1225-0767(ISSN Print)
2287-6715(ISSN Online)
한국연구재단 우수등재학술지

Journal of Ocean Engineering and Technology

Vol. 36, No. 5 (Serial Number 168) October 2022

한국해양공학회지

KSOE

www.joet.org

KSOE The Korean Society of Ocean Engineers

Journal of Ocean Engineering and Technology
한국해양공학회지
Vol. 36 No. 5
(Serial Number 168)
October 31, 2022
www.JOET.org

Editorial Board

Research and Publication Ethics Committee

Published on October 31, 2022
Published by The Korean Society of Ocean Engineers (KSOE)
Room 1302, 13, Jungang-daero 180beon-gil, Dong-gu, Busan, 48821, Korea
TEL: +82-51-759-0656 FAX: +82-51-759-0657 E-mail: ksoehj@ksoe.or.kr URL: http://www.ksoe.or.kr
Printed by Hanrimwon Co., Ltd., Seoul, Korea E-mail: hanrim@hanrimwon.co.kr
ISSN(print) 1225-0767 **ISSN(online)** 2287-6715

This journal was supported by the Korean Federation of Science and Technology Societies (KOFST) grant funded by the Korean government.

Journal of Ocean Engineering and Technology
한국해양공학회지

CONTENTS

Volume 36, Number 5 October, 2022

<Original Research Articles>

GENERAL INFORMATION

"Journal of Ocean Engineering and Technology" is the official journal published by "The Korean Society of Ocean Engineers (KSOE)". The ISO abbreviation is "J. Ocean Eng. Technol." and acronym is "**JOET**". It was launched in 1987. It is published bimonthly in February, April, June, August, October, and December each year. Supplement numbers are published at times.

Journal of Ocean Engineering and Technology (JOET) is a medium for the publication of original research and development work in the field of ocean engineering. JOET covers the entire range of issues and technologies related to the following topics:

Ships and offshore platforms: Design of marine structures; Resistance and propulsion; Seekeeping and maneuvering; Experimental and computational fluid dynamics; Ocean wave mechanics; Fatigue strength; Plasticity; Optimization and reliability; Arctic technology and extreme mechanics; Noise, vibration, and acoustics; Concrete engineering; Thermodynamics and heat transfer; Hydraulics and pneumatics;
Coastal civil engineering: Coastal structures; Port and harbor structures; Soil mechanics; Drilling and exploration; Hydraulics of estuary; Seismic engineering; Coastal disaster prevention engineering;
Ocean renewable energy platforms: Offshore wind turbines; Wave energy platforms; Tidal current energy platforms; Floating photovoltaic energy platforms;
Marine robots: Robot sensor system; Autonomous navigation; Robot equipments; Spatial information and communications; Underwater network; Design of underwater vehicles;
Multidisciplinary areas: Design for safety; IT-based design; IT-based production engineering; Welding mechanics; Control engineering; GPS and GIS; Inspection and sensor; Port and logistics; Leisure boat and deep see water; Offshore process systems engineering; Marine metallic materials; Marine organic materials; Marine Composite materials; Materials properties; Corrosion and Anti-corrosion; Tribology;

It contains original research articles, case reports, brief communications and reviews on technial issues. Conference papers, research papers, diploma papers and academic articles can be submitted.

All of the manuscripts are peer-reviewed. **JOET** has a system where two or more peer reviewers must review each submitted paper and it is operated very strictly.

JOET is being indexed in some prominent database such as Korean Citatation Index (KCI), Google Scholar, Science Central, Korea Science and Directory of Open Access Journals (DOAJ).

For correspondences concerning business matters, author needs to contact KSOE Secretariat by email or phone (e-mail: ksoehj@ksoe.or.kr or Tel: +82 51 759 0656). Correspondences for publication matters can be asked via email to the Editor-in-Chief (email: heroeswise2@gmail.com).

KSOE

Journal of Ocean Engineering and Technology 36(5), 295-302, October, 2022
https://doi.org/10.26748/KSOE.2022.026

pISSN 1225-0767
eISSN 2287-6715

Original Research Article

Ship Motion-Based Prediction of Damage Locations Using Bidirectional Long Short-Term Memory

Hye-young Son[1], Gi-yong Kim[1], Hee-jin Kang[2], Jin Choi[3], Dong-kon Lee[4] and Sung-chul Shin[5]

[1]*Graduate Student, Department of Naval Architecture and Ocean Engineering, Pusan National University, Busan, Korea*
[2]*Senior Director, Alternative Fuels and Power System Research Division, Korea Research Institute of Ships and Ocean Engineering, Daejeon, Korea*
[3]*Principal research engineer, Autonomous & Intelligent Maritime Systems Research Division, Korea Research Institute of Ships and Ocean Engineering, Daejeon, Korea*
[4]*Senior Researcher, Advanced Ship Research Division, Korea Research Institute of Ships and Ocean Engineering, Daejeon, Korea*
[5]*Professor, Department of Naval Architecture and Ocean Engineering, Pusan National University, Busan, Korea*

KEY WORDS: Damage control system, Damage location prediction, BiLSTM, Time-series classification, Recurrent neural network

ABSTRACT: *The initial response to a marine accident can play a key role to minimize the accident. Therefore, various decision support systems have been developed using sensors, simulations, and active response equipment. In this study, we developed an algorithm to predict damage locations using ship motion data with bidirectional long short-term memory (BiLSTM), a type of recurrent neural network. To reflect the low frequency ship motion characteristics, 200 time-series data collected for 100 s were considered as input values. Heave, roll, and pitch were used as features for the prediction model. The F1-score of the BiLSTM model was 0.92; this was an improvement over the F1-score of 0.90 of a prior model. Furthermore, 53 of 75 locations of damage had an F1-score above 0.90. The model predicted the damage location with high accuracy, allowing for a quick initial response even if the ship did not have flood sensors. The model can be used as input data with high accuracy for a real-time progressive flooding simulator on board.*

1. Introduction

Marine accidents can develop into disasters causing large casualties and enormous environmental and property damage owing to their nature. An early response to a marine accident can play a key role in preventing the spread of the accident. Therefore, a damage control system and decision support system must be introduced to accurately detect an accident at its early stage and help the crew to recognize and respond to it (KRISO, 2017). As a study on the flood accident response system, a decision support system for active responses, such as ballasting of damaged ships, was developed (Lee, 2006; Calabrese et al., 2012; Hu et al., 2013; Hu et al., 2015). In these studies, damage information such as the extent and location of damage must be given by crew members or sensor data. In general, direct search for the location of damage by crew members in a ship with a complex structure may cause another safety problem.

Meanwhile, a mathematical model and virtual environment-based decision support system for real-time progressive flooding simulation of damaged ships were developed (Ruponen et al., 2012; Varela et al., 2014; Varela et al., 2015; Varela and Soares, 2007). This flood simulation system is reliable if the initial conditions for hull failure are accurately designed. Furthermore, a sensor-based study was conducted to estimate initial conditions for flooded compartments and to calculate progressive flooding (Ruponen et al., 2017; Bertheussen Karolius et al., 2018; Karolius et al., 2021). If the vessel is equipped with sufficient sensors, the flooding situation can be monitored in real time. However, flooding may not be detected depending on the position of the ship or the accident situation with the flood sensor installed only under safety regulations, and installing flood sensors that can monitor the entire ship in various situations is not cost-effective.

In this study, an algorithm for predicting the location of damage was developed by learning the heave, roll, and pitch motion data with restoring force among motion data obtained from the damaged ship

Received 8 August 2022, revised 2 September 2022, accepted 8 September 2022
Corresponding author Sung-chul Shin: +82-51-510-2525, scshin@pusan.ac.kr

simulation using an RNN(Recurrent Neural Network) model. It can be used for decision-making in case of progressive flooding simulation or accident response by predicting the location of damage with high accuracy without using flood sensors or direct searching by a crew member. In the prior study (Son et al., 2021), an algorithm for predicting the location of damage was developed using the short time Fourier transform (STFT) to obtain the case most similar to the real-time ship motion data among the damaged ship simulation data in various scenarios. Time-series data was transformed to a spectrogram matrix using STFT, and the real-time motion data converted under the same conditions were compared with all simulated scenarios to predict the damage location. The F1-score, used as an index to evaluate the accuracy of the model, is the harmonic average of Precision and Recall and is an index that expresses the accuracy of the model better than Accuracy when the data is unbalanced by class. In prior studies, the F1-score was observed to be as high as 0.90. However, comparing real-time ship motion data and simulation-based damaged ship motion data requires considerable computation, and further improvements are needed. As a follow-up study, the time series data was learned using an RNN model, and by comparing the results with those of the prior studies, the applicability of the damaged location prediction model using damaged ship motion data was reviewed.

2. Research Methodology

2.1 Recurrent Neural Network

As shown in Fig. 1, a recurrent neural network (RNN) predicts by considering the data input at the previous time and at the current time. RNNs with these characteristics are widely used in natural language processing, machine translation, text analysis, emotion recognition, sentence generation, sensor data analysis, and image analysis (Kim, 2020). However, a simple RNN is not applicable when learning data showing trends over a long period of time through a backpropagation algorithm. A problem exists in that inferring a relationship is difficult when the position between the existing input data and the data to be referenced increases. This causes gradient exploding and gradient vanishing. Long short-term memory (LSTM) was developed to solve this problem (Noh and Cho, 2021).

Unlike conventional RNNs, LSTM introduces cell state to enable long-term memory. At time t, the LSTM structure consists of a forget gate, an input gate, and output gate. In Fig. 2, F, I, and O boxes represent the forget, input, and output gates, respectively.

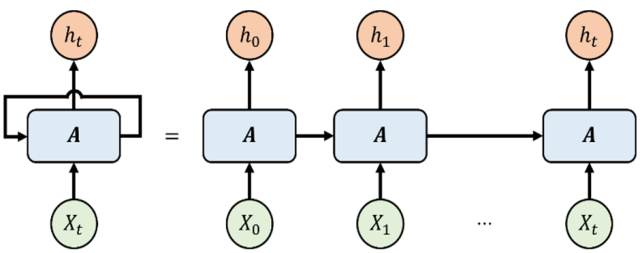

Fig. 1 Recurrent Neural Network architecture

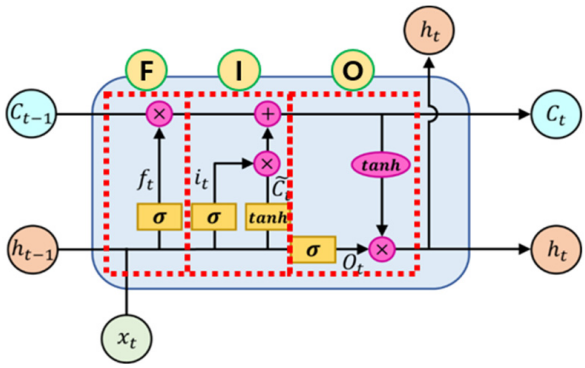

Fig. 2 Long Short-Term Memory architecture

As shown in Eq. (1), A forget gate is a part used to erase unnecessary information from the cell state by deciding what information from the past should be retained. In this case, h_{t-1} represents the hidden state at $t-1$, x_t represents the input data at t, and W_f and b_f represent the weight and bias of the forget gate, respectively. Using sigmoid function σ, unnecessary information is assigned a weight close to 0 to forget the information, and important information is assigned a weight close to 1 to learn to completely preserve the information. The calculated f_t is transferred to the cell state for the next operation.

$$f_t = \sigma(W_f \cdot [h_{t-1}, x_t] + b_f) \tag{1}$$

The input gate is a gate for storing current information as shown in Eqs. (2)–(4). Using current input value x_t and previous hidden state h_{t-1}, i_t indicating the degree to remember the current input value and the current local state $\overline{C_t}$ are obtained. Global cell state C_t to be transmitted to the next hidden state is determined by reflecting the received previous cell state C_{t-1}. In this case, W_i and b_i denote the weight and bias of the input gate, respectively, and W_C and b_C denote the weight and bias of the cell state, respectively.

$$i_t = \sigma(W_i \cdot [h_{t-1}, x_t] + b_i) \tag{2}$$

$$\overline{C_t} = \tanh(W_C \cdot [h_{t-1}, x_t] + b_C) \tag{3}$$

$$C_t = f_t \times C_{t-1} + i_t \times \overline{C_t} \tag{4}$$

As shown in Eqs. (5) and (6), the output gate calculates current hidden state h_t that will be delivered to the hidden layer reflecting current global cell state C_t obtained with o_t, which expresses the extent of memory of the current output value calculated using previous hidden layer h_{t-1}, and current input value x_t. In this case, W_O and b_O denote the weight and bias of the output gate, respectively.

$$o_t = \sigma(W_o \cdot [h_{t-1}, x_t] + b_o) \tag{5}$$

$$h_t = o_t \times \tanh(C_t) \tag{6}$$

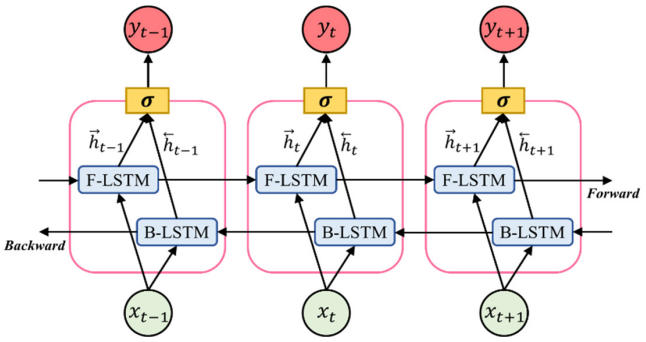

Fig. 3 BiLSTM architecture

Bidirectional LSTM (BiLSTM) is a combination of forward LSTM (F-LSTM) and backward LSTM (B-LSTM) as shown in Fig. 3. When time series data of a certain length is given as an input, F-LSTM learns time series data in the same order as the input, and B-LSTM learns in the reverse order of the input. Each F-LSTM and B-LSTM learn independently to derive each hidden layer. When LSTM is applied to time series data, a certain length of the data for each feature is used as one input. Input values are generated at regular intervals by overlapping. In this case, the length of the input time series data is called the window length. These BiLSTM models are being widely used in time series classification and prediction fields such as natural language processing and handwriting recognition, and in most studies, they performed better than ordinary LSTMs.

2.2 Multiple Classification Model Performance Indicators

A confusion matrix is a representative method used to evaluate the performance of a classification model. As shown in Fig. 4, the matching types of the actual class and the predicted class by the classification model can be divided into four types. True positive (TP) indicates positive being classified as positive, true negative (TN) indicates negative being classified as negative, false negative (FN) indicates positive being classified as negative, and false positive (FP) indicates negative being classified as positive.

Accuracy, Recall, Precision, and F1-score are major indicators of model performance as a confusion matrix and are defined by Eqs. (7)–(10).

$$Accuracy = \frac{TP + TN}{TP + TN + FP + FN} \tag{7}$$

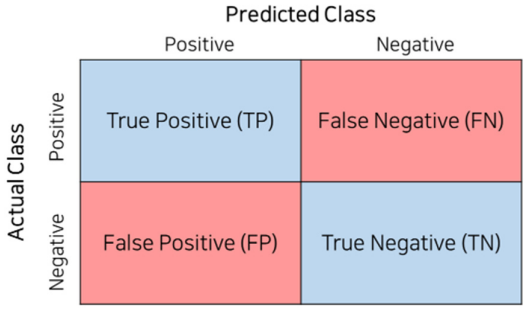

Fig. 4 Confusion matrix

$$Precision = \frac{TP}{TP + FP} \tag{8}$$

$$Recall = \frac{TP}{TP + FN} \tag{9}$$

$$F1 - score = 2 \times \frac{Precision \times Recall}{Precision + Recall} \tag{10}$$

Accuracy is the ratio of the number of correct answers, that is, the number of TP and TN predictions, to the total number of predictions. Although it most intuitively indicates the performance of the model, if the number of negative and positive data is unbalanced, the reliability of the indicator decreases. Therefore, Recall, Precision, and F1-score are introduced. Recall is the ratio of the true positive value of the actual positive value. Precision is the ratio of the true positive of the positive predicted value. F1-score is the harmonic mean of Recall and Precision. F1-score can evaluate the performance of a classification model even when the data are imbalanced (Park et al., 2020). In this study, classification performance was evaluated using the F1-score obtained by assigning different weights according to the amount of data in each class.

3. Data and Learning

3.1 Damaged Ship Motion Data

A 5,200-ton class vessel of the Korea Institute of Maritime and Fisheries Technology with the main specifications of 145 m in length, 18 m in width, and 7.5 m in depth was used as a simulated model in this study.

The motion data of 5400 scenarios were obtained by simulating the behavior of the damaged ship for 1 h with a combination of 75 damaged locations, three damage sizes, three sea states, and eight regular wave incident angles. The Korea Research Institute of Ships & Ocean Engineering in-house code 'SMTP' (Lee, 2015) was used for the simulation. As shown in Fig. 5, the damage location was divided into 75 with 15 locations in the longitudinal direction, one at the bottom of the ship, and four at the side of the ship in the height direction.

The damage size was divided into 30%, 70%, and 100% of the maximum damage size derived from statistical data (IMO, 2003). In this study, the maximum damage area at the hull side, Max_{HS}, owing to collision is expressed as Eq. (11), and the maximum damage area at the hull bottom, Max_{HB}, owing to stranding is expressed as Eq. (12).

$$Max_{HS} = 0.1L \times 0.1B \times 0.3D \tag{11}$$

$$Max_{HB} = 0.3L \times 0.3B \times 0.1D \tag{12}$$

Here, L indicates the overall length, D indicates the depth, and B indicates the moulded breadth.

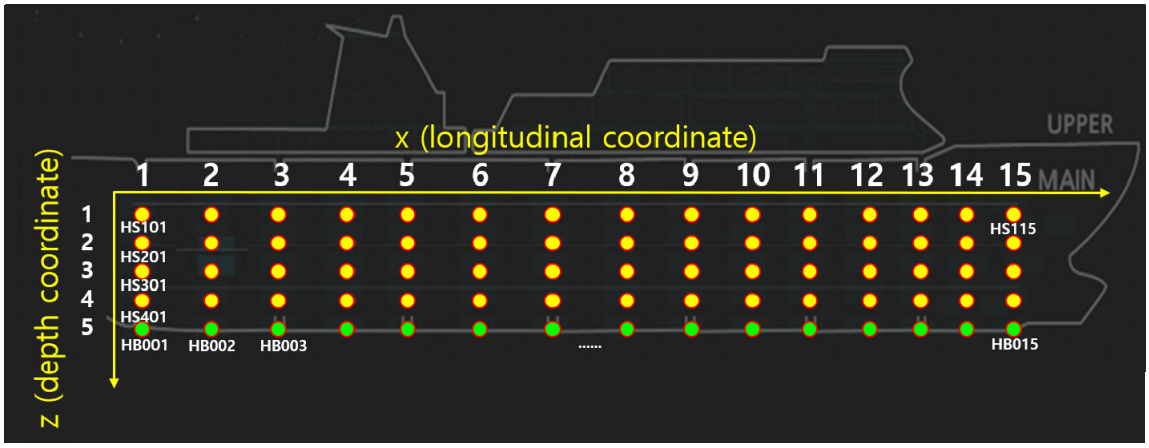

Fig. 5 Locations of damage centers using three-digit codes and a coordinate system

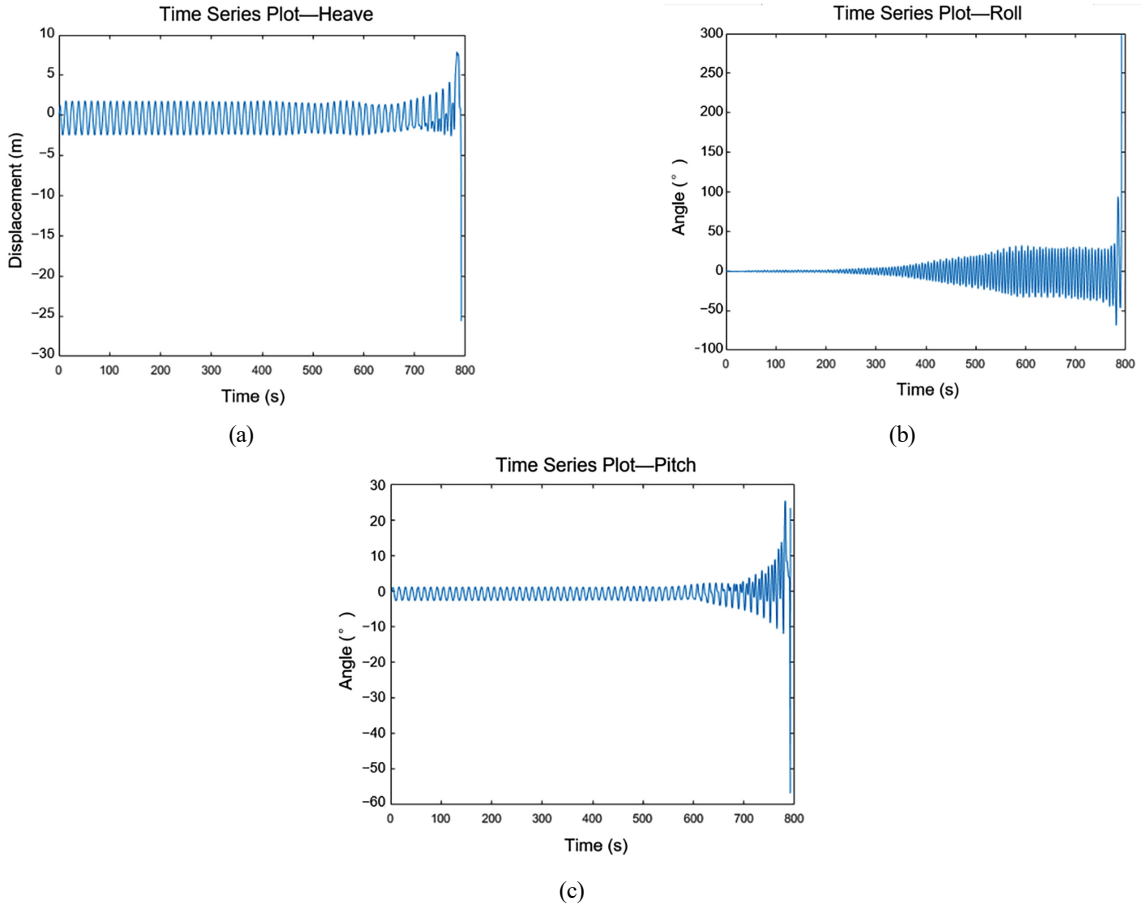

Fig. 6 Time-series motion of the case HB001HA100_SS06WA135: (a) Heave; (b) Roll; (c) Pitch

Table 1 Significant wave height and spectral peak period

Sea state	Average significant wave height	Most probable spectral peak period
4	1.88 m	8.80 s
5	3.25 m	9.70 s
6	5.00 m	12.40 s

For the sea state, the average wave height and period corresponding to sea states 4, 5, and 6, as presented in Table 1, were applied. The incident angle of the regular wave was simulated by dividing 0° to 315° in eight directions at intervals of 45°.

The downflooding angle is the minimum heeling angle at which an opening that is not watertight and not submerged. Owing to the nature of the simulation, a capsizing criterion for the motion data of the damaged ship is required. Therefore, when the rolling angle was equal to or greater than the downflooding angle, the ship was decided as capsized, and only time series data up to that point were used (DNV GL, 2017).

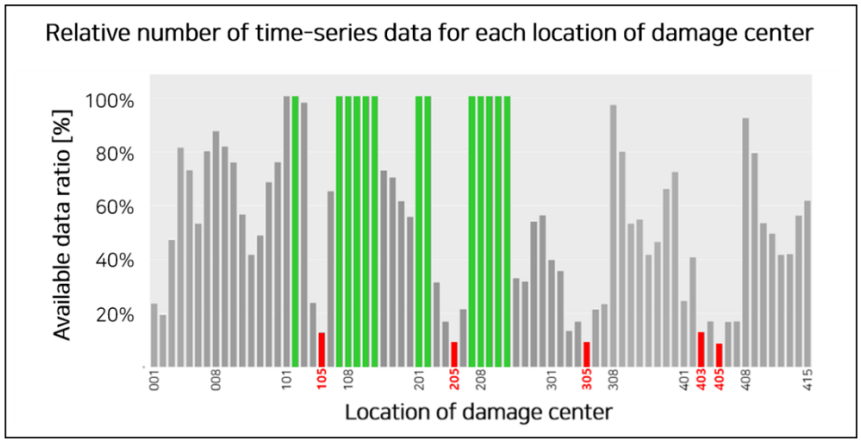

Fig. 7 Relative data ratio for each location of damage center

As an example, the case HB001HA100_SS06WA135, which means that the damage location HB001, closest to the stern among damage locations on the hull bottom, the damage size of 100% of the stochastic maximum damage area, sea state 6, the ship motion time series data of heave, roll, and pitch when the regular wave incident angle is 135°, is shown in Fig. 6.

As shown in the example, several cases existed where the capsizing occurred earlier than an hour at a specific damaged location. In this case, the amount of data was small compared with the amount of data corresponding to the damage location where the capsizing did not occur within 1 h even under various conditions. Fig. 7 shows the relative ratio of the number of the data according to each damage location class. As shown in Fig. 7, the number of the data varied depending on the location of the damage. For example, the number of scenarios for each damage location is 72 with a combination of three maximum damage sizes, three sea states, and eight regular wave incident angles. As shown in Fig. 7, in all scenarios where the damage occurred at location 201, the rolling angle of the simulation data did not exceed the downflooding angle of 45°; therefore, all data could be used. However, in the case of damage at location 405, the amount of data available for learning was insufficient than the data at location 201.

3.2 BiLSTM Classification Model

In this study, a prediction model of the damage location was developed by learning the damaged ship motion time series data using BiLSTM. Among the simulation motion data for 5400 damage scenarios, heave, roll, and pitch were learned to learn the relationship between the damaged ship motion and the damage location.

The simulation data used in this study was recorded in every 0.5 s. Because this is a complex wave with a small frequency owing to the nature of the ship motion, the data obtained in units of 0.5 s for 200 window lengths, that is, 100 s, were used as input. In addition, to learn the change in time series data with the passage of time, the overlap length was set to 160 and prediction was performed every 20 s. Fig. 8 shows the window length and overlap length as a concept for using time series data as input values.

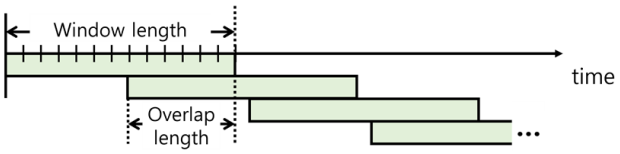

Fig. 8 Window length and overlap length

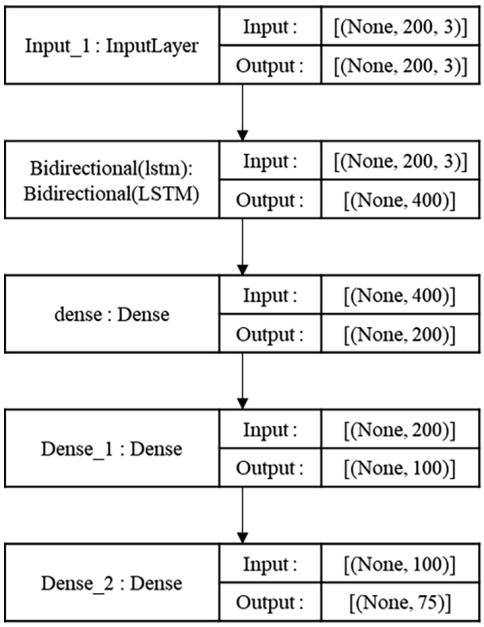

Fig. 9 Structure of the classifier for this study

To learn the characteristics of time series data, it should be divided into an appropriate length and used as an input. Because ship motion has a small frequency, it is not easy to learn its characteristics if only short data is used as an input. Therefore, in this study, 200 units of time series data from heave, roll, and pitch were used as an input. In Fig. 9, the unit of InputLayer is [(None, 200, 3)], which implies that heave, roll, and pitch are used as three input features, and 200 time series data are used for each feature. “None” is a factor related to the length of the data to be input and indicates the number of the data that has not yet been determined. The deep neural network consists of a BiLSTM layer and dense layers (fully-connected layer) that reduce the dimension of

the layer. The structure of the classification model is shown in Fig. 9. Robust scaler was used for data standardization. Training and testing data of the model was divided at a rate 8:2. For the activation and loss functions, "SoftMax" and "categorical cross entropy," which are used for multi-classification problems, were used, and the batch size was 64 and epoch 100 was trained. Because of the data imbalance for each class, test data were collected in proportion to the amount of data in each class.

4. Results of the Research

Damage location prediction is a multi-classification problem and data is imbalanced according to each damage location class. Therefore, the final model was selected using the F1-score, a weighted harmonic mean of Precision and Recall, as an index rather than Accuracy. Table 2 presents a comparison of the performance of the previous research model and the model using BiLSTM for 200 time steps.

The F1-scores of 53 of 75 classes were 0.90 or higher. As shown in the error matrix in Fig. 10, most of the classification model is distributed in the diagonal line; this is the case where the correct answer class is matched.

At specific damage locations, flooding tended to proceed rapidly. This implied that a sufficient amount of data could not be collected for all damage locations. Fig. 11 shows data ratios and F1-scores for each

Table 2 Classification performance of models

Model	Precision	Recall	Accuracy	F1-score
Previous model (Son et al., 2021)	0.90	0.90	0.90	0.90
BiLSTM model	0.94	0.92	0.93	0.92

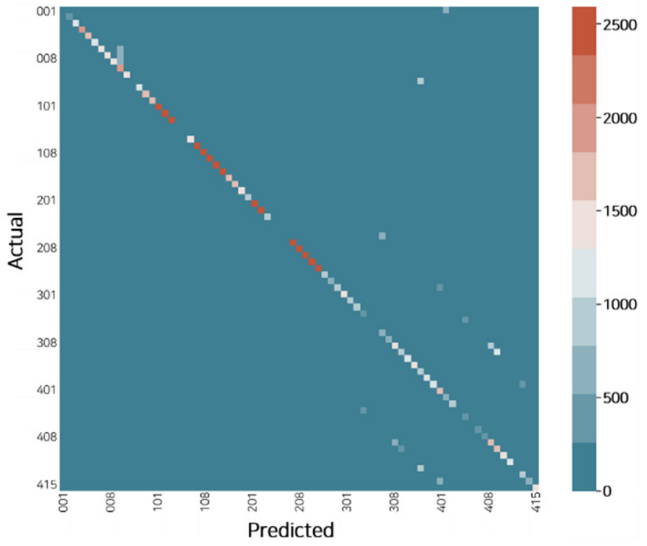

Fig. 10 Confusion matrix of the BiLSTM classifier

of the 75 damage locations. Because the test data was extracted proportionally by each class data, the test data ratio was the same for the entire test. As shown in Fig. 11, the F1-score was low owing to the insufficient amount of the data at some specific damaged locations because of rapidly proceeded capsizing. The number of data and the F1-score of the model are partly proportional.

5. Conclusion

In this study, an algorithm for prediction of the damage location was developed by learning the damaged ship motion time series data with BiLSTM. Through the simulation, the motion data of the damaged ship for 1 h were collected at 0.5-s intervals. A total of 200 units, that

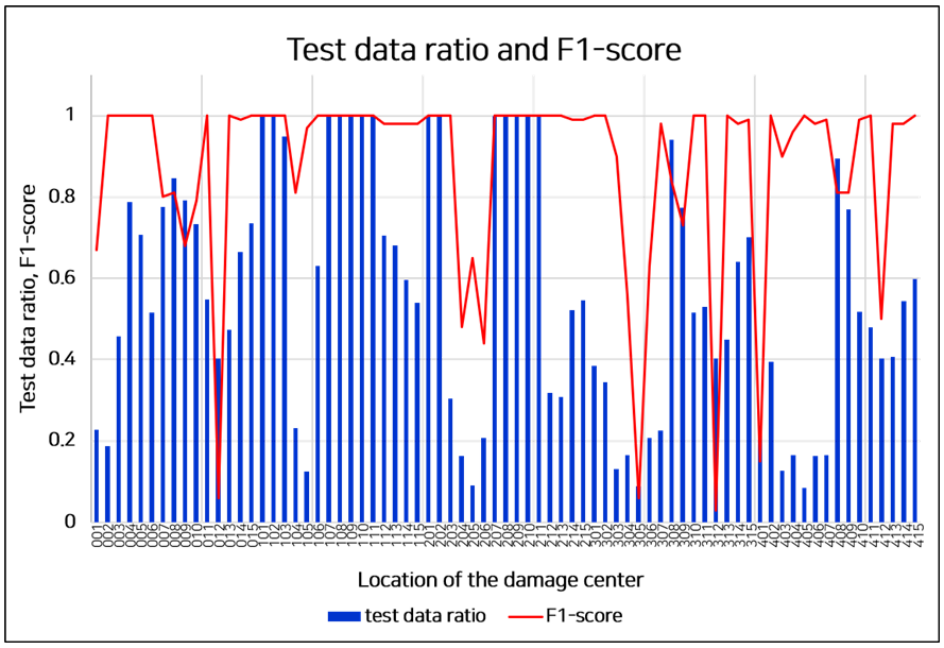

Fig. 11 Number of test samples for classification and corresponding F1-scores

is, data collected for 100 s was used as an input, and a model was developed to predict the damage location every 20 s by overlapping the 80% of the previous input.

Consequently, the model showed a high accuracy with an F1-score of 0.92, and 53 of 75 classes showed an F1-score of 0.90 or higher. The damage location prediction model in the damaged ship using this BiLSTM showed better classification performance than the previous model that classified the damage location by converting the ship's heave, roll, and pitch motions into spectrograms. In addition, computing time and cost efficiency were improved.

The developed model can be used as a part of the flood damage control system. This model enables rapid initial response by predicting the location of damage with high accuracy before proceeding with a direct damage location search by a crew member when the location of damage cannot be accurately determined by flood detection sensors, and it can be applied in case the flooding sensor is missed or malfunctions. Furthermore, the predicted damage location can be used as input with high accuracy to the progressive flooding simulator, with on-board real-time calculations.

In future research, we plan to develop a model that can improve the accuracy of the prediction of the damage location even when an imbalance in data exists. In addition, we plan to continue developing a decision support system to respond to ship accidents.

Conflict of Interest

No potential conflict of interest relevant to this article was reported.

Funding

This research was supported by the 'Development of Autonomous Ship Technology (20200615)' funded by the Ministry of Oceans and Fisheries (MOF, Korea).

References

Bertheussen Karolius, K., Cichowicz, J., & Vassalos, D. (2018). Risk-based positioning of flooding sensors to reduce prediction uncertainty of damage survivability. *Proceedings of the 13th International Conference on the Stability of Ships and Ocean Vehicles, Kobe, Japan.*

Calabrese, F., Corallo, A., Margherita, A., & Zizzari, A. A. (2012). A knowledge-based decision support system for shipboard damage control. *Expert Systems with Applications, 39*(9), 8204–8211. https://doi.org/10.1016/j.eswa.2012.01.146

DNV GL. (2017). *Rules for classification ships - Part 3 Hull –Chapter 15 Stability*. Det Norske Veritas.

Hu, L. F., Ma, K., & Ji, Z. S. (2013). AM–H method-based decision support system for flooding emergencies onboard warship. *Ocean Engineering, 58*, 192–200. https://doi.org/10.1016/j.oceaneng.2012.10.012

Hu, L. F., Tian, Z., Sun, Z., Zhang, Q., & Feng, B. (2015). Genetic algorithm-based counter-flooding decision model for damaged warship. *International Shipbuilding Progress, 62*(1–2), 1–15. https://doi.org/10.3233/ISP-140114

IMO. (2003). Revised Interim guidelines for the approval of alternative methods of design and construction of oil tankers under Regulation 13F (5) of Annex 1 of MARPOL 73/78. *Resolution MEPC, 110*(49).

Karolius, K. B., Cichowicz, J., & Vassalos, D. (2021). Risk-based, sensor-fused detection of flooding casualties for emergency response. *Ships and Offshore Structures, 16*(5), 449–478. https://doi.org/10.1080/17445302.2020.1735846

Kim, C. (2020). *Design and performance analysis of 1D-CRNN based fault detection system for naval vessel* [Master's thesis, Kumoh National Institute of Technology].

Korea Research Institute of Ships & Ocean Engineering (KRISO). (2017). *Development of marine casualty initial response and salvage technical support system.* KRISO.

Lee, D. (2006). Knowledge-based system for safety control of damaged ship. *Knowledge-based systems, 19*(3), 187–191. https://doi.org/10.1016/j.knosys.2005.11.005

Lee, G. J. (2015). Dynamic orifice flow model and compartment models for flooding simulation of a damaged ship. *Ocean Engineering, 109*, 635–653. https://doi.org/10.1016/j.oceaneng.2015.09.051

Noh, Y. D., & Cho, K. C. (2021). A Text Content Classification Using LSTM For Objective Category Classification. *Journal of the Korea Society of Computer and Information, 26*(5), 39–46. https://doi.org/10.9708/jksci.2021.26.05.039

Park, M. K., Choi, J. W., & Whangbo, T. K. (2020). A symptom recognition method of diseases for senior user based on language odel. *Proceedings of the Korea Information Processing Society Conference*, 461–463. https://doi.org/10.3745/PKIPS.y2020m05a.461

Ruponen, P., Larmela, M., & Pennanen, P. (2012, September). Flooding prediction onboard a damaged ship. *Proceedings of the 11th International Conference on the Stability of Ships and Ocean Vehicles, Athens, Greece,* 23–28.

Ruponen, P., Pulkkinen, A., & Laaksonen, J. (2017). A method for breach assessment onboard a damaged passenger ship. *Applied Ocean Research, 64*, 236–248. https://doi.org/10.1016/j.apor.2017.01.017

Son, H. Y., Roh, H. D., Kim, G. Y., Oh, S. J., Choi, J., Lee, D. K., & Shin, S. C. (2021). Prediction of flooded compartment damage locations in ships by using spectrum analysis of ship motions in waves. *Journal of Marine Science and Engineering, 10*(1), 17. https://doi.org/10.3390/jmse10010017

Varela, J. M., & Soares, C. G. (2007). A virtual environment for decision support in ship damage control. *IEEE Computer Graphics and Applications, 27*(4), 58–69. https://doi.org 10.1109/MCG.2007.74.

Varela, J. M., Rodrigues, J. M., & Soares, C. G. (2014). On-board decision support system for ship flooding emergency response. *Procedia Computer Science, 29*, 1688–1700. https://doi.org/10.1016/j.procs.2014.05.154

Varela, J. M., Rodrigues, J. M., & Soares, C. G. (2015). 3D simulation of ship motions to support the planning of rescue operations on damaged ships. *Procedia Computer Science, 51*, 2397–2405. https://doi.org/10.1016/j.procs.2015.05.416

Author ORCIDs

Author name	ORCID
Son, Hye-young	0000-0001-7794-1851
Kim, Gi-yong	0000-0003-0980-8375
Kang, Hee-jin	0000-0002-8241-3751
Choi, Jin	0000-0001-9842-2049
Lee, Dong-kon	0000-0001-5066-5850
Shin, Sung-chul	0000-0003-1814-9578

KSOE

Journal of Ocean Engineering and Technology 36(5), 303-312, October, 2022
https://doi.org/10.26748/KSOE.2022.025

pISSN 1225-0767
eISSN 2287-6715

Original Research Article

Computational Investigation of Seakeeping Performance of a Surfaced Submarine in Regular Waves

Doojin Jung[1,2] and Sanghyun Kim[3]

[1]*Graduate Student, Department of Naval Architecture & Ocean Engineering, Inha University, Incheon, Korea*
[2]*Principal Research Engineer, Department of Fluid Dynamics R&D, Daewoo Shipbuilding and Marine Engineering Co., Ltd, Siheung, Korea*
[3]*Professor, Department of Naval Architecture & Ocean Engineering, Inha University, Incheon, Korea*

KEY WORDS: Submarine, Seakeeping, CFD, Potential theory, Regular waves, Free surface conditions

ABSTRACT: *A submarine is optimized to operate below the water surface because it spends most of its time in a submerged condition. However, the performance in free surface conditions is also important because it is unavoidable for port departure and arrival. Generally, potential flow theory is used for seakeeping analysis of a surface ship and is known for excellent numerical accuracy. In the case of a submarine, the accuracy of potential theory is high underwater but is low in free surface conditions because of the nonlinearity near the free surface area. In this study, the seakeeping performance of a Canadian Victoria Class submarine in regular waves was investigated to improve the numerical accuracy in free surface conditions by using computational fluid dynamics (CFD). The results were compared to those of model tests. In addition, the potential theory software Hydrostar developed by Bureau Veritas was also used for seakeeping performance to compare with CFD results. From the calculation results, it was found that the seakeeping analysis by using CFD gives good results compared with those of potential theory. In conclusion, seakeeping analysis based on CFD can be a good solution for estimating the seakeeping performance of submarines in free surface conditions.*

Nomenclature

BM	Metacentric radius
GM	Metacentric height
H_s	Significant wave height
K_{xx}	Roll radius of gyration
LCG	Longitudinal center of gravity
T_p	Wave peak period
USK	Under Side of Keel
VCG	Vertical center of gravity
λ	Wave length
μ	Wave direction

1. Introduction

Over the last 100 years, since the development of the diesel-powered submarine by the French Navy in 1863, submarine design has changed remarkably. The hull form of early submarines was similar to those of surface ships, but a rounded hull form was used to reduce water resistance and increase speed for tactical planning (Krishna and Krishnankutty, 2016). Submarines spend most of their time below the water surface, so the design was optimized for submerged conditions. However, the performance in free surface conditions is also important because submarines face various scenarios. Military submarines avoid going out on the water to minimize exposure to enemies, but free surface conditions are unavoidable for port departure and arrival, and it is necessary to study the seakeeping performance in extreme environments (Burcher and Rydill, 1995). In addition, submarines have very poor rolling in free surface conditions because they have a rounded shape with very few appendages. For these reasons, research on the seakeeping performance of submarines in free surface conditions is steadily continuing, but only a few papers have been published for security reasons.

Received 1 August 2022, revised 16 August 2022, accepted 16 August 2022
Corresponding author Sanghyun Kim: +82-32-860-7344, kimsh@inha.ac.kr
It is noted that this paper is presented on the subject of "Study of submarine seakeeping performance at free surface condition in regular waves" in the 15th International Symposium on Practical Design of Ships and Other Floating Structures PRADS 2022 (Jung and Kim, 2022).

Hedberg (2006) created a method to simulate the roll motion of a submarine in a linear way in the frequency domain and in a nonlinear way in the time domain for a surfaced submarine. The two methods are used to study how difference sea states, adding appendages, and varying the transverse metacenter height affects the roll angle of submarine while surfaced. Thornhill and Hermanski (2008) performed a computational fluid dynamics (CFD) simulation and physical experiments based on a 2D surfaced submarine section for estimating the effects on roll motion of a closed versus free-flooding casing and found that the opening size had a significant impact on roll damping. Vogels (2016) investigated the roll damping of surfaced submarines based on the mathematical model and experiments using several combinations of rudder configuration, forward speed, roll amplitude, and roll frequency. Cansiz and Yildiz (2021) created a mathematical model of roll decay motion for a submarine in surface conditions, and the roll damping term was obtained numerically by carrying out roll decay simulations using CFD code.

Generally, potential flow theory is used for seakeeping analysis of a surface ship and is known for excellent numerical accuracy. Potential flow theory was invented by Gerritsma and Beukelman (1970) based on the assumption of a slender ship. Bingham (1994) overcame the assumption of a slender ship and used 3D codes based on free surface conditions and a wave source. Kring (1994) applied a Rankine source to consider both the hull and free surface for seakeeping analysis, but there was a limitation in not sufficiently considering the viscous effects. In the case of a submarine, the accuracy of potential flow theory is high underwater but is low in free surface conditions because of the nonlinearity near the free surface area, low damping, etc. Therefore, seakeeping analysis for surface conditions is extremely challenging, and most shipyards seem to rely on a wave basin test.

In general, a submarine has limited access to public documents due to issues such as military secrets and security maintenance, and it is extremely difficult to obtain related material. In this study, a Canadian Victoria Class submarine was chosen as a target vessel, and the experimental results have been published in the 2010 11th International Symposium on Practical Design of Ships and Other Floating Structures (PRADS) (Hermanski and Kim, 2010). The main goal of this study is to improve the numerical accuracy in free surface conditions using CFD. Compared to physical experiments, CFD is financially efficient, and the intensity of physical labor is low. However, there has been a drawback in that it is difficult for computer hardware to perform large-capacity calculation. But recently, with the development of computer hardware technology, the value of CFD has been increasing. In this study, Star-CCM+ was used as a Reynolds-averaged Naver Stokes (RANS) solver to estimate the seakeeping performance of a submarine, and the results were compared to those of model tests from a published paper (Hermanski and Kim, 2010). In addition, the potential theory software Hydrostar developed by Bureau Veritas was also used for seakeeping performance to compare with the CFD results.

2. Target Vessel

In the present study, the Canadian Victoria Class submarine was chosen as a target vessel, which is illustrated in Fig. 1. The experimental results of the Canadian Victoria Class submarine have been published in the 2010 PRADS 11th triennial (Hermanski and Kim, 2010), which is one of the reasons why the Canadian Victoria Class submarine was chosen. A 3D model was created from the body plan in the published paper and was repaired using Star-CCM+. The bare hull for numerical calculation is 1:14.96 scale, and the main dimensions are defined in Table 1.

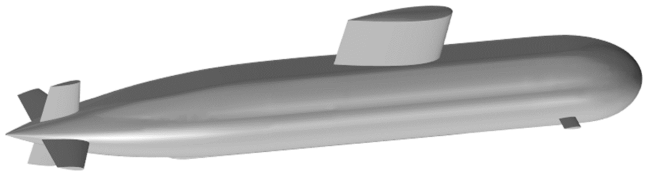

Fig. 1 3D model of the Canadian Victoria Class Submarine

Table 1 Principal dimensions of the Canadian Victoria Class Submarine

Item	Model-scale	Full-scale
Length overall (LOA) (m)	4.696	70.25
Beam (m)	0.508	7.6
Forward Draft (m)	0.462	6.909
After Draft (m)	0.581	8.699
Displacement (t)	0.671 (fresh water)	2281.0 (salt water)
Trim by stern (°)	2.010	2.01
BM above USK (m)	0.012	n/a
VCG above USK (m)	0.264	4.184
GMT (m)	0.038	0.362
LCG from midships (m)	0.088	1.274
K_{xx} (m)	0.212	3.176
Scale ratio	1 :14.96	-

3. Seakeeping Analysis

3.1 Potential Flow Theory

In the present study, CFD code and potential flow theory were used for seakeeping analysis of the submarine, and the results were compared to those of the model tests for verification. The seakeeping analysis based on potential flow theory was performed with Hydrostar for Experts V8.10, which has been developed by Bureau Veritas since 1991. Hydrostar is powerful 3D diffraction/radiation potential software that provides a complete solution to a first-order problem of wave diffraction and radiation and also second-order low-frequency wave loads for a floating body with or without forward speed in deep water and in finite water depth (BV, 2019). For 3D diffraction/radiation potential theory, the hull was modeled as panels according

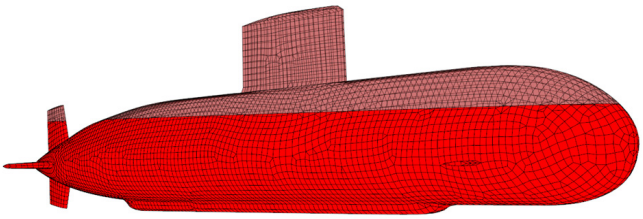

Fig. 2 Panel mesh for potential code

the hull geometry. The number of panels is governed by the panel size, and the maximal panel length should be smaller than 1/6 of the minimum wave length considered for analysis. The panel model used in Hydrostar is shown in Fig. 2.

The seakeeping analysis was performed at all wave headings from head (180º) to following (0º) seas (12 headings with 30º spacing), and a forward speed of 3 knots (1.54 m/s) was used. Wave frequencies of 0.27 rad/s to 1.32 rad/s were used with steps in wave frequencies not exceeding 0.04 rad/s. Since the viscosity effect on the roll response is important to arrive at a realistic roll angle, appropriate roll viscous damping should be included. In this study, 5% viscous roll damping was taken from a roll decay test in a published paper (Hermanski and Kim, 2010).

After the modeling and mesh generation were completed, the response amplitude operators (RAOs) with six degrees of freedom were calculated, and the results of heave, roll, and pitch are shown in Figs. 3–5. From the results, unlike the heave and pitch RAOs of typical

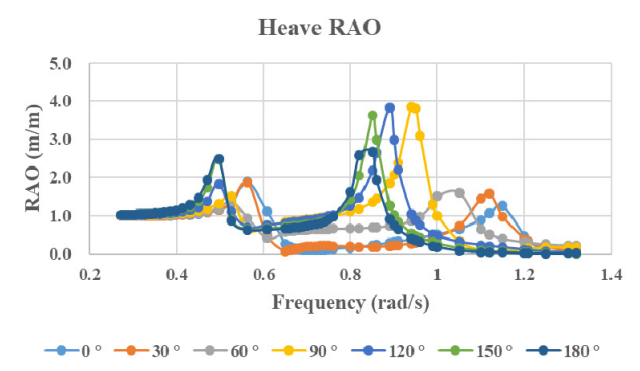

Fig. 3 Heave RAOs from potential code

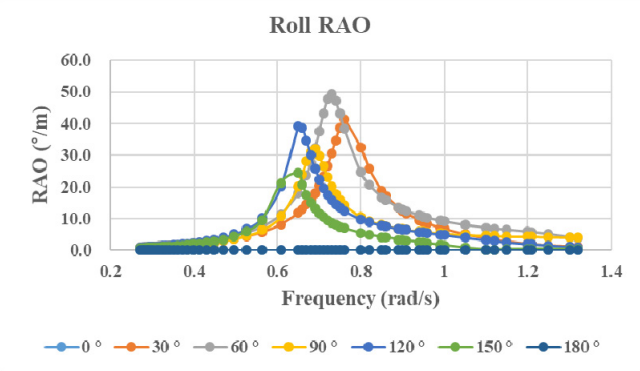

Fig. 4 Roll RAOs from potential code

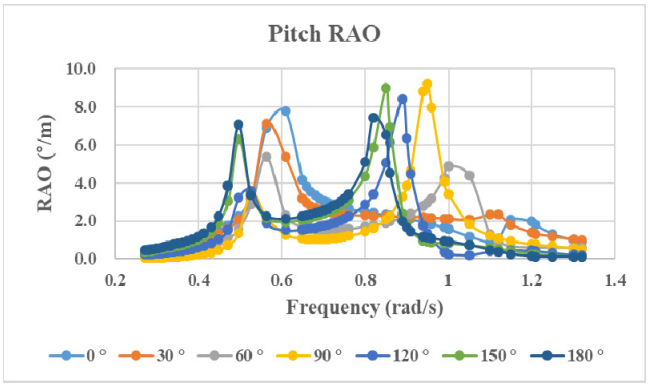

Fig. 5 Pitch RAOs from potential code

surface ship, those of a surfaced submarine take double peaks into account. Roll RAOs of quartering waves (30º, 60º and 120º) are higher than that of beam sea (90º). These results seem to be due to the nonlinearity near the free surface area, as will be shown later.

3.2 Computational Fluid Dynamics

The seakeeping analysis based on the regular wave simulation was performed with the commercial CFD software STAR-CCM+ V15.06. Fig. 6 shows the computational domain that was used in this study. The computational domain consists of two regions (a tank region and overset region) and was generated with size corresponding to 0.7 times the ship length (L) from the forward direction of the ship to 3.3 times L from the backward direction, 3.0 times Lpp in the horizontal direction, and 2.5 times Lpp in the vertical direction. The dynamic fluid body interaction method with overset grid and two sets of spring damper system were used to simulate the 6 degrees of freedom of motion.

For body-environment coupling, a pair of linear springs was attached to the bow and stern, and an elasticity coefficient of 100 N/m was used to minimize the effect on the ship's motions. The boundary conditions for the inlet, outlet, top, bottom and side (port and starboard) were assigned as velocity inlets, and the velocity was

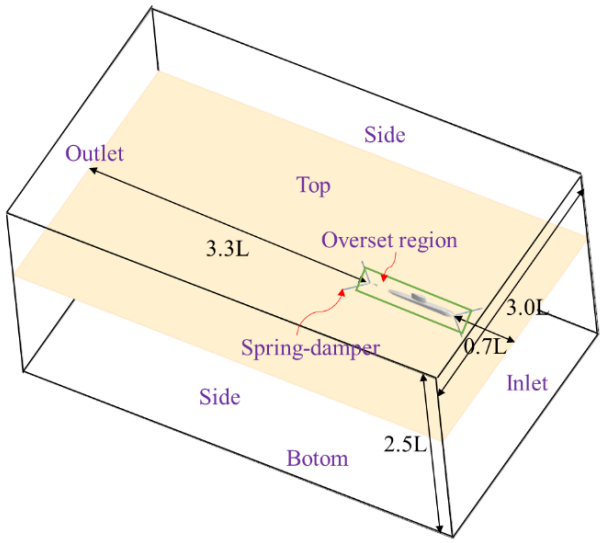

Fig. 6 Computational domain for regular wave simulation

Table 2 Simulation conditions for regular waves

Ship speed	3 knots (1.54 m/s)
Degrees of freedom	6 degrees of freedom
λ/L	0.5, 0.6, 0.7, 0.8, 0.9, 1.0, 1.1, 1.2, 1.3, 1.5, 1.8, 2.0, 2.5, 3.0 and 3.5
H/λ	1/50
Wave heading	180º (head sea), 150º, 120º, 90º, 60º, 30º and 0º (following sea)
Turbulence model	Realizable k-ϵ
Multiphase model	Volume Of Fluid (VOF)
Time scheme	Second order scheme in time
Convection scheme	Second order upwind scheme
Diffusion scheme	Central difference scheme

defined as the same flow as the submarine's target speed. For considering the free surface, the volume of fluid (VOF) method was used, and a VOF wave forcing zone was applied to the inlet (forcing zone size: 0.3L), outlet (forcing zone size: 1.5L), and side (forcing zone size: 0.25L) to eliminate disturbed flows.

The simulation conditions for regular wave cases are described in Table 2. The regular wave simulations were performed with seven wave headings and forward speeds of 3 knots (1.54 m/s). The wavelength (λ) was between 0.5 and 3.5 times the ship length, and the wave steepness (H/λ) was fixed with a value of 1/50. The turbulence was modeled with the realizable k- ε turbulence model for numerical stability and is generally used for the marine industry. In order to reduce the wave dissipation, a second-order scheme in time was applied, and a 5th-order Stokes wave was used in the simulation. The

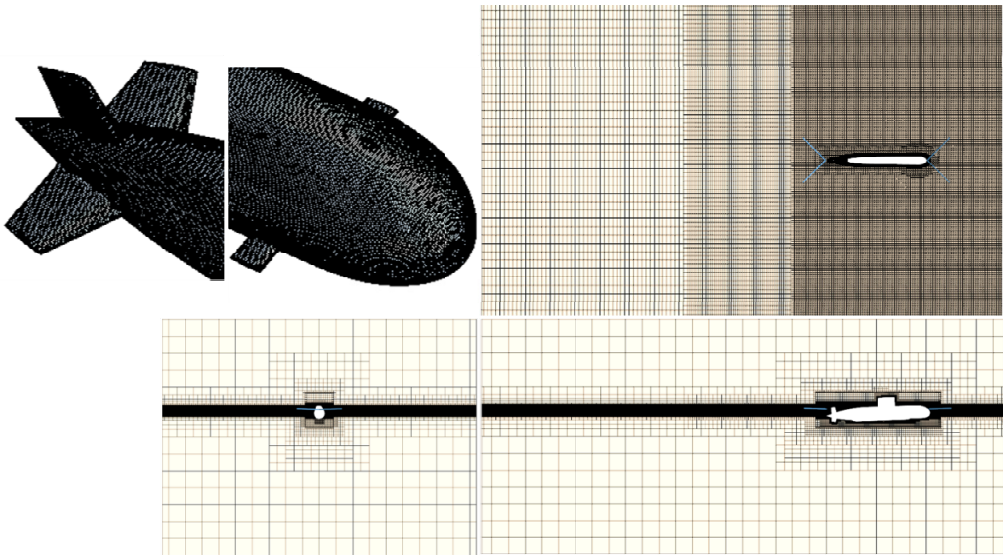

Fig. 7 Mesh distribution for head sea (180º) simulation

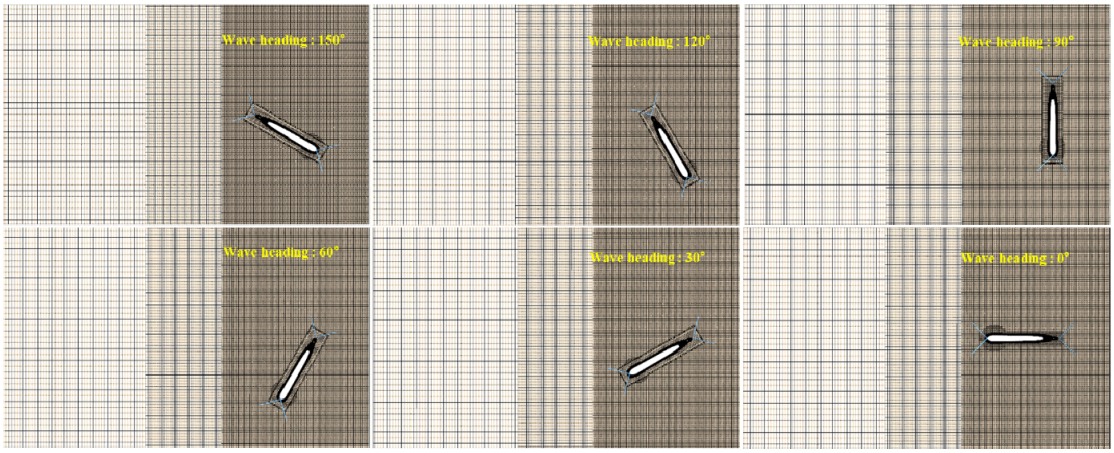

Fig. 8 Mesh distribution for quartering and following sea simulation

time step was selected to be able to perform 500 calculations per period based on the encounter period, and the calculation was performed so that the encounter period was repeated 10 time or more.

The mesh was made with a trimmed mesh in STAR-CCM+. Four prism layers were used to accurately measure the boundary layer flow on the hull surface, and the first layer thickness (Y+) was 10–40. The configuration of the mesh used in a regular wave simulation is shown in Fig. 7 and Fig. 8.

A grid convergence test was performed to find the optimal grid resolution for three grids based on Richardson extrapolation (ITTC Resistance Committee, 2017). For this purpose, it was performed on course, medium, and fine grids for heave, pitch, and roll RAOs. The three grids are determined by increasing the size of the grid with the refinement ratio (r_i). Based on the simulation time, a refinement ratio (r_i) of $\sqrt{2}$ was applied due to the hardware resource limitation. The number of grids corresponding to the course, medium, and fine grids are shown in Table 3, and the generated grids are shown in Fig. 9.

The heave, pitch, and roll RAOs are selected for grid convergence test: ship on regular waves, head sea (μ = 180º) and beam sea (μ = 90º). The both cases ship speed was 3 knots (1.54 m/s) and the results of grid convergence study are summarized in Table 4. The convergence ratio is defined by Eq. (1).

Table 3 Information of different types of grids for convergence test

Index	Reference size (m)	Number of grids
Coarse	0.1183	2.8M
Medium	0.1054	3.6M
Fine	0.0939	4.9M

$$R_G = \epsilon_{32}/\epsilon_{21} \tag{1}$$

where

S_1 = Coarse grid (2.8M)

S_2 = Medium grid (3.6M)

S_3 = Fine grid (4.9M)

$\epsilon_{21} = S_2 - S_1$: The difference of coarse and medium grids

$\epsilon_{32} = S_3 - S_2$: The difference of medium and fine grids

Convergence conditions are defined according to the convergence rate calculated by Richardson extrapolation as follows:

(1) $R_i > 1$: Grid divergence

(2) $R_i < 0$: Oscillatory convergence

(3) $0 < R_i < 1$: Monotonic convergence

As shown in Table 4, R_G for heave, pitch, and roll shows that monotonic convergence is achieved for all simulation variables because they are between 0 and 1. It is shown that the tendency of calculated results converge as the size of the grid is reduced. The order of accuracy p_G is defined by Eq. (2).

$$p_G = \frac{\ln\left(\frac{\epsilon_{32}}{\epsilon_{21}}\right)}{\ln(r_G)} \tag{2}$$

Based on Celik et al. (2008), the Grid Convergence Index (GCI) is defined using the following equations:

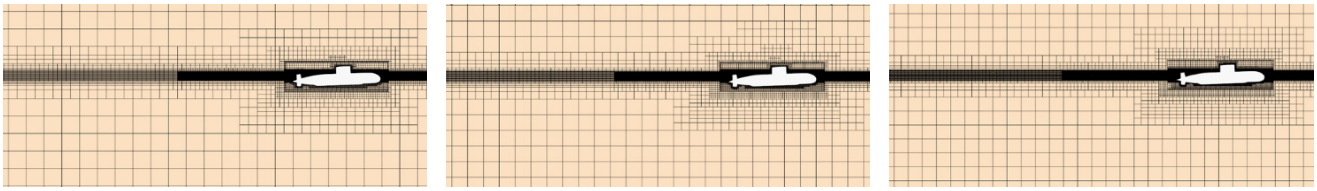

(a) (b) (c)

Fig. 9 Different grids on side view: (a) Coarse grid; (b) Medium grid; (c) Fine grid

Table 4 Grid convergence test results

	μ = 180º		μ = 90º	
Variable	Heave (m/m)	Pitch (º /m)	Heave (m/m)	Roll (º /m)
S1 (Coarse)	0.67	2.54	0.96	8.39
S2 (Medium)	0.76	2.87	0.99	8.62
S3 (Fine)	0.80	3.00	1.01	8.73
r_G	$\sqrt{2}$	$\sqrt{2}$	$\sqrt{2}$	$\sqrt{2}$
ϵ_{21}	0.093	0.332	0.028	0.235
ϵ_{32}	0.038	0.131	0.025	0.110
R_G	0.409	0.393	0.899	0.468
p_G	2.58	2.69	0.31	2.19
GCI_{fine}^{32}	0.029	0.021	0.025	0.008

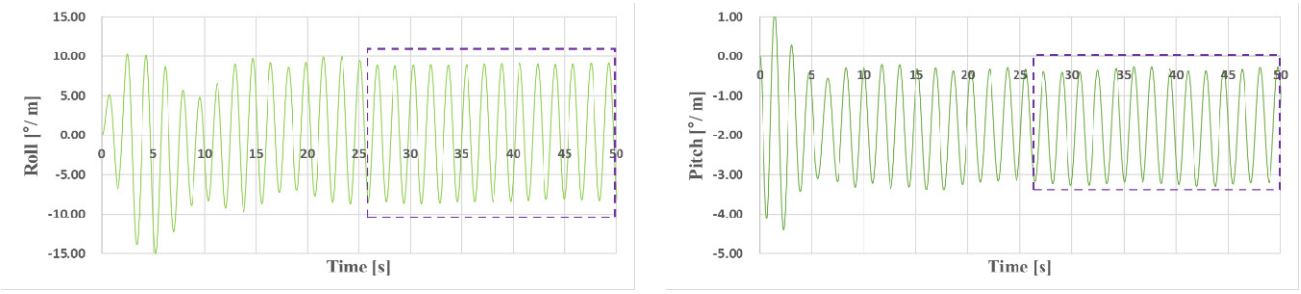

(a) (b)

Fig. 10 Time series of roll and pitch response in beam sea (λ/L = 1.0, rectangle box: available time history range): (a) Roll response; (b) Pitch response

$$GCI_{fine}^{32} = 1.25e_a^{32}/\left(r_{32}^{p}-1\right) \quad (3)$$

As shown in Table 4, the maximum GCI is 0.029 in heave motion and head sea, and the minimum GCI is 0.008 in roll motion and beam sea, all of which are within an acceptable range. In this study, grids of 4.9 million cells were used based on the grid convergence test, and 100 grids per wavelength and 16 grids per wave height were selected. From the CFD simulation, heave, roll, and pitch responses were obtained based on the earth-fixed coordinate system. Fig. 10 shows the time histories of the roll and pitch response. The motion RAOs were calculated from average of responses after the transient range, as shown in Fig. 10.

Figs. 11–13 show the motion RAOs obtained from the CFD simulation. The motion RAOs were normalized with the wave amplitude. Unlike the results of potential code, the maximum roll response was found in beam sea. The natural roll period was 8.3 seconds, which is a slightly smaller value compared with the target value (8.76 s). In the motion RAOs, the maximum values of heave and pitch were found in beam sea and head sea, respectively. As with the potential code, the heave and pitch RAOs from CFD simulation showed double peaks, which will be discussed later with the comparison results.

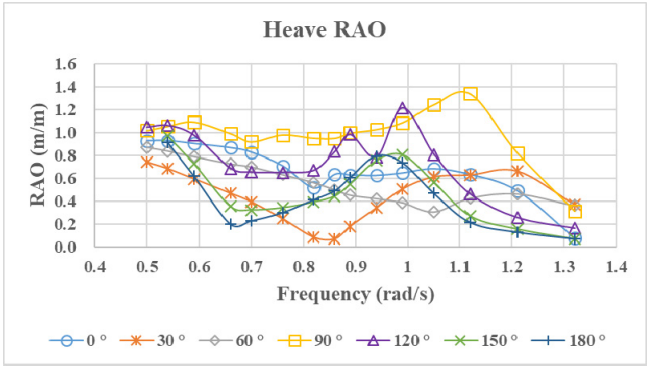

Fig. 11 Heave RAOs obtained from CFD simulation

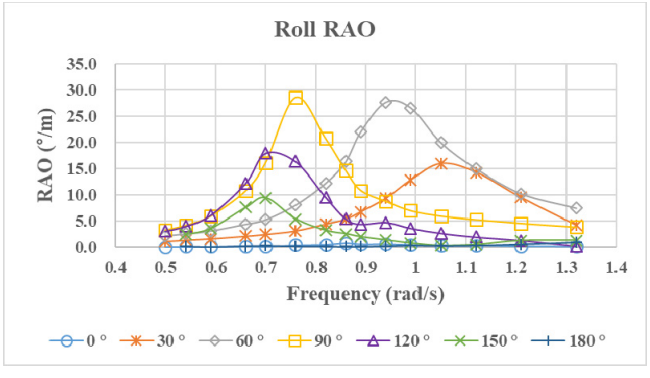

Fig. 12 Roll RAOs obtained from CFD simulation

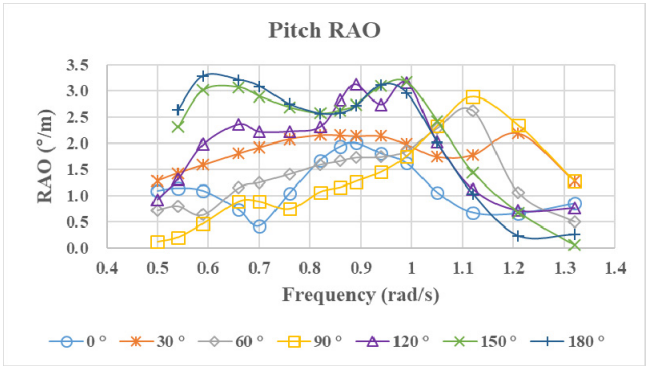

Fig. 13 Pitch RAOs obtained from CFD simulation

4. Comparison Results and Discussion

4.1 Motion RAOs

The simulation results (potential code and CFD) for motion RAOs were compared and validated with the model test results. As mentioned earlier, the model test results were obtained from a published paper (Hermanski and Kim, 2010). The comparison results with experimental data are shown in Fig. 14. Unfortunately, experimental data were available for only beam sea conditions. From the results, the roll RAOs of CFD show good agreement with experimental results at wave frequency > 0.76 rad/s. For low wave frequency (frequency < 0.76 rad/s), the roll RAOs of CFD show a smaller value than the experimental results. This result seems to be due to a small difference of roll natural period between the CFD results and experimental results.

On the other hand, roll RAOs obtained from potential code show a big deviation from experimental results. The pitch motion is not dominant in beam sea, but when compared within available

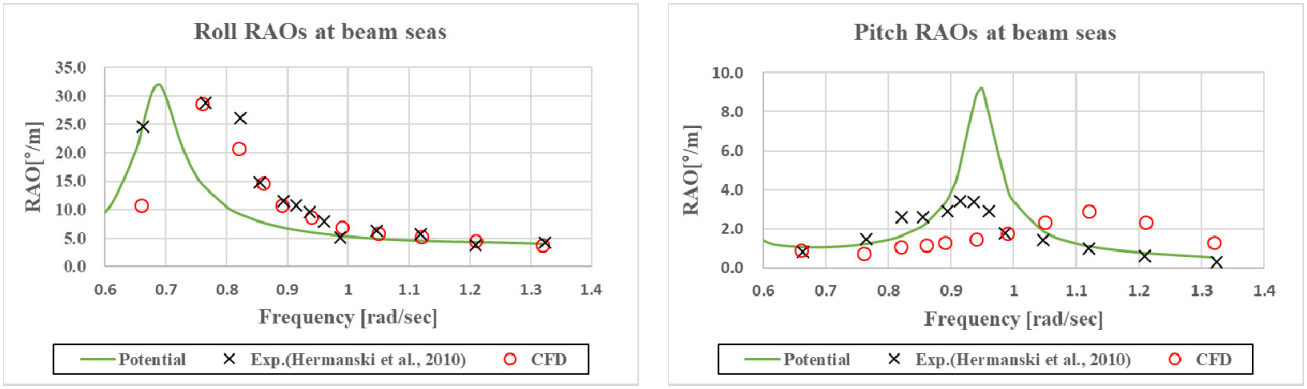

(a) (b)

Fig. 14 Comparison of roll and pitch RAOs (μ = 90º): (a) Roll RAO; (b) Pitch RAO

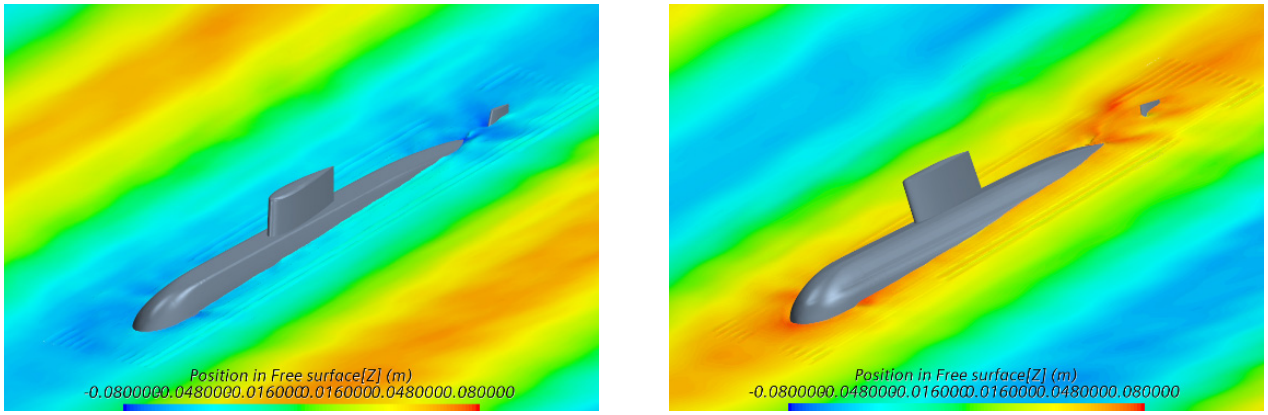

(a) (b)

Fig. 15 Wave contours on free surface from CFD simulation (μ = 90º): (a) t = 42 s ; (b) t = 45 s

experimental data, the results of the potential code showed a big difference compared to the experimental results in the resonance frequency range. These differences might be due to nonlinear effects, which quickly become important due to the particular body geometry close to waterline. As shown in the CFD results (Fig. 15), the wetted surface area on the free surface changes dramatically, especially in the stern area, but the potential code does not take this into account.

4.2 Motion Response

Quantitative comparison of estimated motion responses was performed. The motion responses in irregular waves can be obtained by spectral analysis employing the motion RAOs and generated wave spectrum. In this study, a Joint North Sea Wave Project spectrum for fetch-limited seas was used, and the parameters are summarized in Table 5.

The estimated motion responses are shown in Figs. 16–18. The roll motion responses are compared in Fig. 16. As can be seen from Fig. 16, roll motions from the CFD code showed similar trends to the experimental results, while the roll motions from the potential code showed significantly larger values than the experimental results, and the tendency is different. These differences might be due to nonlinear effects, which quickly become important due to the particular body geometry close to the waterline.

The pitch motion responses are compared in Fig. 17. The pitch motion response from CFD code showed good agreement with experimental results except for the wave heading of 30º. On the other hand, pitch motion responses obtained from the potential code were significantly bigger than the experimental results for sea states 5 and 6.

Finally, the heave motion responses are compared in Fig. 18. From Fig. 18, it was found that heave motions from potential code were overestimated, and those from CFD code were underestimated

Table 5 Simulation conditions for irregular waves

Sea state	Significant wave height (H_s)	Wave peak period (T_p)	Gamma factor
Sea state 4 (SS4)	1.88 m	7.5 s	
Sea state 5 (SS5)	3.25 m	9.7 s	3.3
Sea state 6 (SS6)	5.00 m	12.4 s	

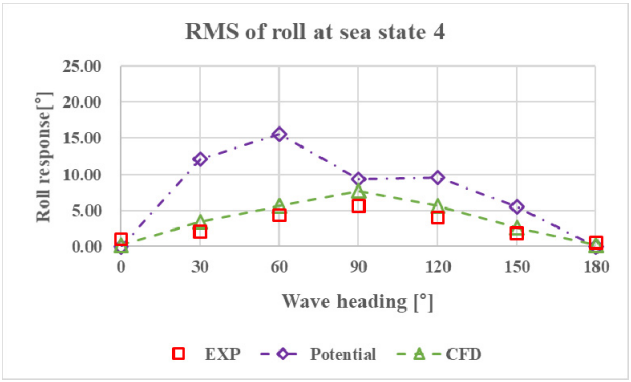

(a)

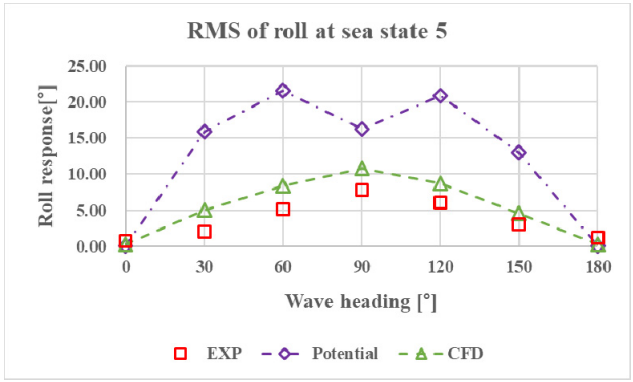

(b)

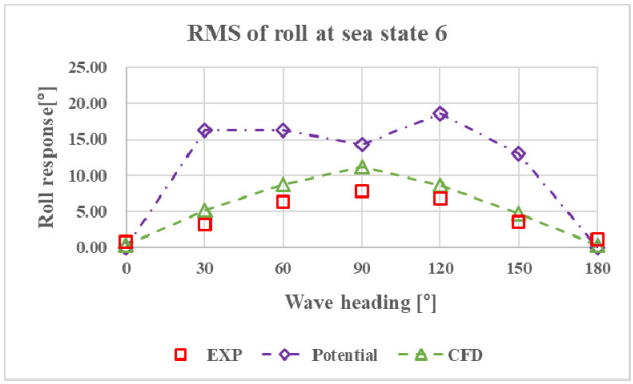

(c)

Fig. 16 Comparison of roll motion responses: (a) Roll motions at SS4; (b) Roll motions at SS5; (c) Roll motions at SS6

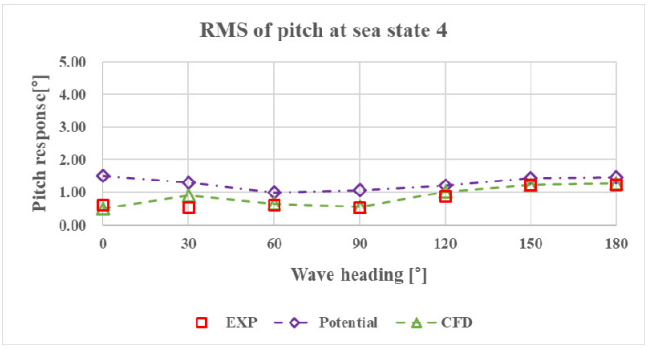

(a)

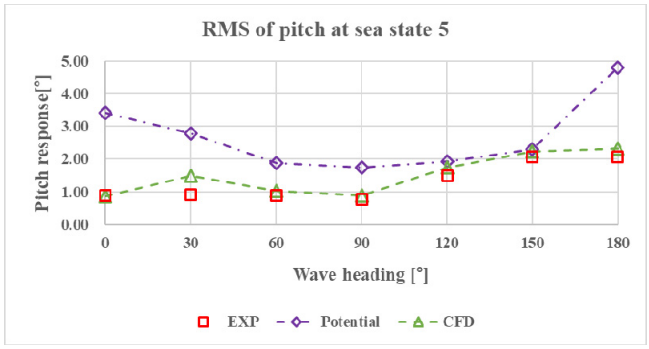

(b)

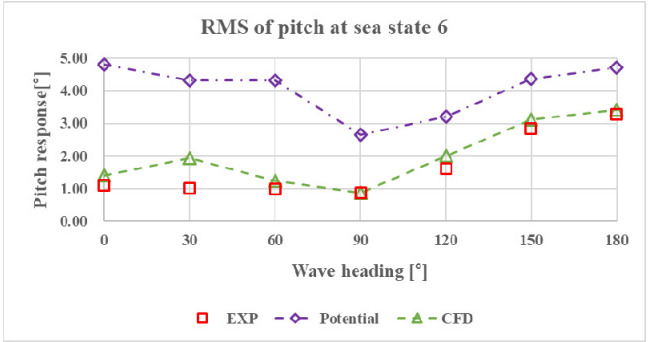

(c)

Fig. 17 Comparison of pitch motion responses: (a) Roll motions at SS4; (b) Roll motions at SS5; (c) Roll motions at SS6

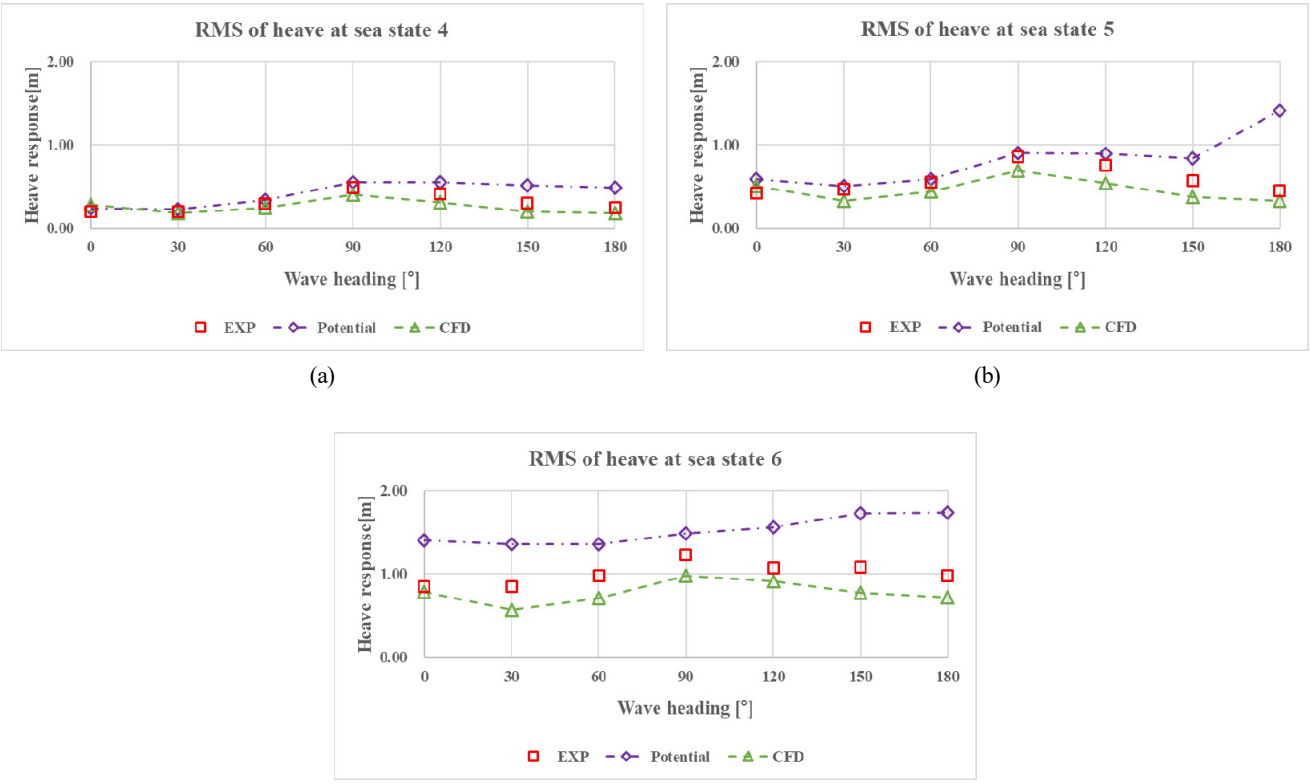

Fig. 18 Comparison of heave motion responses: (a) Heave motions at SS4; (b) Heave motions at SS5; (c) Heave motions at SS6

compared with the experimental results. Although heave motion from CFD code was underestimated from the experimental results, the difference was small, and the heave motions showed a similar tendency to the experimental results.

From these comparison results, it was found that the seakeeping analysis using CFD code gives good results compared with those of potential code. Therefore, the seakeeping analysis based on the CFD code can be a good solution for estimating the seakeeping performance of submarines in free surface conditions. In addition, as the sea state increased, the overall difference between motion responses from CFD code and experimental results slightly increased. These differences might be due to nonlinear effects from stern area flooded by waves, as shown in Fig. 19.

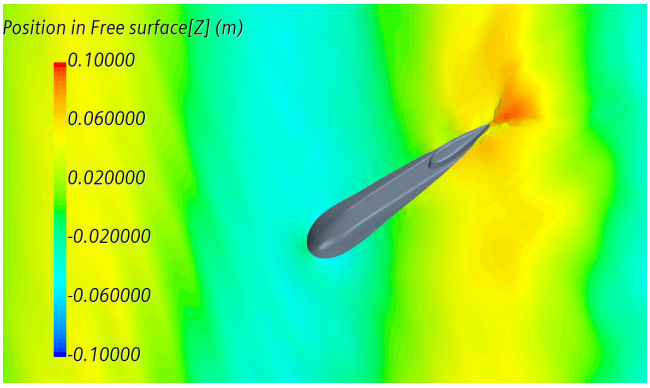

Fig. 19 Wave contour on free surface from CFD simulation (μ = 30°)

According to DNV-RP-C103 (DNV, 2005), the flow of water on top of the pontoons with nonlinear effects for transit conditions is not taken into account in a linear calculation. The primary results of these nonlinear effects are reduced heave, pitch, and roll motions near resonance (Recommended practice DNV-RP-C103, 2005). In this study, the seakeeping analysis was carried out using a spectral method from the motion RAOs based on linear calculation. Therefore, in the future, it is necessary to apply direct estimation in irregular waves to further improve the calculation accuracy.

5. Conclusion

In this study, seakeeping performance of a submarine in free surface conditions was evaluated by CFD code and potential code. Estimated results were compared with experimental results, and the following conclusions were made.

(1) From the results, the roll RAOs from CFD code showed good agreement with experimental results except at low wave frequency.

(2) Motion responses from CFD code showed similar trends to experimental results, while motion responses from potential code showed significantly larger values than experimental results. These differences might be due to nonlinear effects, which quickly become important due to the particular body geometry close to the waterline.

(3) From these comparison results, it was found that seakeeping analysis based on the CFD code can be a good solution for estimating the seakeeping performance of submarines in free surface conditions.

Conflict of Interest

No potential conflict of interest relevant to this article was reported.

Funding

This research was supported by "the development and demonstration of data platform for AI-based safe fishing vessel design (20220210)" of the Ministry of Oceans and Fisheries, Republic of Korea.

References

Bingham, H. B. (1994). *Simulating ship motions in the time domain* [Doctoral dissertation, Massachusetts Institute of Technology]. MIT Libraries. http://hdl.handle.net/1721.1/12320

Burcher, R. K., & Rydill, L. J. (1995). *Concepts in submarine design* (1st ed.). Cambridge University Press.

BV. (2019). *HydroStar for experts user manual*. Bureau Veritas.

Cansiz, M. Y., & Yildiz, B. (2021). Mathematical model of roll decay motion for a surfaced submarine. *GMO Journal of Ship and Marine Technology,* (219), 107−123. https://dergipark.org.tr/en/pub/gdt/issue/63160/948683

Celik, I. B., Ghia, U., Roache, P. J., Freitas, C. J., Coleman, H., & Raad, P. E. (2008). Procedure for estimation and reporting of uncertainty due to discretization in CFD application. *Journal of Fluids Engineering, 130*(7), 078001. https://doi.org/10.1115/1.2960953

DNV. (2005). *Recommended practice* (DNV-RP-C103). Det Norske Veritas.

Gerritsma, J., & Beukelman, W. (1972). Analysis of the resistance increase in waves of a fast cargo ship. *Intenational Shipbuilding Progress, 19*(217), 285−293. https://doi.org/10.3233/ISP-1972-1921701

Hedberg, S. (2006). *Investigation of submarine roll behaviour* [Master's thesis, KTH Royal Institute of Technology]. https://www.kth.se/polopoly_fs/1.213390.1600688853!/Menu/general/column-content/attachment/report.pdf

Hermanski, G., & Kim, S. (2010). Surface seakeeping experiments with model of a submarine. *11th International Symposium on Practical Design of Ships and Other Floating Structures, PRADS 2010*, Rio de Janeiro, Brazil, 19577550.

ITTC Resistance Committee. (2017). Uncertainty analysis in CFD verification and validation methodology and procedures. *ITTC − Recommended Procedures and Guidelines*, 1−13.

Jung, D. J., & Kim, S. H. (2022, October 9−13). Study of sunmarine seakeeping performance at free surface condition in regular waves. *15th International Symposium on Practical Design of Ships and Other Floating Structures, PRADS 2022*, Dubrovnik, Croatia.

Kring, D. C. (1994). *Time domain ship motions by a three-dimensional rankine panel method* [Doctoral dissertation, Massachusetts Institute of Technology].

Krishna, G. Das., & Krishnankutty. P. (2016). Roll motion control of submarines at free surface using juxtapositioned stern planes. *International Seminar on Current and Future Challenges in Design and Construction of Underwater Vehicles*, 74−110.

Thornhill, E., & Hermanski, G. (2008). Numerical and experimental analysis of surfaced submarine roll decay behavior. *Journal of Ocean Technology*, *Ocean Sovereignty, 3*(1), 91−100. https://www.thejot.net/article-preview/?show_article_preview=85&jot_download_article=85

Vogels, R.H. (2016). *On the roll damping of surfaced submarines* [Master's thesis, Delft University of Technology].

Author ORCIDs

Author name	ORCID
Jung, Doojin	0000-0001-8653-7236
Kim, Sanghyun	0000-0002-3625-2328

KSOE

Journal of Ocean Engineering and Technology 36(5), 313-325, October, 2022
https://doi.org/10.26748/KSOE.2022.024

pISSN 1225-0767
eISSN 2287-6715

Original Research Article

Prediction of Wave Transmission Characteristics of Low Crested Structures Using Artificial Neural Network

Taeyoon Kim[1], Woo-Dong Lee[2], Yongju Kwon[3], Jongyeong Kim[3], Byeonggug Kang[3] and Soonchul Kwon[4]

[1]*Research Professor, Department of Ocean Civil Engineering, Gyeongsang National University, Tongyeong, Korea*
[2]*Professor, Department of Ocean Civil Engineering, Gyeongsang National University, Tongyeong, Korea*
[3]*Student, Department of Civil Engineering, Pusan National University, Busan, Korea*
[4]*Professor, Department of Civil Engineering, Pusan National University, Busan, Korea*

KEY WORDS: Artificial neural network, Wave transmission, Coastal engineering, Prediction, Sensitivity analysis

ABSTRACT: *Recently around the world, coastal erosion is paying attention as a social issue. Various constructions using low-crested and submerged structures are being performed to deal with the problems. In addition, a prediction study was researched using machine learning techniques to determine the wave attenuation characteristics of low crested structure to develop prediction matrix for wave attenuation coefficient prediction matrix consisting of weights and biases for ease access of engineers. In this study, a deep neural network model was constructed to predict the wave height transmission rate of low crested structures using Tensor flow, an open source platform. The neural network model shows a reliable prediction performance and is expected to be applied to a wide range of practical application in the field of coastal engineering. As a result of predicting the wave height transmission coefficient of the low crested structure depends on various input variable combinations, the combination of 5 condition showed relatively high accuracy with a small number of input variables defined as 0.961. In terms of the time cost of the model, it is considered that the method using the combination 5 conditions can be a good alternative. As a result of predicting the wave transmission rate of the trained deep neural network model, MSE was 1.3×10^{-3}, I was 0.995, SI was 0.078, and I was 0.979, which have very good prediction accuracy. It is judged that the proposed model can be used as a design tool by engineers and scientists to predict the wave transmission coefficient behind the low crested structure.*

1. Introduction

As climate change causes sea levels to rise, which increases the external forces of high waves, shoreline deformation with coastal erosion and scour has received significant attention, becoming an important social issue in many countries. In particular, morphological changes in seabed due to such coastal erosion and sedimentation can cause changes in the coastal environment and ecosystems. Various deformation methods have been proposed to recover coastal erosion issues, but commercially utilized gravity-type structures such as breakwaters and headlands change the sea environment, resulting in bad seawater circulation and poor water quality. Low-crested and submerged structures (LCS), such as detached breakwater and artificial reefs, diminish the wave height with reduced wave energy behind a structure due to the change in the freeboard at the still water surface, which protects the inland sea environment. The construction of LCS is performed under specific conditions to produce the desired wave transmission coefficient; thus, the calculation or prediction of the transmission coefficient of the structure should be carried out as an important factor in designing the structure. To determine the wave transmission coefficient of LCS, various studies have proposed formulas for calculating the wave transmission rate, but the wave transmission coefficients are estimated through a regression analysis of mathematical experimental data, showing a limited analysis of the natural phenomena (Koosheh et al., 2020; Formentin et al., 2017). Recently, a machine learning model has been used to estimate and predict statistical structures from input and output data. This machine learning model can readily explain the regression analysis of nonlinear relationships (Hashemi et al., 2010; Rigos et al., 2016). Machine-learning-based prediction models employ deep learning algorithms of neural networks, which have been continuously applied in the field of coastal engineering in recent years, especially for solving problems

Received 21 July 2022, revised 7 September 2022, accepted 20 September 2022
Corresponding author Soonchul Kwon: +82-51-510-7642, sckwon@pusan.ac.kr

related to modeling behavior around coastal structures (Shamshirband et al., 2020; Kim et al., 2005; Formentin et al., 2017; Panizzo and Briganti, 2007).

Herein, we introduced a prediction trend of the wave attenuation characteristics of LCS to propose an explicit method composed of weights and biases using artificial neural network. To estimate dominant factors for the wave transmission rate of LCS, we applied machine learning models to predict the wave height transmission rate of LCS dependent on 7 types of dimentionless characters with sensitivity analysis. In addition, we proposed an optimized machine learning model suitable for the determination of wave transmission coefficient and performs an overall analysis of the model with various combination. Finally, we carried out the evaluation of the applicability of the machine learning model through the analysis of the accuracy associated with the formulas for calculating the wave height transmission rate of the existing LCS. We found that the estimated wave attenuation characteristics calculated with the presented weight and bias matrix shows better accurate reliability compared with those obtained from the broadly used empirical formula.

2. Background

2.1 Analysis of Transmission Coefficient Empirical Formulas

Among various studies, Takayama et al.(1985) proposed the Eq. (1) to determine the wave transmission coefficient for LCS based on empirical experiment using irregular wave as follows:

$$K_T = -0.92\left(\frac{B}{L_0}\right) + 0.42\left(\frac{R_C}{H_0'}\right) + 3.80\left(\frac{H_0'}{L_0}\right) + 0.51 \tag{1}$$

where B is the crown width, R_C is the crown freeboard, L_0 is deep sea wave length , H_0' is calculated wave height of deep sea. When the relative width of structure increases over a certain value, the value of wave transmission coefficient at $B/L_0 > 0.7$ is defined as a negative value based on the result of Takayama et al.'s(1985) experiment, which was determined using a small with of structure ($B/L_0 < 0.4$) (Lee and Bae, 2020). Thus, it is suitable for an experiment with a short wave period length. In DELOS (Environmental Design of Low Crested Coastal Defence Structures, EVK3-CT-2000-00041) project, more than 2300 two-dimensional experiments were performed to determine the wave transmission coefficient for LCS. Van der Meer et al. (2005) proposed the experimental formula to estimate the wave transmission coefficient using converted dimensionless variables of relative freeboard (R_C/H_i), relative crest width (B/H_i), surf similarity parameter ($\xi = \tan\alpha/\sqrt{H_i/L_0}$) obtained from DELOS as follows:

$$K_T = -0.3\left(\frac{R_C}{H_i}\right) + 0.75\left(1 - e^{-0.5\xi}\right), \xi < 3 \tag{2}$$

$$K_T = -0.3\left(\frac{R_C}{H_i}\right) + 0.75\left(\frac{B}{H_i}\right)^{-0.31}\left(1 - e^{-0.5\xi}\right), \xi > 3 \tag{3}$$

where $\tan\alpha$ is breakwater slope and effective range of wave transmission coefficient is determined between 0.075 and 0.8.

Goda and Ahrens (2009) proposed the formula of wave transmission coefficient for LCS as follows.

$$K_T = \max\left\{0, \left(1 - \exp\left[a\left(\frac{R_C}{H_i} - F_0\right)\right]\right)\right\} \tag{4}$$

$$a = 0.248\exp\left[-0.384\ln\left(\frac{B_{eff}}{L_0}\right)\right] \tag{5}$$

$$F_0 = \begin{cases} 1.0 & : D_{eff} = 0 \\ \max\{0.5, \min(1.0, H_i/D_{eff})\} & : D_{eff} > 0 \end{cases} \tag{6}$$

where F_0 is dimensionless limit wave run-up height, D_{eff} is the effective diameter of the materials composed of LCS.

$$B_{eff} = \begin{cases} B_{swl} & emerged crest \\ \frac{9}{10}B + \frac{1}{10}B_0 & zero freeboard \\ \frac{8}{10}B + \frac{2}{10}B_0 & submerged crest \end{cases} \tag{7}$$

Herein, B_{eff} is effective crest width at still water level, B_{swl} is the width of structure at still water level, B is the crest width of structure, B_0 is the width at the bottom of structure.

Calabrese et al. (2003) used the large-scale experimental data to determine the wave transmission coefficient.

$$K_T = a\frac{R_C}{B} + b \tag{8}$$

$$b = \alpha \times exp\left(-0.0845\frac{B}{H_i}\right) \tag{9}$$

$$\alpha = 1 - 0.562\exp(-0.0507\xi) \tag{10}$$

$$a = \beta \times exp\left(0.2568\frac{B}{H_i}\right) \tag{11}$$

$$\beta = 0.6957 \times \frac{H_i}{h} - 0.7021 \tag{12}$$

2.2 Artificial Neural Network

Artificial neural network (ANN) is modeling systems that provides a data process structure inspired by the neural networks of human brains, which are composed of a web of millions of interconnected neurons. A neuron is a special biological cell that conveys information from one neuron to others. ANN is composed of a large number of simple processing elements interconnected with each other. The system requires the involvement of a labeled direct graph structure where nodes conduct computations. The "directed graph" provides a set of "nodes" (vertices) and a set of "connections" (edges/links/arcs) to connect pairs of nodes. In a neural network, each node performs simple computations, and each connection delivers a signal from one

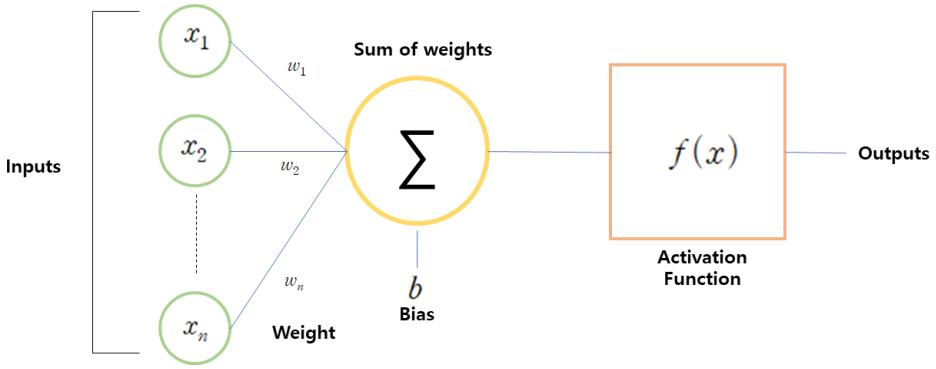

Fig. 1 Neural network diagram of element

node to another, labeled by a number called the "connection strength" or "weight", which implies the extent to which a signal is amplified or diminished by connection, as shown in Fig. 1.

In the ANN data process, the result values are derived by substituting the normalized input variable into the function of Eq. (13) at each node.

$$N_j = \sum_{i=1}^{N_c} w_{ij} x_i + \theta_j \tag{13}$$

where w is weight), θ is Bias, x is input value.

2.2.1 Activation function

The activation function provides the explanation of non-linearity by substituting the estimated input data in each node into a function that creates non-linearity and then outputs the results. Different kinds of functions, such as linear, exponential, sigmoid, tanh, rectified linear unit (ReLU), softmax, scaled exponential linear unit (SeLU), and expoenetial linear unit (elU) are utilized for the activation function. The mean squared error of the various functions where six different activation functions are described to the hidden layer and output layer as shown in Fig. 2.

2.2.2 Gradient decent method

In general, the error back propagation method is used as an optimization algorithm for parameter estimation, which re-updates any parameter to the one with the lowest error. The period in which each parameter is updated once is called the weight adjustment period (epoch). Here, the error backpropagation refers to the process of minimizing the error by re-correcting the weight while going backwards the result of the sum of the errors of each neuron. For the optimization of the loss function, the gradient descent method was developed by re-updating the weights to find the lowest point of the lost value. The existing gradient descent method can accurately derive

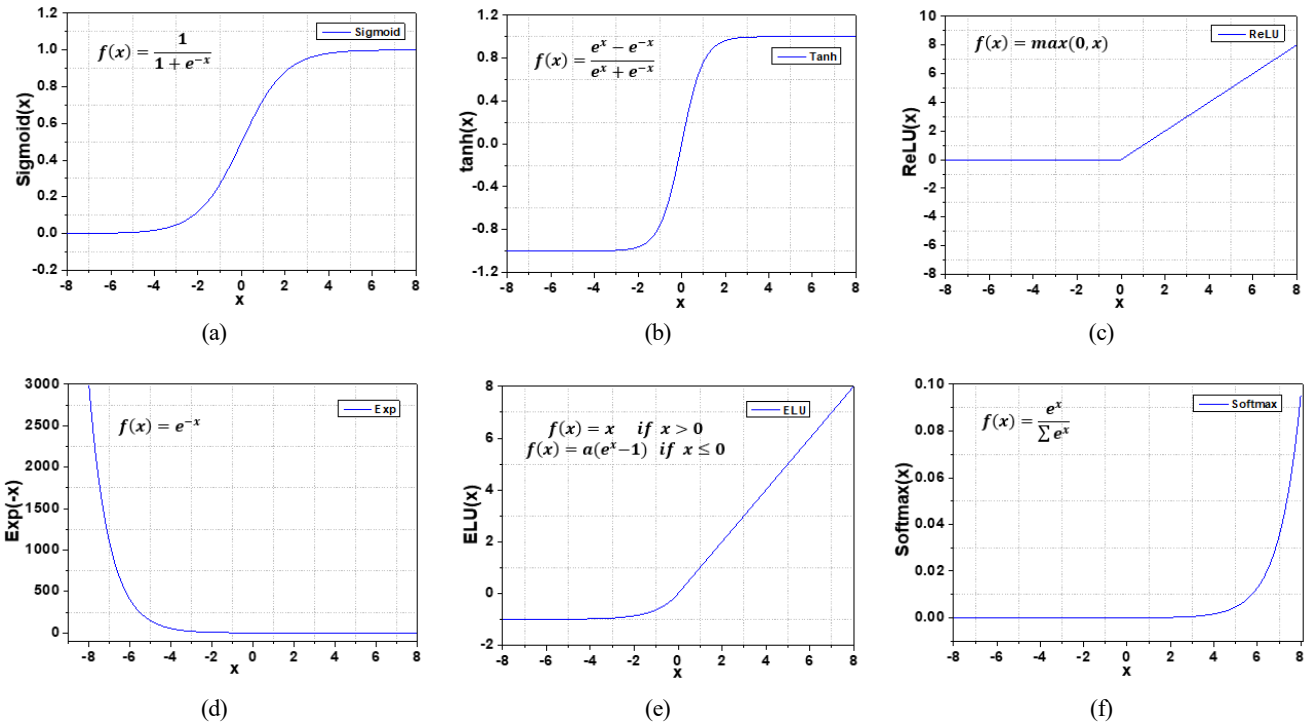

Fig. 2 Type of activation functions: (a) Sigmoid type; (b) Tanh type; (c) ReLU type; (d) Exponential type; (e) eLU type; (f) Softmax type

weights, but it has a disadvantage in that the amount of calculation is very large because it must be differentiated over the entire data instantaneously whenever the weights are changed. That is, the speed may decrease due to the load caused by a large amount of computation, and learning may be stopped before additionally finding the optimal solution. To compensate for this problem, various advanced gradient descent techniques have been developed. Advanced gradient descent techniques include stochastic gradient descent (SGD), momentum, Nesterov accelerated gradient, Adagrad, and root mean square propagation (RMSProp), Adam, etc., and in this study, the optimization process using Adam was performed. Adam is a gradient descent method that combines Momentum and RMSprop techniques, and uses the exponential average of the squares of the slopes of the RMSprop technique. is as follows (Eqs. (14)–(16)).

(1) Stochastic gradient descent (SGD)

The stochastic gradient descent method consists of a set of parameters to be updated through the calculation of the change rate of the loss function (E) and the learning rate (η) shown in Eq. (14).

$$W_{t+1} = W_t - \eta \frac{1}{\sqrt{\hat{h}_t + \epsilon}} \hat{m}_t \tag{14}$$

Here, W is a weight, η is a learning rate, E is an error, and is a method of updating weights according to a constant learning rate (η) using some randomly extracted data.

(2) Adaptive gradient, Adagrad

In the adaptive gradient method, the learning rate is adjusted according to the number of updates of the variable by h_t when the weights are re-updated, and the weights are trained to reach the optimal value. It is a method of learning by decreasing the learning rate for variables that have changed significantly and increasing the learning rate for variables with small changes (Eqs. (15), (16)).

$$W_{t+1} = W_t - \eta \frac{1}{\sqrt{h_t}} \frac{\partial E}{\partial W_t} \tag{15}$$

$$h_t = h_{t-1} + \left(\frac{\partial E}{\partial W_t} \right)^2 \tag{16}$$

Here, for weight update, the learning rate is multiplied by $\frac{1}{\sqrt{h_t}}$, and h_t is the continuous sum of the squares of the slope of the loss function. In addition, in the existing gradient descent method, the addition of the squares of the weight gradients causes the learning rate to decrease gradually for the weights that have a lot of fluctuations in the weight values. However, if Adagrad learns infinitely, at some point h becomes too large and the learning rate becomes 0 and learning is stopped. That is, it works well for the problem of the cost function composed of a simple quadratic equation, but it has a problem that the learning rate is too reduced and the learning stops completely before reaching the global minimum.

(3) RMSprop

In the complex structure of Adagrad, there is a problem that the learning rate becomes 0 before reaching the global minimum. To compensate for this, the RMSprop technique was developed (Eqs. (17), (18)). This method improved the existing problems by reflecting and accumulating the latest slope information using the Decaying mean.

$$W_{t+1} = W_t - \eta \frac{1}{\sqrt{h_t + \epsilon}} \frac{\partial E}{\partial W_t} \tag{17}$$

$$h_t = \rho h_{t-1} + (1-\rho) \left(\frac{\partial E}{\partial W_t} \right)^2 \tag{18}$$

Here, ρ is added to the h_t parameter, which usually uses a value of 0.9 as the attenuation rate, and functions to reflect the latest gradient information rather than simply accumulating the weight gradient.

(4) AdaDelta (Adaptive delta)

AdaDelta is calculated using the Hessian matrix instead of the learning rate to compensate for the problem of small learning rate in Adagrad, and is calculated as follows Eqs. (19)–(22).

$$W_{t+1} = W_t - \triangle\theta_t \tag{19}$$

$$\triangle\theta_t = \frac{\sqrt{v_t} + \epsilon}{\sqrt{h_t} + \epsilon} \frac{\partial E}{\partial W_t} \tag{20}$$

$$h_t = \rho h_{t-1} + (1-\rho) \left(\frac{\partial E}{\partial W_t} \right)^2 \tag{21}$$

$$v_t = \rho v_{t-1} + (1-\rho) \triangle\theta_t^2 \tag{22}$$

(5) Adam (Adaptive moments)

Adam uses the exponential averaging of the square of the slope of the RMSprop technique as a gradient descent method that combines the Momentum and RMSprop techniques (Eqs. (23)–(25)).

$$W_{t+1} = W_t - \eta \frac{1}{\sqrt{\hat{h}_t + \epsilon}} \hat{m}_t \tag{23}$$

$$\hat{m}_t = \frac{m_t}{1-\beta_1^t}, \quad m_t = \beta_1 m_{t-1} + (1-\beta_1) \frac{\partial E}{\partial W_t} \tag{24}$$

$$\hat{v}_t = \frac{v_t}{1-\beta_2^t}, \quad v_t = \beta_2 v_{t-1} + (1-\beta_2) \left(\frac{\partial E}{\partial W_t} \right)^2 \tag{25}$$

Here, m_t is the estimate for the first moment of the gradient, v_t is the estimate for the second moment, and β_1 and β_2 are the correction values that correct the deviation of the weights.

3. Methodology

3.1 Experimental Database

It is required to consider various valuables to determine the wave transmission characteristics behind the LCS structure. The optimal machine learning model was used to figure out the role of variables affecting the wave control of LCS using the machine learning analysis package. We used the results of previous hydraulic experiment with LCS for input data, including deep sea wave length (L_0), crest freeboard (R_C), incident wave height (H_0), crown width (B), water depth (h), structure height (h_c), wave period (T_0), similarity coefficient for breakwater ($\tan\alpha$) and Dn_{50}(Seelig, 1980; Daemrich and kahle, 1985; van der Meer, 1988; Daemen, 1991) (Table 1). Data was obtained from DELOS databased of submerged breakwater information.

- 81 data on rubble mound emerged/submerged breakwater [Seelig];
- 95 data on tetrapod submerged breakwater [Daemrich and Kahle];
- 31 data on rubble mound emerged/submerged breakwater [Van der Meer];
- 53 data on rubble mound emerged/submerged breakwater [Daemen]

When applying the results of the mathematical model experiment, applying a dimensionless factor helps to clarify the problem related to the scale effect. Therefore, we applied 7 dimensionless factors as input variables as shown in Table 2 in consideration of the above dimension factors.

$$K_T = f\left\{\frac{R_C}{H_0}, \frac{B}{H_0}, \xi, \frac{B}{L_0}, \frac{R_C}{h}, \frac{Dn_{50}}{h_c}, \frac{h_c}{h}\right\} \tag{26}$$

where R_C/H_0 is the relative freeboard, B/H_0 is the relative crest width, ξ is the surf similarity parameter, B/L_0 is the ratio of the crest width to the wavelength, R_C/h is the ratio of the crest height to the water depth, Dn_{50}/h_c is the ratio of the nominal diameter to the crest height, and h_c/h is the relative crest height. To reflect the same degree of feature scale, we converted the input variable using max-min normalization.

$$x_n = \frac{x - \min(x)}{\max(x) - \min(x)} \tag{27}$$

3.2 Hyperparameters Tuning and Model Validation

A machine learning model has many hyperparameters that the user

Table 1 Ranges of parameter of reference

	R_C		B		h		Dn_{50}		$\tan\alpha$		H_0		T_0	
	Min	Max	Min	Max	Min	Max	Min	Max	Min	Max	Min	Max	Min	Max
Seelig (1980)	-0.42	0.21	0.30	0.40	0.45	0.85	0.11	0.16	0.38	0.67	0.02	0.18	0.91	3.66
Damrich and Kahle (1985)	-0.20	0	0.20	1.00	0.50	0.70	0.08	0.08	0.50	0.50	0.02	0.23	1.23	3.27
Van der Meer (1988)	-0.10	0.13	0.3	0.3	0.4	0.4	0.03	0.03	0.5	0.5	0.08	0.23	1.94	2.60
Daemen (1991)	-0.09	0.20	0.34	0.34	0.27	0.52	0.04	0.06	0.67	0.67	0.03	0.15	0.98	2.88

Table 2 Definitions and ranges of scaled model parameter

Parameter		Definition	Average	Max	Min
X_1	R_C/H_0	Relative freeboard	-0.494	4.00	-8.696
X_2	B/H_0	Relative crest width	4.525	43.478	0.889
X_3	ξ	Surf similarity parameter	4.145	10.541	1.181
X_4	B/L_0	Ratio of the crest width to wave length	0.09	0.424	0.012
X_5	R_C/h	Ratio of the crest height to the water depth	-0.065	0.36	-0.56
X_6	Dn_{50}/h_c	Ratio of the nominal diameter to crest height	0.166	0.336	0.065
X_7	h_c/h	Relative crest height	0.935	1.734	0.44
Y	K_T	Transmission coefficient	0.482	0.922	0.049

Table 3 Hyperparameter tuning

Hyper parameter	Range of hyperparameter	Number of hyperparameter
Hidden layer	1-2	2
Activation function of hidden layer	ReLU, Sigmoid, Tanh, Exponential	4
Hidden neuron	7-35 (15)	15
Output layer	1	1
Activation function of output layer	Sigmoid, Linear	2
Optimizer	SGD, Adadelta, Adagrad, Adam	4

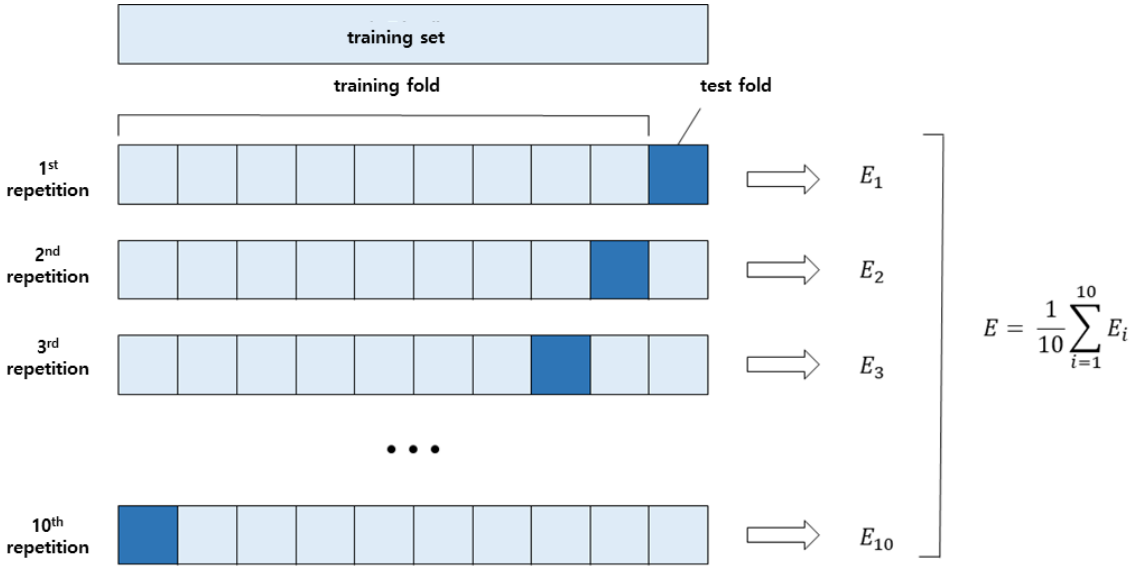

Fig. 3 10-fold cross validation

needs to specify. It is used to optimize performance by balancing bias and variance of machine learning models. Random search cross-validation (CV) and grid search CV are methods for deriving hyperparameters suitable for models and data. In this study, the optimal parameters for predicting the wave height attenuation characteristics of low-rise structures were derived using grid search CV. Table 3 shows the parameters and ranges applied to the grid search CV, and the parameter with the highest accuracy was derived through the calculation of a total of 960 cases.

The purpose of a machine learning model is to predict with high accuracy on new data, and to ensure generalization and reliability of model performance on new data. Cross-validation is a method to improve the generalization performance of a model and is generally a more reliable and superior statistical evaluation method than dividing the training set and test set once. The most widely used cross-validation method is k-cross-validation, which was developed to minimize the bias associated with random sampling of the training set. In this study, 10-fold cross validation was performed, the entire data sample was divided into 10, 9 were used for training and 1 was used for model validation, and cross-validation was performed 10 times in a row (Fig. 3).

3.3 ANN Model Setup

Table 4 shows ANN model setup. In this study, we utilized the 260 sets of wave input data with reference to the results of the hydraulic model experiment with existing low crest structures. Of the total 260 data, we used 70% as training data and 30% as prediction data. To set up the prediction model of wave properties with high accuracy using LCS method, various hyperparameters were determined under different conditions, including the activation function, gradient descent technique, hidden layer, and overfitting prevention technique, to build a model with low error and high accuracy. With respect to the activation functions of the hidden layer and the output layer, optimal activation functions (ReLU, Sigmoid) were applied using various model prediction results. We applied the calculated value to the hidden layer's activation function (ReLU) to explain non-linearity. We calculated the result by substituting the hidden layer calculation result into the function of output layers and output the result value by inputting it into the activation function (Sigmoid) of the output layer. To verify the model performance, we applied 10-fold cross-validation method that was developed to minimize the bias associated with random sampling of the training set.

The neural network derives an optimal weight and bias where the mean squared error (MSE) is minimized through the error backpropagation method. In the process of weight redistribution using backpropagation algorithm, the increase in the number of hidden layers and hidden nodes improves the model's performance, but increases training costs. Thus, this study determined various

Table 4 Model setup of ANN model

Total data	260
Training set	182
Test set	78
Normalization	Max-Min normalization
Input neuron	7
Hidden layer (Activation function)	1-2 (ReLU)
Hidden neuron	7-35
Output layer (Activation function)	1 (Sigmoid)
Epoch	10,000
Batch_size	200
Optimizer	Adam
Loss	Mean squared error
Overfitting prevention	Early stopping callback

hyperparameters with respect to the number of hidden layers and hidden neurons. We analyzed model accuracy (R^2) under the condition of the 1st–3th layers and 7–35 hidden neurons at hyperparameters.

When building a neural network, the optimal training time and prediction performance are obtained by varying the number of hidden layers and neurons. Fig. 4 reveals the R^2 results for the training set and the test set for the hidden neuron under the condition of different hidden layers, which shows trend lines with R^2 values with respect to the number of hidden layers and hidden neurons for training data. It represents that the model accuracy increases with the increase in the numbers of hidden layers. In addition, R^2 value of the training set gradually increases as the number of hidden neurons increases. On the other hand, the model accuracy of the test set increases as the number of hidden layers increases under certain condition (Fig. 5). The R^2 value (0.979) of the test set showed the highest accuracy under the condition of 29 hidden neurons with 2 hidden layers, which suggests that the model accuracy of the test set does have a high relationship with the accuracy of training set under certain condition. Thus, we constructed the model under the optimum condition of 29 hidden neurons with 2 hidden layers.

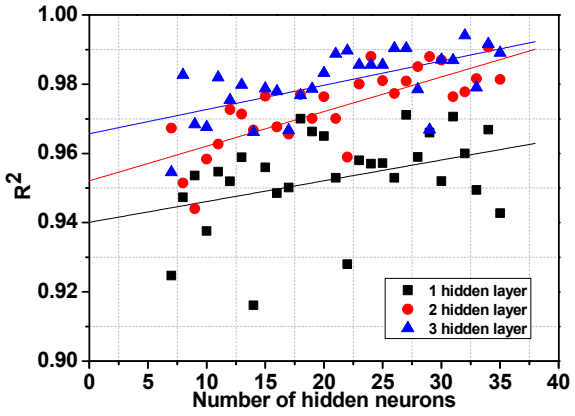

Fig. 4 R_squared of training data as a function of the number of hidden layer

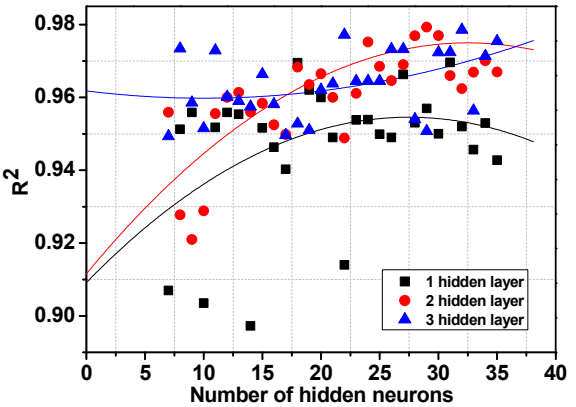

Fig. 5 R_squared of test data as a function of the number of hidden layer

4. Results and Discussion

4.1 Estimation of Wave Transmission Rate Using Empirical Formula

As shown in Fig. 6, we compared the experimental values of wave transmission rate with those obtained from empirical formula. Takayama et al. (1985) suggested an estimated wave transmission rate that has an MSE of 0.021 and an R^2 value of 0.5, which reveals the overestimation of experimental results with a low accuracy (Fig. 6(a)). Some data even broke the pattern of effective wave transmission rate ($0 < K_t < 1$), driven by the case of high relative freeboard. Takayama's formula can mainly use for the submerged structure under still water level, and the empirical formula are composed of the linear regression type of the 1st order of polynomial equation, which cause the low accuracy.

Among four different empirical formulas, Goda and Ahrens (2008) revealed the estimated wave transmission rate that has an MSE of 0.008 and an R^2 value of 0.851, which shows the highest accuracy because suggested formula used 6 types of dimensionless numbers for converted effective crest width (B_{eff}) under various conditions (Fig. 6(b)). Fig. 6(c) shows the estimated wave transmission rate of LCS suggested by Van der Meer et al. (2005). The effective values of wave transmission rate are obtained in the range of $0.075 < K_t < 0.8$ in the empirical formula. They provided an MSE of 0.009 and an R^2 value of 0.81, which generally represent overestimated results compared to experimental results. In the same manner, the results, obtained from Carabrese et al. (2003) provides the overestimated prediction at the point of wave transmission rate compared to the experimental results, as shown in Fig. 6(d), suggesting inappropriate model for our study.

4.2 Prediction Accuracy Analysis Using ANN

Figs. 7 and 8 show the wave transmission rate of the training and test data of 206 sets using a deep neural network under the optimum condition of 29 hidden neurons with 2 hidden layers. In the figures, the horizontal axis reveals the experimental values, and the vertical axis shows the distribution of predicted values. In the prediction results of the training dataset, index of agreement (I) was 0.997, scatter index (SI) was 0.086, and R^2 was 0.988. For the test dataset, MSE was 1.3×10^{-3}, I was 0.995, SI was 0.078, and R^2 was 0.979, suggesting that the predictive model for the wave transmission rate demonstrated excellent performance. Based on the obtained analysis, it is worth noting that the performance prediction method using an artificial neural network model can be suitable for various fields in coastal engineering, unlike the broadly used empirical formula. Table 5 shows the statistical model performance results based on the application of popular empirical formula compared to deep neural network, which suggests that the ANN model provides a more accurate prediction performance compared to the empirical formula. In addition, the ANN model is not required to set up the effective range of the wave transmission rate or apply the special formula dependent on the input variables whereas the empirical formula can be used under the recommended effective range in order to diminish the uncertainty.

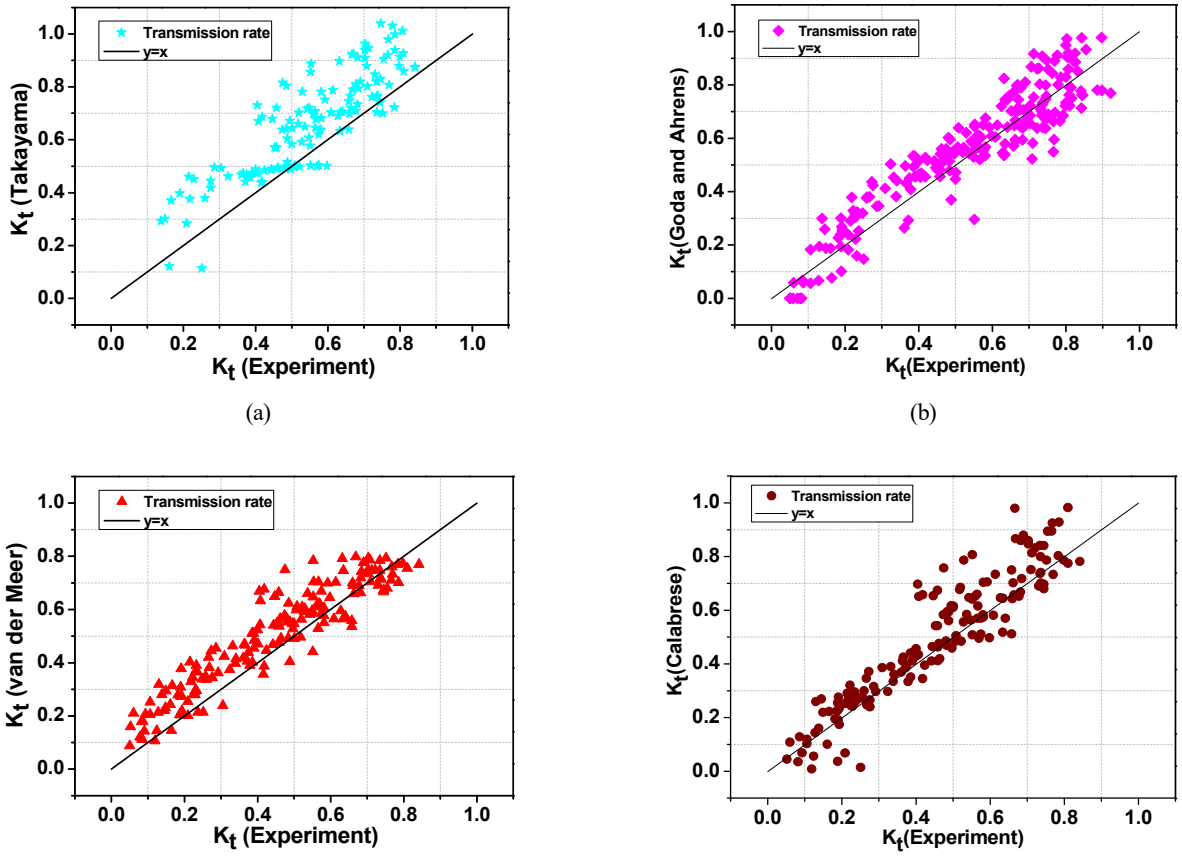

Fig. 6 Comparison of wave transmission formulas with experimental data: (a) Takayama et al. (1985); (b) Goda and Arhens. (2008); (c) Van der Meer et al. (2005); (d) Calabrese et al. (2003)

Table 5 Statistical parameters of the results

Methods	MSE	I	SI	R^2
Takayama et al. (1985)	21×10^{-3}	0.846	0.263	0.500
Goda and Arhens (2008)	8×10^{-3}	0.962	0.172	0.851
Van der Meer (2005)	9×10^{-3}	0.974	0.221	0.810
Calabrese et al. (2003)	9×10^{-3}	0.952	0.215	0.792
ANN model	1.3×10^{-3}	0.995	0.078	0.979

Note: MSE = Mean square error, I = Index of agreement, SI = Scatter index

Thus, the ANN model can provide high prediction accuracy with cost-effective reliability when only seven dimensionless input variables are used.

4.3 Sensitivity Analysis

To estimate the independent importance of the input variable of the model constructed using ANN calculations and to determine the important input variables, we performed a sensitivity analysis of the effect on the prediction of the wave transmission rate through model application using the same training set. Table 6 shows the sensitivity analysis results of the wave transmission rate for each input variable. To estimate the independent importance of the input variable of the model constructed using ANN calculations and to determine the important input variables, we performed sensitivity analysis of the effect on the prediction of the wave transmission rate through model application using the same training set. The analysis reveals that the model accuracy for the relative freeboard (R_C/H_0) had an MSE of 146.7×10^{-3} and an R^2 value of 0.153, which was found to be the most important parameter for the wave attenuation and wave transmission rate of the structure. This finding is attributed to the reduction of transmitted wave height along with strong breaking wave, and an increased reflected wave in front of the structure as the crown depth is reduced. Figs. 9 (a) and (d) are the distributions of the experimental and predicted values, respectively, when factors related to the relative freeboard and ratio of the crest height to the water depth are excluded, which showed that the predicted value using the model overestimated

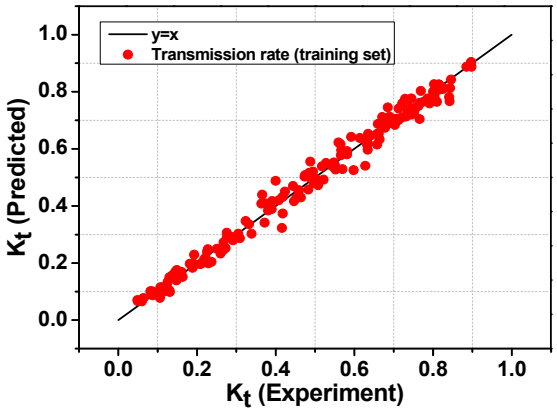

Fig. 7 Comparison of transmission rate between experiment and prediction (training data)

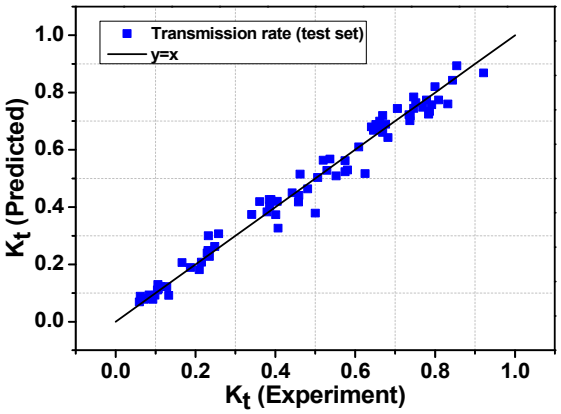

Fig. 8 Comparison of transmission rate between experiment and prediction (test data)

the experimental value and the error increased significantly. As the relative freeboard factor is the dominant factor in wave control, a large error occurred when the two factors were not considered.

Most of empirical formular(van der Meer, 2005; Goda, 2008; Calabrese, 2003; Takayama, 1985) have suggested r elative freeboard (R_C/H_0), ratio of the crest width to wave length (B/L_0) and surf similarity parameter (ξ) as impact factors for wave attenuation coefficient. However, sensitivity to the wave breaking similarity coefficient reflecting the conditions for the front slope and wave slope of the structure was MSE 22.4×10^{-3}, R^2 0.703, which was less sensitive to wave control than other variables. The standard deviation of the input variable is large, and the interpretation of various conditions of the crest width to wave length is insufficient because wave transmission rate was performed for two widths of 0.3 and 1.0, in the input variable. In all experiments and model implementation, the variable control is considered one of the important factors for obtaining reliable results. Therefore, in future research, we plan to develop a model with high predictive performance through the

Table 6 Sensitivity analysis of ANN model

Parameter		Performance measures			
		MSE	I	SI	R^2
X_1	R_C/H_0	146.7×10^{-3}	0.589	0.795	0.153
X_2	B/L_0	9.7×10^{-3}	0.962	0.205	0.864
X_3	ξ	22.4×10^{-3}	0.925	0.311	0.703
X_4	B/L_0	27.0×10^{-3}	0.896	0.341	0.684
X_5	R_C/H	78.3×10^{-3}	0.665	0.581	0.343
X_6	Dn_{50}/h_c	40.1×10^{-3}	0.832	0.416	0.563
X_7	h_c/h	45.4×10^{-3}	0.818	0.443	0.572

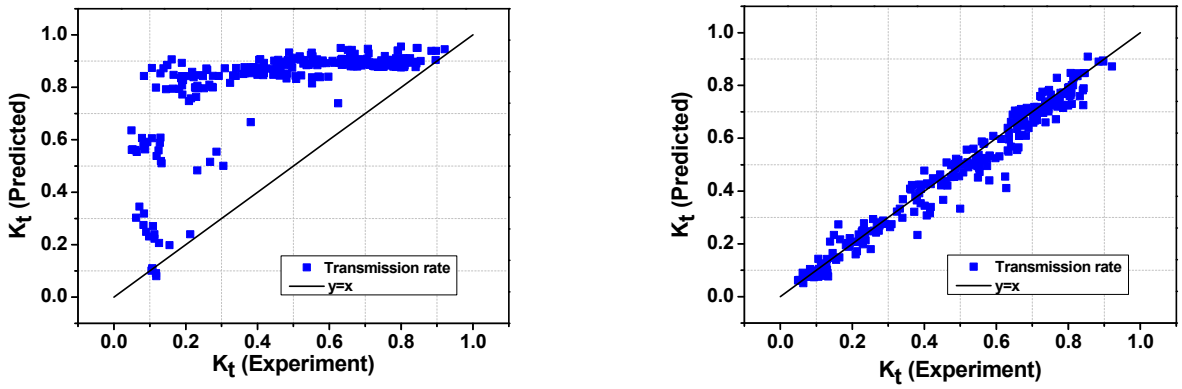

(a) (b)

Fig. 9 Sensitivity analysis of input variables: (a) R_C/H_0 variables of sensitivity; (b) B/H_0 variables of sensitivity; (c) ξ variables of sensitivity; (d) B/L_0 variables of sensitivity; (e) R_C/h variables of sensitivity; (f) Dn_{50}/h_c variables of sensitivity; (g) h_c/h variables of sensitivity

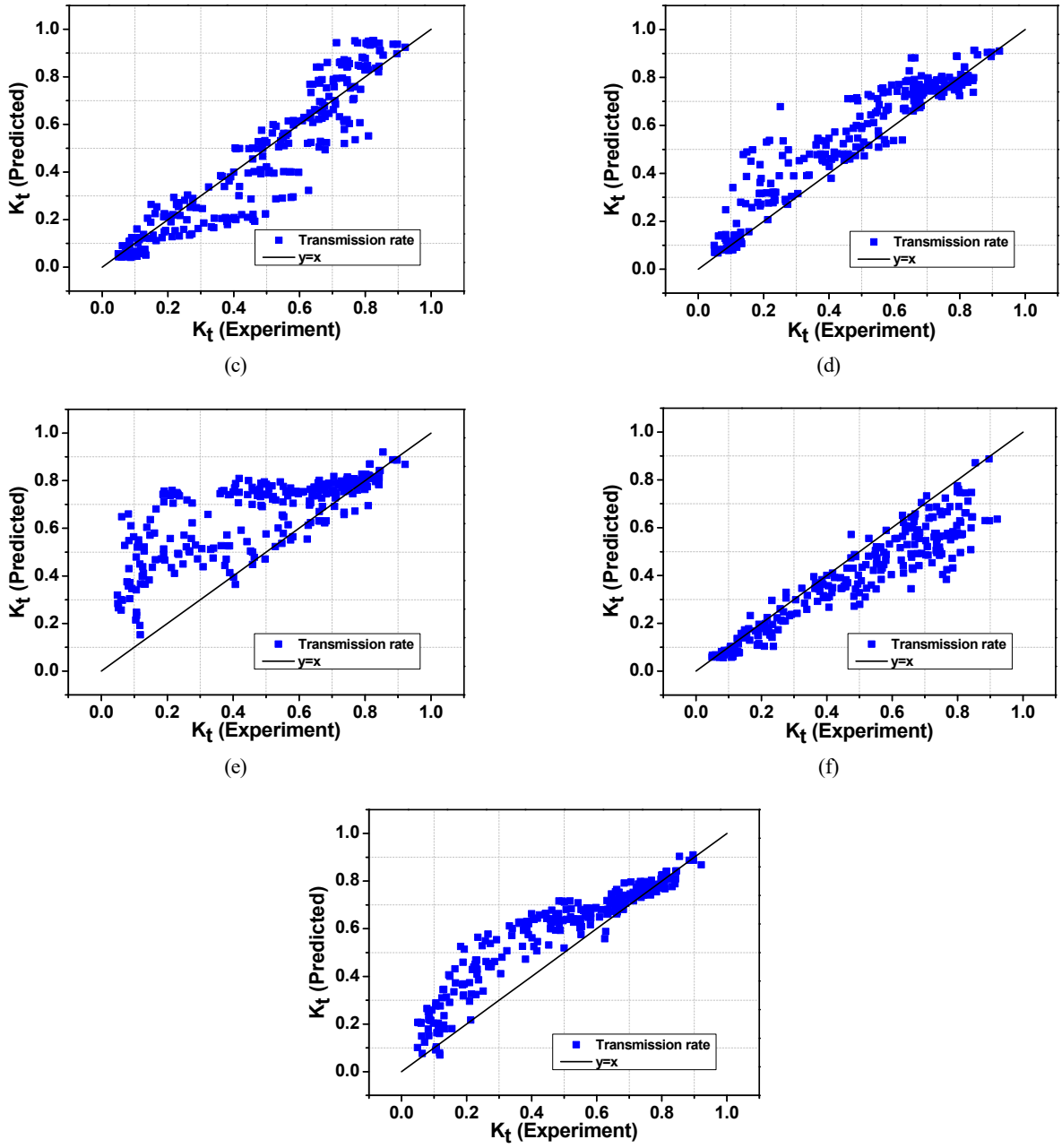

Fig. 9 Sensitivity analysis of input variables: (a) R_C/H_0 variables of sensitivity; (b) B/H_0 variables of sensitivity; (c) ξ variables of sensitivity; (d) B/L_0 variables of sensitivity; (e) R_C/h variables of sensitivity; (f) Dn_{50}/h_c variables of sensitivity; (g) h_c/h variables of sensitivity (Continuation)

development of various machine learning-based predictive models using refined input variables.

4.4 Analysis of Accuracy Metric According to Input Variables Combination

In this study, we applied input variables composed of seven dimensionless numbers ($X = \{X_1 : \frac{R_C}{H_0}, X_2 : \frac{B}{H_0}, X_3 : \xi, X_4 : \frac{B}{L_0}, X_5 : \frac{R_C}{h}, X_6 : \frac{Dn_{50}}{h_c}, X_7 : \frac{h_c}{h}\}$) and analyzed the effect on model performance when some input variables or data were not reflected through various combinations. The results of the predicted values and the experimental values using eight combinations are shown in Fig. 10, and model performance results according to the eight combinations of input variables are shown in Table 7. Combination 1 shows the model performance results when the seven non-dimensional input variables are applied, indicating highest accuracy with an MSE of 1.3×10^{-3} and R^2 of 0.979.

Combination 7, applying three input variables ($X_2 : \frac{B}{H_0}, X_3 : \xi,$

$X_4 : \frac{B}{L_0}$, $X_6 : \frac{Dn_{50}}{h_c}$), showed the lowest accuracy with an MSE of 38.7×10^{-3} and R^2 of 0.401. In addition, combination 8 with same variables applied ($X_1 : \frac{R_C}{H_0}$, $X_5 : \frac{R_C}{h}$, $X_7 : \frac{h_c}{h}$) showed relatively good accuracy, with an MSE of 6.7×10^{-3}, and R^2 of 0.896. The analysis results from various combinations suggest that the accuracy does not increase linearly even if the number of input variables increases.

Furthermore, accurate prediction using neural network model requires reducing training time and improving the simplicity of the model. An ideal model is one that describes the problem in the easiest and simplest way using the fewest variables. Therefore, it is important to identify variables that save modeling time and space.

Accordingly, combination 4 using four input variables produced a result with relatively high accuracy, with an MSE of 2.5×10^{-3} and R^2 of 0.961. In terms of the model time cost, combination 4 offers a good alternative for the model.

Table 7 Performance measures for analysis of different input variable combinations

Combinations	Performance measures						
	MSE	*I*		*SI*		R2	
		test	train	test	train	test	train
1: $X_1, X_2, X_3, X_4, X_5, X_6, X_7$	1.3×10^{-3}	0.995	0.997	0.078	0.086	0.979	0.988
2: $X_2, X_3, X_4, X_5, X_6, X_7$	1.9×10^{-3}	0.992	0.994	0.095	0.080	0.970	0.975
3: X_1, X_4, X_5, X_6, X_7	2.7×10^{-3}	0.989	0.99	0.112	0.100	0.958	0.961
4. X_1, X_2, X_3, X_4, X_6	2.2×10^{-3}	0.991	0.994	0.100	0.077	0.966	0.977
5. X_1, X_4, X_5, X_7	2.5×10^{-3}	0.990	0.994	0.107	0.076	0.961	0.977
6. X_2, X_3, X_4, X_6	37.4×10^{-3}	0.807	0.919	0.414	0.265	0.424	0.632
7. X_2, X_3, X_6	38.7×10^{-3}	0.791	0.902	0.422	0.285	0.401	0.552
8. X_1, X_5, X_7	6.7×10^{-3}	0.973	0.977	0.175	0.150	0.896	0.906

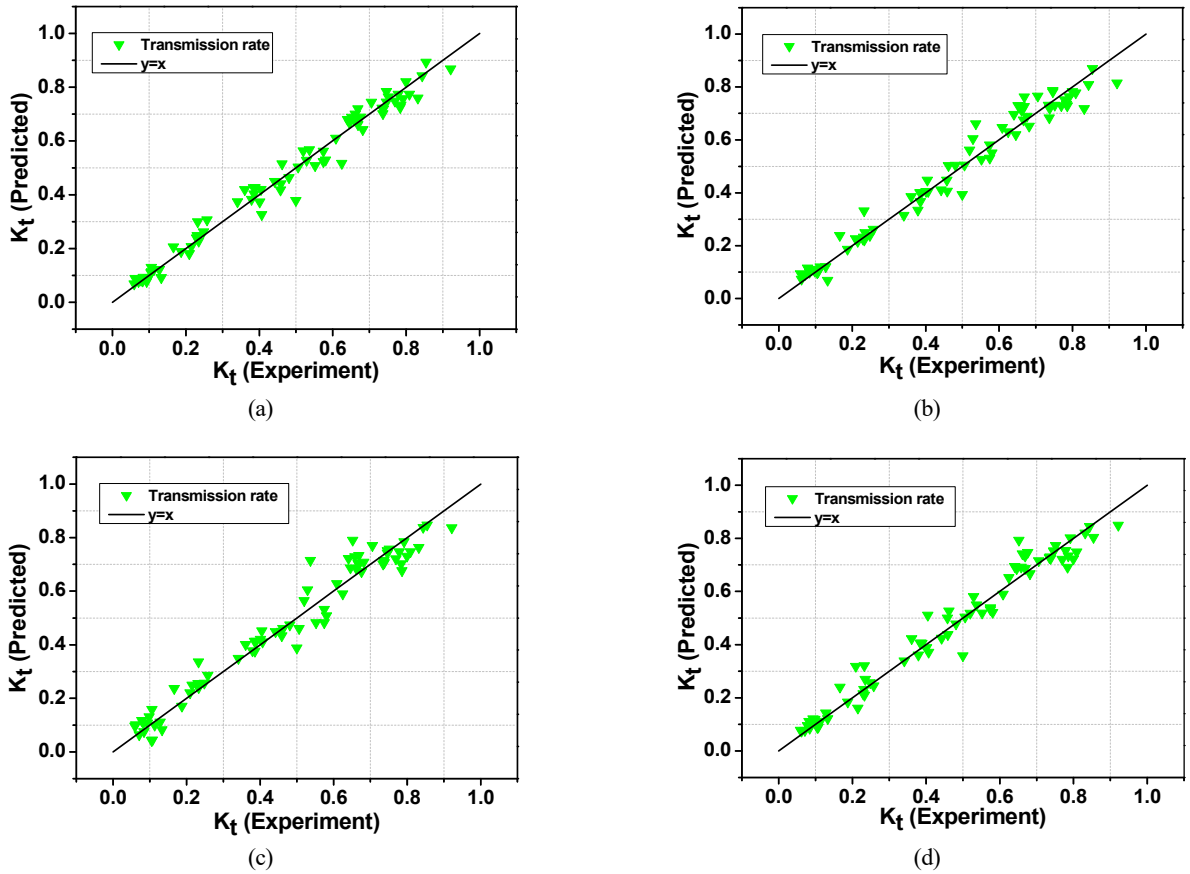

Fig. 10 Influence of number of input; variables: (a) Combination 1; (b) Combination 2; (c) Combination 3; (d) Combination 4; (f) Combination 6; (g) Combination 7; (h) Combination 8

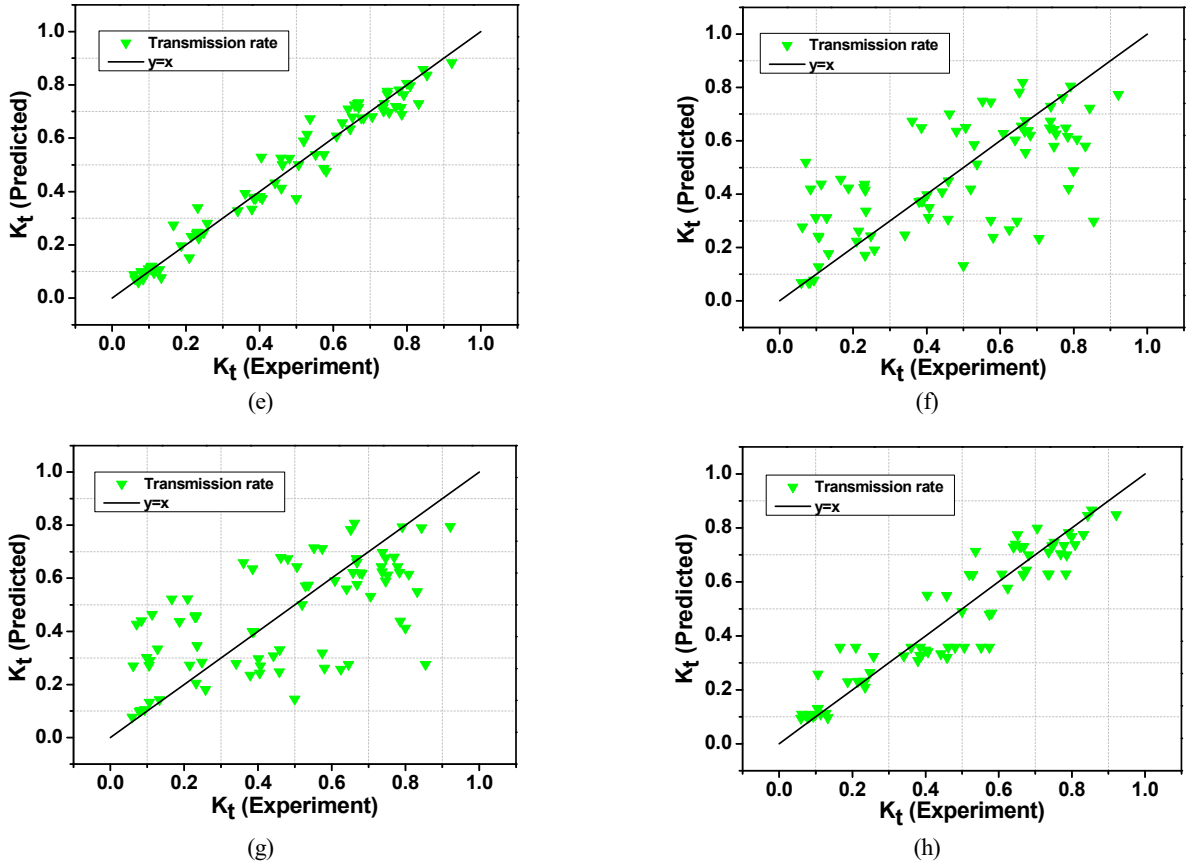

Fig. 10 Influence of number of input; variables: (a) Combination 1; (b) Combination 2; (c) Combination 3; (d) Combination 4; (f) Combination 6; (g) Combination 7; (h) Combination 8 (Continuation)

4. Conclusion

In this study, we built a deep neural network model to predict the wave transmission rate of low crested structures using TensorFLow, an open source platform. To construct the model, we utilized the hydraulic model experiment data from Seelig (1980), Daemrich and kahle (1985), van der Meer (1988), Daemen (1991) for training (70%) and prediction (30%). These neural network models show reliable prediction performance and are expected to be widely used in practical applications in the field of coastal engineering.

The sensitivity analysis using the neural network model found that importance of independent variable input for relative freeboard (R_C/H_0) and ratio of the crest height to the water depth (R_C/h) was large, and the lowest performance appeared when the two factors were excluded from training. In short, the crest depth was found to be the most dominant factor influencing the wave height attenuation in the hydraulic behavior around the low crested structure.

The proposed model showed relatively high accuracy in predicting the wave transmission coefficient of the low crested structure according to various combinations of input variables, with combination 5 showing 0.961 despite using a small number of input variables. In terms of the model time cost, a method using combination 5 offers a good alternative.

The prediction results were analyzed using a comparative review of the results from the existing empirical formula and statistical indicators. The result of wave transmission rate of the trained deep neural network model showed very good prediction accuracy, with 1.3×10^{-3} of MSE, 0.995 of I, 0.078 of SI, and 0.979 of R^2, the prediction performance is highly improved compared to existing empirical results. Engineers and scientists can use the suggested model as a design tool to predict the wave transmission coefficient behind the low crested structure.

Conflict of Interest

Soonchul Kwon serve as an editor of the Journal of Ocean Engineering and Technology but has no role in the decision to publish this article. No potential conflict of interest relevant to this article was reported.

Funding

This work was supported by a 2-Year Research Grand of Pusan National University.

References

Calabrese, M., Vicinanza, D., & Buccino, M. (2003). 2D wave set up

behind low crested and submerged breakwaters. *Proceedings of the 13th International Conference ISOPE, Honolulu, Hawaii, USA.* https://onepetro.org/ISOPEIOPEC/proceedings/ISOPE03/All-ISOPE03/ISOPE-I-03-321/8542

Daemen, I. F. R. (1991). *Wave transmission at low-crested structures* [Master thesis, Delft University of Technology]. Delft Hydraulics Report H462.http://resolver.tudelft.nl/uuid:433dfcf3-eb87-4dc9-88dc-8969996a6e3f

Daemrich, K., & Kahle, W. (1985). Protective effect of underwater breakwaters under the influence of irregular sea waves (Report Heft 61). Franzius-Instituts fur Wasserbau und Kusteningenieurswesen.

Formentin, S. M., Zanuttigh, B., & Van der Meer, J. W. (2017). A Neural network tool for predicting wave reflection, overtopping and transmission. *Coastal Engineering Journal, 59(1)*, 1750006. https://doi.org/10.1142/S0578563417500061

Goda, Y., & Ahrens, J. P., (2008). New formulation of wave transmission over and through low-crested structures. *Proceedings of the 31st International Conference of Coastal Engineering, Hamburg, Germany,* 3530−3541. https://doi.org/10.1142/9789814277426_0292

Hashemi, M. R., Ghadampour, Z., & Neill, S. P. (2010). Using an artifi cial neural network to model seasonal changes in beach profiles. *Ocean Engineering, 37*(14-15), 1345−1356. https://doi.org/10.1016/j.oceaneng.2010.07.004

Kim, D. H., & Park, W. S. (2005). Neural network for design and reliability analysis of rubble mound breakwaters. *Ocean engineering, 32*(11-12), 1332−1349. https://doi.org/10.1016/j.oceaneng.2004.11.008

Koosheh, A., Etemad-Shahid, A., Cartwright, N., Tomlinson, R., & Hosseinzadeh, S. (2020). The comparison of empirical formulae for the prediction of mean wave overtopping rate at aromored sloped structures. *Coastal Structure, 36v.* https://icce-ojs-tamu.tdl.org/icce/index.php/icce/article/view/10161

Lee, J. H., Jung, W. J., Bae, J. H., Lee, K. H., & Kim, D. S. (2019). Variation characteristic of wave field around 2-dimensional low-crested-breakwaters. *Journal of Korean Society of Coastal and Ocean Engineers, 31*(5), 294−304. https://doi.org/10.9765/KSCOE.2019.31.5.294

Lee, J. I., & Bae, I. L. (2020). Experimental study for wave transmission coefficients of submerged structure : Ⅰ. Permeable type structure. *Journal of the Korean Society of Civil Engineers, 40*(5), 485−496. https://doi.org/10.12652/Ksce.2020.40.5.0485

Panizzo, A., & Briganti, R. (2007). Analysis of wave transmission behind low-crested breakwaters using neural networks. *Coastal Engineering, 54*(9), 643−656. https://doi.org/10.1016/j.coastaleng.2007.01.001

Rigos, A., Tsekouras, G. E., Chatzipavlis, A., & Velegrakis, A. F. (2016). Modeling beach rotation using a novel legendre polynomial feedforward neural network trained by nonlinear constrained optimization. In *IFIP International Conference on Artificial Intelligence Applications and Innovations* (pp. 167−179). Springer International Publishing.

Seelig, W. N. (1980). *Two dimensional tests of wave transmission and feflection characteristics of laboratory breakwaters* (Technical report No. 80-1). Coastal Engineering Research Center, U.S. Army, Corps of Engineers Waterways Experiment Station, Vicksburg, MS, 187. https://apps.dtic.mil/sti/pdfs/ADA089603.pdf

Shamshirband, S., Mosavi, A., Rabczuk, T., Nabipour, N., & Chau, K. W. (2020). Prediction of significant wave height; comparison between nested grid numerical model, and machine learning models of artificial neural networks, extreme learning and support vector machines. *Engineering Applications of Computational Fluid Mechanics, 14*(1), 805−817. https://doi.org/10.1080/19942060.2020.1773932

Takayama, T., Nagai, K., & Sekiguchi, T. (1985). Irregular wave experiments on wave dissipation function of submerged breakwater with wide crown. In *Proceedings of 32th Japanese Conference on Coastal Engineering, JSCE,* (Vol. 32, pp. 545−549)

Van der Meer, J. W. (1988). *Rock slopes and gravel beaches under wave attack* [PhD thesis, Delft University of Technology]. Delft Hydraulics Report 396.

Van der Meer, J. W., Briganti, R., Zanuttigh, B., & Wang, B. (2005). Wave transmission and reflection at low-crested structures: Design formulae, oblique wave attack and spectral change. *Coastal Engineering, 52*(10−11), 915−929. https://doi.org/10.1016/j.coastaleng.2005.09.005

Author ORCIDs

Author name	ORCID
Kim, Taeyoon	0000-0002-5060-5302
Lee, Woo-Dong	0000-0001-7776-4664
Kwon, Yongju	0000-0001-7935-8416
Kim, Jongyeong	0000-0001-6642-8622
Kang, Byeonggug	0000-0003-4057-4386
Kwon, Soonchul	0000-0003-3764-331X

KSOE

Journal of Ocean Engineering and Technology 36(5), 326-339, October, 2022
https://doi.org/10.26748/KSOE.2022.028

pISSN 1225-0767
eISSN 2287-6715

Original Research Article

Analysis of Hydraulic Characteristics According to the Cross-Section Changes in Submerged Rigid Vegetation

Jeongheum Lee[1], Yeon-Myeong Jeong[2], Jun-Seok Kim[1], and Dong-Soo Hur[3]

[1]*Graduate Student, Department of Ocean Civil Engineering, Gyeongsang national University, Tongyeong, Korea*
[2]*Senior Researcher, Engineering Research Institute, Gyeongsang national University, Jinju, Korea*
[3]*Professor, Department of Ocean Civil Engineering, Gyeongsang national University, Tongyeong, Korea*

KEY WORDS: Submerged vegetation, Rigid vegetation, Laboratory experiment, Numerical wave tank, Hydraulic characteristics

ABSTRACT: *Recently, not only Korea but also the world has been suffering from problems related to coastal erosion. The hard defense method has been primarily used as a countermeasure against erosion. However, this method is expensive and has environmental implications. Hence, interest in other alternative methods, such as the eco-friendly vegetation method, is increasing. In this study, we aim to analyze the hydraulic characteristic of submerged rigid vegetation according to the cross-sectional change through a hydraulic experiment and numerical simulation. From the hydraulic experiment, the reflection coefficient, transmission coefficient, and energy dissipation coefficient were analyzed according to the density, width, and multi-row arrangement of the vegetation zone. From numerical simulations, the flow field, vorticity distribution, turbulence distribution, and wave distribution around the vegetation zone were analyzed according to the crest depth, width, density, and multi-row arrangement distance of the vegetation zone. The hydraulic experiment results suggest that the transmission coefficient decreased as the density and width of the vegetation zone increased, and the multi-row arrangement condition did not affect the hydraulic characteristics significantly. Moreover, the numerical simulations showed that as the crest depth decreased, the width and density of vegetation increased along with vorticity and turbulence intensity, resulting in increased wave height attenuation performance. Additionally, there was no significant difference in vorticity, turbulence intensity, and wave height attenuation performance based on the multi-row arrangement distance. Overall, in the case of submerged rigid vegetation, the wave energy attenuation performance increased as the density and width of the vegetation zone increased and crest depth decreased. However, the multi-row arrangement condition did not affect the wave energy attenuation performance significantly.*

1. Introduction

Recently, coastal erosion has become a major issue globally. Coastal erosion occurs owing to the rise in sea levels caused by global warming, invasion of high waves caused by abnormal temperatures, reduced soil supply caused by river development (e.g., dams), and change in the coastal environment caused by coastal development (e.g., port construction). When sand is lost owing to coastal erosion, the national land area decreases, thereby damaging those regions socially and economically . Countermeasures against coastal erosion include construction of gravity-based structures, such as groins and detached breakwaters, and beach nourishment. However, gravity-based structures are expensive and not eco-friendly, and beach nourishment is not a fundamental solution. Therefore, many studies have been conducted on countermeasures, and interest in the eco-friendly vegetation method has been increasing. While studies on vegetation have been conducted in the United States and Europe, such studies are not active in Korea.

Vegetation has different characteristics depending on various conditions, such as the shape of the material used, height of vegetation, and density and width of the vegetation zone, and many related studies were conducted on this topic (Anderso et al., 2011; Manca et al., 2010; Asano et al., 1988; Abdolahpour et al., 2017; Beudin et al., 2017; Hadadpour et al., 2019). Peruzzo et al. (2018) collected actual vegetation from nature and produced flexible vegetation with a similar shape. They performed a hydraulic model experiment and calculated the vegetation drag coefficient according to the density and depth of the vegetation zone. Wang et al. (2022) studied the wave transmission coefficient and drag coefficient of cylindrical flexible vegetation according to the depth and density through a hydraulic model experiment. Furthermore, various hydraulic model experiments on flexible vegetation have been performed (Blackmar et al., 2014; Maza

Received 10 August 2022, revised 26 August 2022, accepted 28 August 2022
Corresponding author Dong-Soo Hur: +82-55-772-9122, dshur@gnu.ac.kr

et al., 2015). Additionally, Hu et al. (2014) studied wave height attenuation and the drag coefficient of vegetation according to the density and depth of the vegetation zone under the application of waves and flow for rigid cylindrical vegetation through a hydraulic model experiment. Van Veelen et al. (2020) performed a hydraulic model experiment on the effect of changes in the vegetation material on wave height attenuation and flow velocity using flexible and rigid vegetation with the same shape and size and different materials. Jeong and Hur (2016) developed a bidirectional coupled analysis technique by combining the discrete element method with the wave field model and numerically examined the wave attenuation effect according to the behavioral characteristics of vegetation.

As for submerged breakwaters, many studies have been conducted on the wave energy reduction effect by Bragg reflection that occurs when submerged breakwaters are arranged in multiple rows (Kirby and Anton, 1990; Cho et al., 2002; Cho, 2006). However, in the case of vegetation, studies on multi-row arrangement are insufficient.

In this study, a hydraulic model experiment and numerical model experiment were performed to analyze hydraulic characteristics according to the cross-section changes in submerged rigid vegetation. From the hydraulic model experiment, the hydraulic characteristics were analyzed according to the density and width of the vegetation zone and the cross-section change in multi-row arrangement. From the numerical model experiment, the flow field, vorticity distribution, turbulence distribution, and wave height distribution were analyzed according to the crest depth, density, width, and multi-row arrangement distance of the vegetation zone.

2. Hydraulic Model Experiment

2.1 Overview of the Hydraulic Model Experiment

The hydraulic model experiment was performed to analyze hydraulic characteristics according to the cross-section variation in submerged rigid vegetation. A wave flume with a length of 37 m, height of 1 m, and width of 0.6 m was used in the experiment. A piston-type wave generator was used in the experiment. A 30 cm-high impermeable floor with a front inclination of 1:30 was constructed to generate waves, and a capacitance wave gauge was used to measure the wave height.

Fig. 1 and Table 1 show the configuration of the wave flume and the cross-section conditions of the vegetation. The density, width, and multi-row arrangement of the vegetation zone were considered for the cross-section conditions. The rigid vegetation used in the experiment was made of an acrylic material, as shown in Fig. 2(a). Fig. 3 shows

Table 1 Vegetation cross section condition

Case	V_h (cm)	R (cm)	B (cm)	V_d (cm)	ρ_V	Number of vegetation
R1	14.8	2.2	133	-	0.123	972
R2	14.8	2.2	133	-	0.032	255
R3	14.8	2.2	266	-	0.123	1944
R4	14.8	2.2	133	133	0.123	1944

Note: V_h = vegetation height, R = vegetation zone crest depth, B = vegetation zone width, V_d = distance of each vegetation zone, ρ_V = vegetation zone density

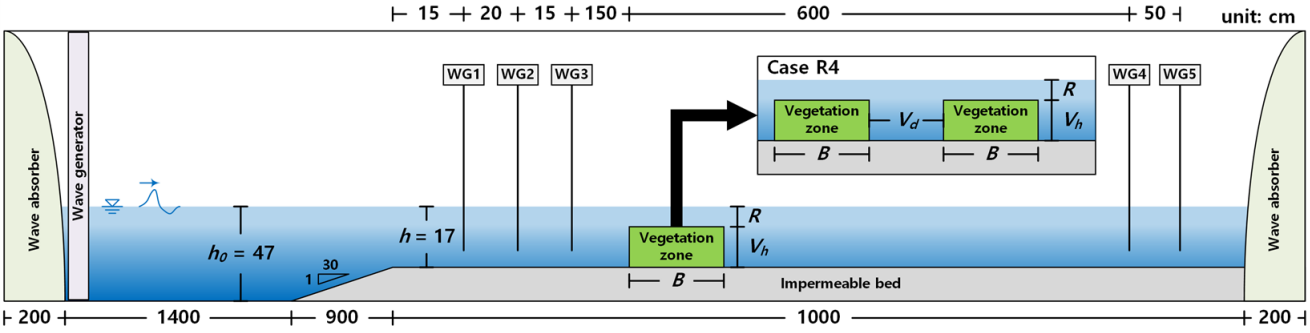

Fig. 1 Sketch of wave flume and experimental setup

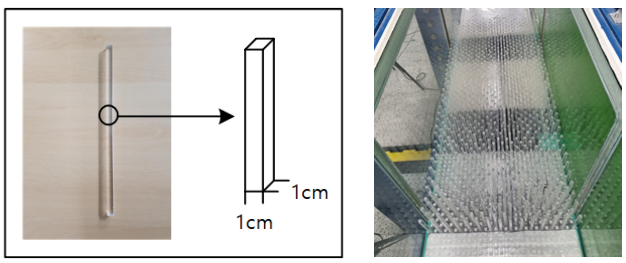

(a) (b)

Fig. 2 Vegetation used in the experiment: (a) specification of vegetation; (b) vegetation zone installed in the wave flume

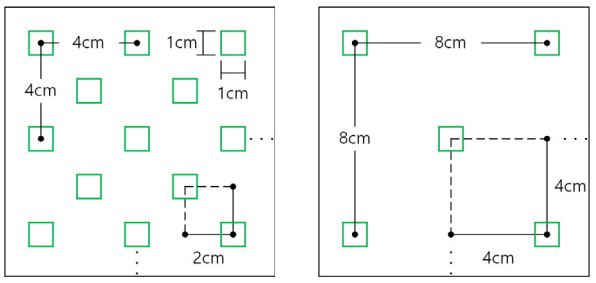

(a) (b)

Fig. 3 Sketch of frame fixed vegetation: (a) ρ_V = 0.123; (b) ρ_V = 0.032

the frame fixed vegetation. Figs. 3(a) and 3(b) represent cases in which the vegetation densities (ρ_V) are 0.123 and 0.032, respectively.

$$S(f) = 0.257 H_S^2 T_S^{-4} f^{-5} \exp[-1.03(T_S f)^{-4}] \quad (1)$$

where $S(f)$ is the wave spectral density, H_S is the significant wave height, T_S is the significant wave period, and f is the frequency.

Table 2 shows the incident wave conditions. The incident waves were irregular waves with a wave height of 2.67–11.0 cm and a period of 0.64–1.88 s. The Bretschneider–Mitsuyasu spectrum of Eq. (1) proposed by Mitsuyasu (1969) was used to generate the irregular waves. In Fig. 4, the theoretical values of the Bretschneider–Mitsuyasu spectrum are compared with those obtained from the experiment. Figs. 4(a) and 4(b) represent wave case 4 (H_S = 5.33 cm, T_S = 0.95 s) and wave case 16 (H_S = 11.0 cm, T_S = 1.88 s), respectively.

Table 2 Incident wave condition (wave type = irregular, h = 17 cm)

Wave case	H_S (cm)	T_S (s)	L_S (cm)
1	2.67	0.64	60.3
2	5.33	0.64	60.3
3	2.67	0.95	107.1
4	5.33	0.95	107.1
5	2.67	1.26	150.9
6	5.33	1.26	150.9
7	9.00	1.26	150.9
8	11.00	1.26	150.9
9	2.67	1.57	193.3
10	5.33	1.57	193.3
11	9.00	1.57	193.3
12	11.00	1.57	193.3
13	2.67	1.88	234.9
14	5.33	1.88	234.9
15	9.00	1.88	234.9
16	11.00	1.88	234.9

Note: H_S = significant wave height, T_S = significant wave period, L_S = significant wave length

The reflection coefficient (K_R), transmission coefficient (K_T), and energy dissipation coefficient (K_D) were calculated to analyze hydraulic characteristics according to the cross-section changes in submerged rigid vegetation. The reflection coefficient (K_R) was calculated using the incident/reflected wave separation method proposed by Goda and Suzuki (1976). The transmission coefficient (K_T) and energy dissipation coefficient (K_D) were calculated using Eqs. (2) and (3), respectively.

$$K_T = \frac{H_T}{H_O} \quad (2)$$

where H_O is the incident wave height and H_T is the transmitted wave height.

$$K_D = \sqrt{1 - K_R^2 - K_T^2} \quad (3)$$

2.2 Results of the Hydraulic Model Experiment

A fixed-bed hydraulic model experiment was performed as a preliminary experiment to examine the hydraulic characteristics of wave propagation according to the cross-section changes in submerged rigid vegetation. In other words, K_R, K_T, and K_D were calculated according to the density, width, and multi-row arrangement conditions of submerged rigid vegetation. Fig. 5 shows the distribution of the coefficients according to the wave steepness. Figs. 5(a), 5(b), and 5(c) represent the cases of K_R, K_T, and K_D, respectively.

2.2.1 Reflection coefficient

The reflection coefficient was not significantly different depending on the width and multi-row arrangement for Case R1 (B = 133 cm, ρ_V = 0.123), Case R3 (B = 266 cm, ρ_V = 0.123), and Case R4 (B = 133,

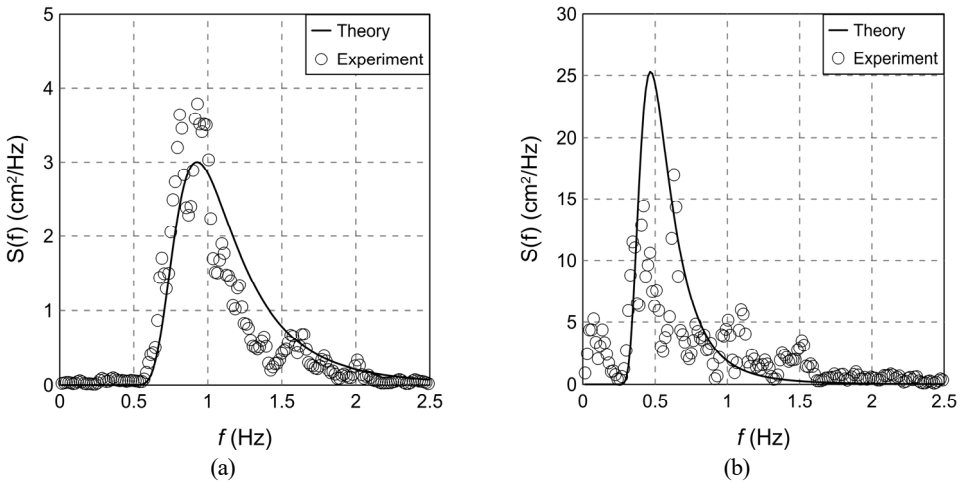

Fig. 4 Comparison between theoretical and experimental spectra: (a) wave case 4; (b) wave case 16

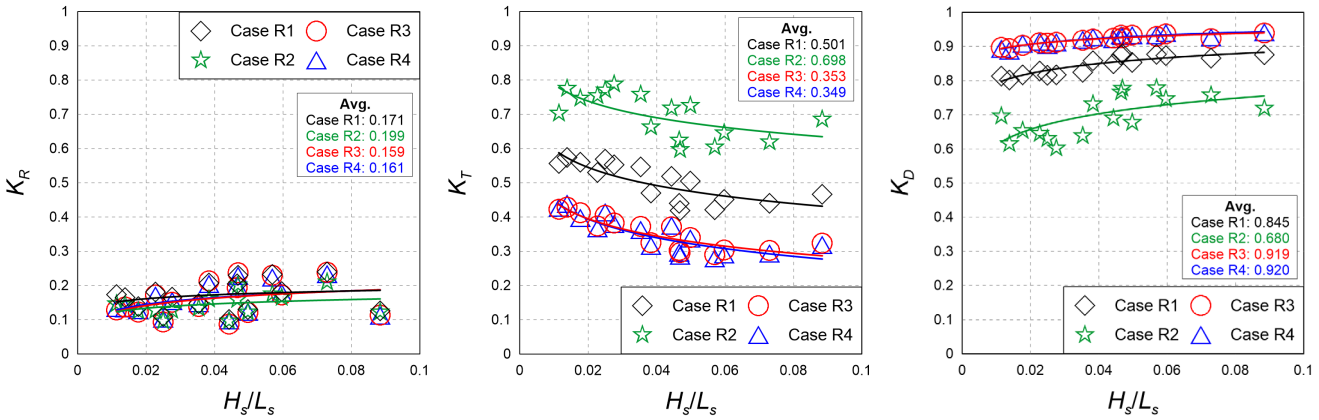

Fig. 5 Comparison of K_R, K_T, and K_D according to changes in the cross-section condition of the rigid vegetation zone

133 cm, $\rho_V = 0.123$), which had the same density. It decreased slightly for Case R2 ($B = 133$ cm, $\rho_V = 0.032$), which had lower density. This is because the reflected wave was generated similarly when the density of the vegetation zone was the same and the transmission area of waves increased as the vegetation density decreased.

2.2.2 Transmission coefficient

The transmission coefficient was found to decrease in Case R3 ($B = 266$ cm, $\rho_V = 0.123$) and Case R4 ($B = 133$, 133 cm, $\rho_V = 0.123$), where the density was the same and the width of the vegetation zone increased compared to that in Case R1 ($B = 133$ cm, $\rho_V = 0.123$), and in Case R2 ($B = 133$ cm, $\rho_V = 0.032$), where the width was identical and the density decreased. This is because an increase in the density and width of the vegetation zone induces more breaking waves at the crest of the vegetation zone.

2.2.3 Energy dissipation coefficient

The energy dissipation coefficient was the lowest in Case R2 ($B = 133$ cm, $\rho_V = 0.032$), where the width and density of the vegetation zone were low, and showed a tendency to increase as the width and density of the vegetation zone increased. Additionally, there was no significant difference in hydraulic characteristics between Case R3 ($B = 266$ cm, $\rho_V = 0.032$) and Case R4 ($B = 133$, 133 cm, $\rho_V = 0.032$), which had the same density and width of the vegetation zone. In the case of submerged rigid vegetation, it was assumed that the multi-row arrangement condition does not affect the wave energy attenuation of the incident wave significantly.

3. Overview of the Numerical Model Experiment

The numerical model experiment was performed to analyze hydraulic characteristics according to the cross-section changes in the submerged rigid vegetation. As for the numerical model, LES-WASS-2D (Hur and Choi, 2008), a complete nonlinear two-dimensional (2D) model that can consider the energy dissipation by fluid resistance according to the characteristics of the permeable medium based on the porous body model and volume of fluid capable of considering the effect of permeability, was used.

3.1 Governing Equations

The basic equations of the numerical model consist of the continuity equation, modified Navier–Stokes equations, and advection equation, which are shown in Eq. (4), Eqs. (5)–(6), and Eq. (7), respectively.

$$\frac{\partial(\gamma_x u)}{\partial x}+\frac{\partial(\gamma_z w)}{\partial z}=q^* \tag{4}$$

$$\begin{aligned}\gamma_v\frac{\partial u}{\partial t}+u\frac{\partial(\gamma_x u)}{\partial x}+w\frac{\partial(\gamma_z u)}{\partial z}\\ =-\gamma_v\frac{1}{\rho}\frac{\partial p}{\partial x}+\frac{1}{\rho}\left[\frac{\partial}{\partial x}\left\{\gamma_x\nu_t\left(2\frac{\partial u}{\partial x}\right)\right\}+\frac{\partial}{\partial z}\left\{\gamma_z\nu_t\left(\frac{\partial u}{\partial z}+\frac{\partial w}{\partial x}\right)\right\}\right]\\ -M_x-E_x-D_x\end{aligned} \tag{5}$$

$$\begin{aligned}\gamma_v\frac{\partial w}{\partial t}+u\frac{\partial(\gamma_x w)}{\partial x}+w\frac{\partial(\gamma_z w)}{\partial z}\\ =-\gamma_z\frac{1}{\rho}\frac{\partial p}{\partial z}+\frac{1}{\rho}\left[\frac{\partial}{\partial x}\left\{\gamma_x\nu_t\left(\frac{\partial w}{\partial x}+\frac{\partial w}{\partial z}\right)\right\}+\frac{\partial}{\partial z}\left\{\gamma_z\nu_t\left(2\frac{\partial w}{\partial z}\right)\right\}\right]\\ -\frac{2\nu}{3}\frac{\partial q^*}{\partial z}-\gamma_v g-\beta w-M_z-E_z-D_z\end{aligned} \tag{6}$$

$$\frac{\partial(\gamma_v F)}{\partial t}+\frac{\partial(\gamma_x F u)}{\partial x}+\frac{\partial(\gamma_z F w)}{\partial z}=Fq^* \tag{7}$$

where u and w are the flow velocities in the x and z directions, respectively. q^* is the flow density of the wave source. M_x and M_z are inertial resistance. E_x and E_z are laminar flow resistance. D_x and D_z are turbulence resistance. γ_v is the volumetric porosity. γ_x and γ_z are the area permeabilities along the x and z directions, respectively. t is the time, g is the gravitational acceleration, ρ is the fluid density, p is the pressure, β is the wave attenuation coefficient, F is the volume ratio occupied by the fluid in each grid, and ν_t is the sum of the kinematic viscosity coefficient and kinematic eddy viscosity.

3.2 Vegetation Drag

The fluid resistance by vegetation (RV_i) is given by Eq. (8).

$$RV_i = \frac{1}{2} C_D \Phi v_i \sqrt{v_i^2 + v_j^2} + C_M (1-\gamma_v) \frac{\partial v_i}{\partial t} \quad (8)$$

where Φ is the vegetation density, C_D is the drag coefficient, and C_M is the inertial resistance.

For C_D, Eq. (9), which was presented by Lee et al. (2017a) by analyzing the experimental results of Wu and Cox (2015), was applied. C_M = 1.5, as proposed by Sakakiyama and Kajima (1992), was applied.

$$C_D = 1.4\left(1 + \frac{15}{KC}\right) \quad (9)$$

where KC is the Keulegan–Carpenter number.

3.3 Verification of the Numerical Wave Tank

To examine the validity of the numerical model, a 2D numerical wave tank was constructed, as shown in Fig. 6. The lengths of the x and z axes were set to be 1000 and 30 cm, respectively. The grid sizes of △x and △z were set to be 1 cm. Additional dissipation zones were prepared at both ends of the tank to prevent the reflection and re-reflection of waves.

Table 3 Conditions of incident waves and vegetation cross-section used in this study

Case	Wave conditions		Vegetation zone		
	H_S (cm)	T_S (s)	R (cm)	B (cm)	ρ_V
R1-01	2.67	0.64	2.2	133	0.123
R1-02	5.33	0.64	2.2	133	0.123
R1-03	2.67	0.95	2.2	133	0.123
R1-04	5.33	0.95	2.2	133	0.123
R1-05	2.67	1.26	2.2	133	0.123
R1-06	5.33	1.26	2.2	133	0.123
R1-07	9.00	1.26	2.2	133	0.123
R1-08	11.00	1.26	2.2	133	0.123
R1-09	2.67	1.57	2.2	133	0.123
R1-10	5.33	1.57	2.2	133	0.123
R1-11	9.00	1.57	2.2	133	0.123
R1-12	11.00	1.57	2.2	133	0.123
R1-13	2.67	1.88	2.2	133	0.123
R1-14	5.33	1.88	2.2	133	0.123
R1-15	9.00	1.88	2.2	133	0.123
R1-16	11.00	1.88	2.2	133	0.123
R2-06	5.33	1.26	2.2	133	0.032
R3-06	5.33	1.26	2.2	266	0.123
R4-06	5.33	1.26	2.2	133, 133	0.123

Note: H_S = significant wave height, T_S = significant wave period, R = vegetation zone crest depth, B = vegetation zone width, ρ_V = vegetation zone density

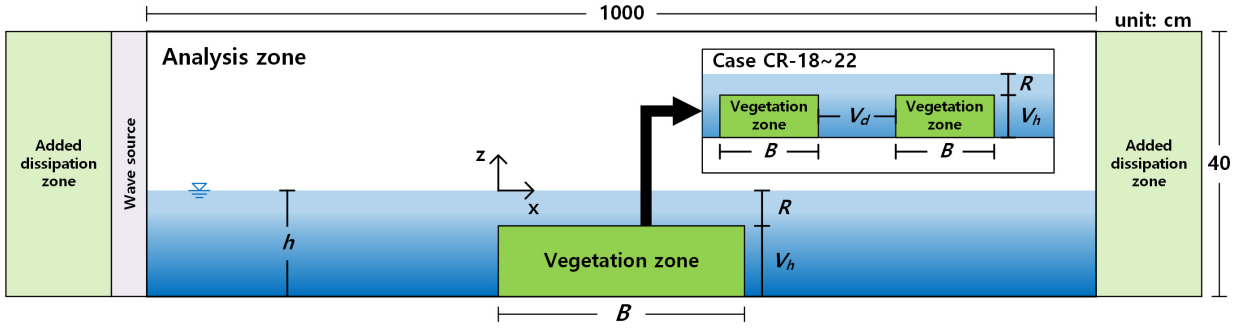

Fig. 6 Sketch of the numerical wave tank based on the hydraulic experiment

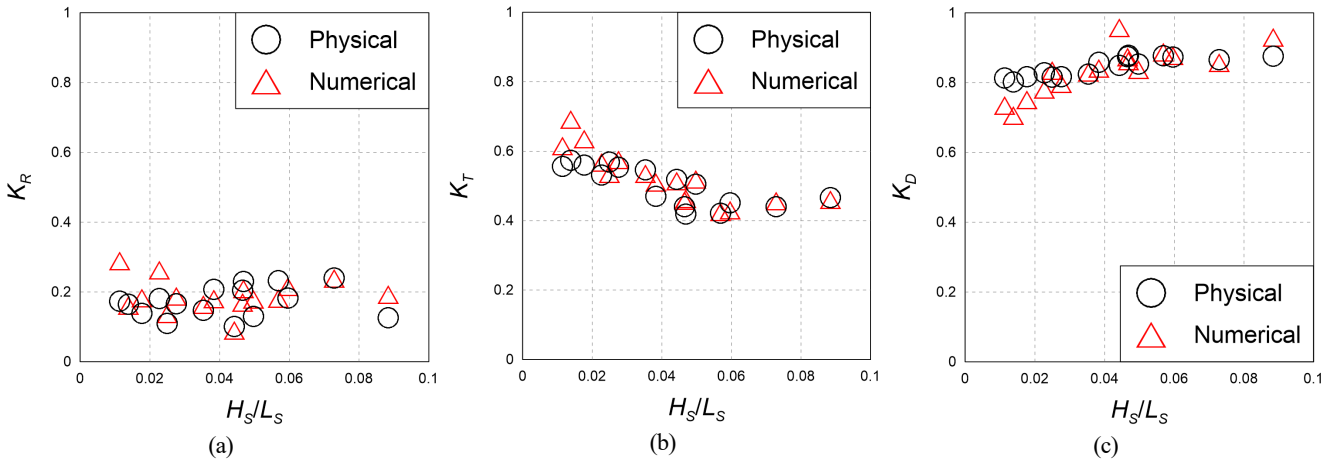

Fig. 7 Comparison of reflection, transmission, and energy dissipation coefficients between the experimental and calculated values

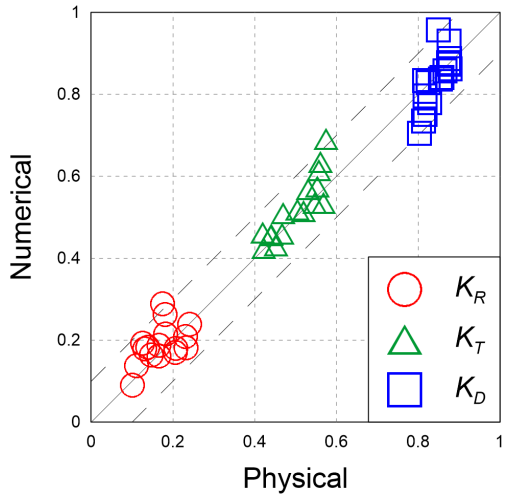

Fig. 8 Comparison of K_R, K_T, and K_D between the experimented and calculated values

The numerical wave tank was compared and verified for the experimental conditions shown in Table 3 for the wave and vegetation cross-section conditions applied in the hydraulic model experiment. As the planar arrangement of rigid vegetation could not be reproduced owing to the characteristics of the 2D numerical model, the vegetation density was replaced with porosity in the numerical model.

In Fig. 7, the results of the hydraulic and numerical model experiments are compared. Figs. 7(a), 7(b), and 7(c) represent the reflection coefficient, transmission coefficient, and energy dissipation coefficient, respectively. For the reflection and transmission coefficients, the calculation results tended to be slightly higher than the experimental values when the wave steepness was low (near H_S/L_S = 0.02). Overall, it was assumed that the calculated values reproduced the experimental values properly. In Fig. 8, the dotted lines show the ±10% range of the values of the hydraulic and numerical model experiments. Overall, it can be seen that the results of the numerical model experiment reproduced the reflection coefficient, transmission coefficient, and energy dissipation coefficient of the hydraulic model experiment appropriately.

4. Results of the Numerical Model Experiment

For a closer analysis of the hydraulic characteristics according to the cross-section changes in submerged rigid vegetation, which were examined in the numerical model experiment, the flow field, vorticity distribution, turbulence distribution, and wave height distribution around the submerged rigid vegetation were examined using the validated numerical wave tank. As shown in Fig. 6 and Table 4, additional experimental conditions compared to the hydraulic model experiment were applied to the numerical wave tank. A regular wave was used as the incident wave to facilitate the analysis. Additionally, the crest depth (R), width (B), density (ρ_V), and arrangement distance (V_d) were considered for the cross-section conditions of the vegetation zone.

Table 4 Experimental conditions used in this study (wave conditions: H_i = 5.33 cm, T_i = 1.26 s)

Case	Vegetation zone						
	R (cm)	R/H_i	B (cm)	B/L_i	ρ_V	V_d (cm)	V_d/L_i
CR-00	2.2	0.413	133	0.887	0.123	-	-
CR-01	0.0	0.000	133	0.887	0.123	-	-
CR-02	1.0	0.188	133	0.887	0.123	-	-
CR-03	3.0	0.563	133	0.887	0.123	-	-
CR-04	4.0	0.750	133	0.887	0.123	-	-
CR-05	5.0	0.938	133	0.887	0.123	-	-
CR-06	2.2	0.413	67	0.447	0.123	-	-
CR-07	2.2	0.413	100	0.667	0.123	-	-
CR-08	2.2	0.413	166	1.107	0.123	-	-
CR-09	2.2	0.413	200	1.333	0.123	-	-
CR-10	2.2	0.413	233	1.553	0.123	-	-
CR-11	2.2	0.413	266	1.773	0.123	-	-
CR-12	2.2	0.413	333	2.220	0.123	-	-
CR-13	2.2	0.413	400	2.667	0.123	-	-
CR-14	2.2	0.413	133	0.887	0.093	-	-
CR-15	2.2	0.413	133	0.887	0.153	-	-
CR-16	2.2	0.413	133	0.887	0.183	-	-
CR-17	2.2	0.413	133	0.887	0.213	-	-
CR-18	2.2	0.413	133	0.887	0.123	44	0.293
CR-19	2.2	0.413	133	0.887	0.123	89	0.593
CR-20	2.2	0.413	133	0.887	0.123	133	0.887
CR-21	2.2	0.413	133	0.887	0.123	177	1.180
CR-22	2.2	0.413	133	0.887	0.123	222	1.480

Note: R = vegetation zone crest depth, H_i = incident wave height, B = vegetation zone width, L_i = incident wave length, ρ_V = vegetation zone density, V_d = distance of each vegetation zone

The vorticity was calculated using Eqs. (10)–(14), which were proposed by Raffel et al. (1998) and Raffel et al. (2007) as in Lee et al. (2017b). Positive (+) values in red represent the counterclockwise direction and negative (−) values in blue represent the clockwise direction.

$$\omega_{xz} = \frac{(\Omega_A + \Omega_B - \Omega_C - \Omega_D)}{4\triangle x \triangle z} \tag{10}$$

$$\Omega_A = \frac{1}{2}\triangle x(u_{i-1,k-1} + 2u_{i,k-1} + u_{i+1,k-1}) \tag{11}$$

$$\Omega_B = \frac{1}{2}\triangle z(w_{i+1,k-1} + 2w_{i+1,k} + w_{i+1,k+1}) \tag{12}$$

$$\Omega_C = \frac{1}{2}\triangle x(u_{i+1,k+1} + 2u_{i,k+1} + u_{i-1,k+1}) \tag{13}$$

$$\Omega_D = \frac{1}{2}\triangle z(w_{i-1,k+1} + 2w_{i-1,k} + w_{i-1,k-1}) \tag{14}$$

In the case of turbulence, turbulence with a relatively large structure

was calculated directly. For turbulence smaller than the grid size, the large eddy simulation technique that utilizes the sub-grid scale (SGS) model was used, and the Smagorinsky SGS model (Smagorinsky, 1963) expressed using the following equations was used.

$$\nu_t = \nu + \nu_l \tag{15}$$

$$\nu_l = (C_S \Delta)^2 |S| \tag{16}$$

$$|S| = (2 S_{ij} S_{ij})^{1/2} \tag{17}$$

$$S_{ij} = \frac{1}{2}\left(\frac{\partial u_i}{\partial x_j} + \frac{\partial u_j}{\partial x_i}\right) \tag{18}$$

$$\Delta = (\Delta x \Delta z)^{1/2} \tag{19}$$

where ν is the kinematic viscosity coefficient, ν_l is the kinematic eddy viscosity of SGS, Δ is the filter length scale, and S_{ij} is the deformation tensor at the grid size. As for the C_S value, Schumann (1987) proposed a value ranging from 0.07 to 0.21, but 0.1 was used in this study because it was applied in a similar study (Christensen and Deigaard, 2001; Okayasu et al., 2005).

4.1 Flow Field, Vorticity Distribution, Turbulence Distribution, and Wave Height Distribution According to the Crest Depth

Figs. 9 and 10 show the flow field, vorticity distribution, and turbulence distribution according to the crest depth of the vegetation zone. Fig. 11 shows the wave height distribution around the submerged rigid vegetation according to the crest depth. From Figs. 9 and 10(a), clockwise (−) and counterclockwise (+) vortices can be

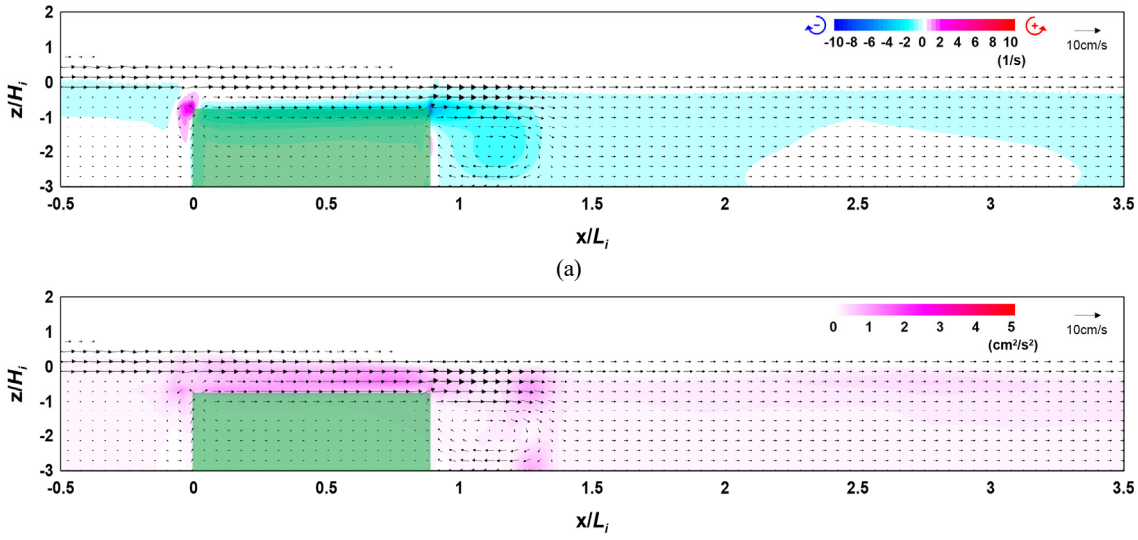

Fig. 9 Flow field, vorticity distribution, and turbulence distribution around the vegetation (Case CR-03, R/H_i = 0.563): (a) flow field and vorticity distribution; (b) flow field and turbulence distribution

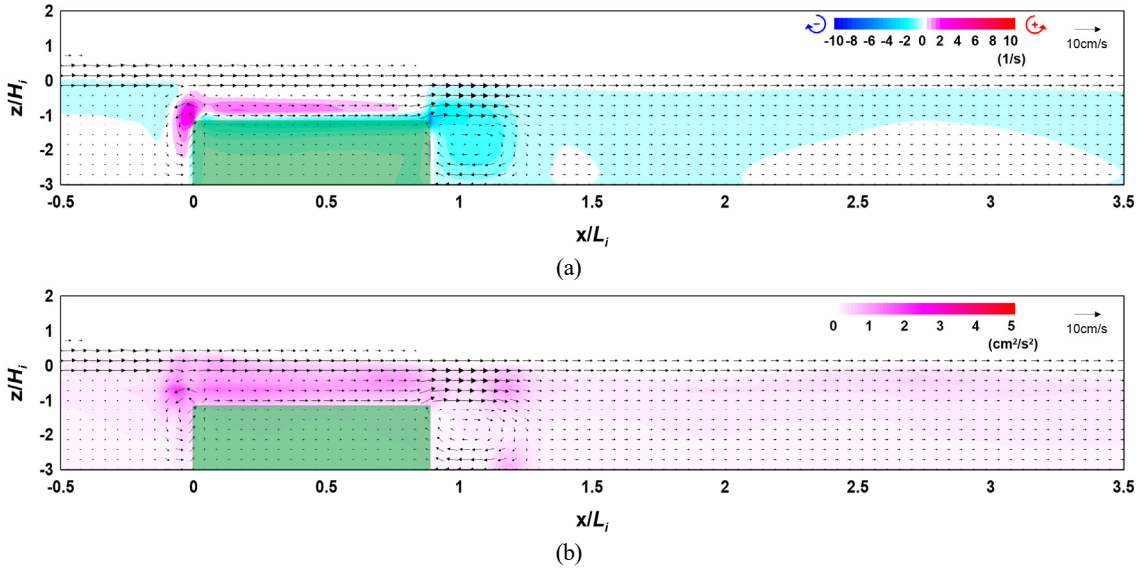

Fig. 10 Flow field, vorticity distribution, and turbulence distribution around the vegetation owing to the ridge (Case CR-05, R/H_i= 0.938): (a) flow field and vorticity distribution; (b) flow field and turbulence distribution

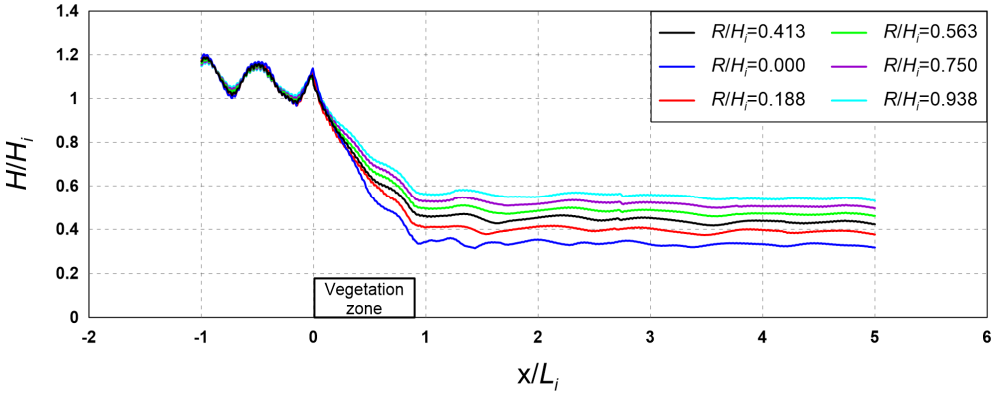

Fig. 11 Wave height distribution according to changes in crest depth of the vegetation zone (R/H_i)

confirmed in the vorticity distribution around the rigid vegetation. Additionally, a strong vorticity distribution is formed in the clockwise direction behind the vegetation, and the case of Fig. 9(a) with a low crest depth shows a stronger and wider vorticity distribution than the case of Fig. 10(a).

Figs. 9 and 10(b) show that a large turbulence distribution is formed at the crest and back of the submerged vegetation. This is because strong flow velocity corresponding to breaking waves occurs on the crest of the rigid vegetation. Additionally, the turbulence intensity on the crest of the rigid vegetation is higher and the turbulence distribution behind the rigid vegetation is wider in the case of Fig. 9(b). However, the crest depth was lower than that shown in the case of Fig. 10(b).

In Fig. 11, it can be seen that a slight partial standing wave field is formed in front of the submerged rigid vegetation under the influence of the reflected waves by the vegetation, and the height of waves that pass through the vegetation is reduced at the back by the energy dissipation caused by the resistance of the vegetation. This wave height attenuation effect tended to increase as the crest depth decreased as with the characteristics of typical submerged breakwaters.

4.2 Flow Field, Vorticity Distribution, Turbulence Distribution, and Wave Height Distribution According to the Width

Figs. 12–14 show the flow field, vorticity distribution, and turbulence distribution according to the width of the vegetation zone. Fig. 15 shows the wave height distribution around the submerged vegetation according to the width. From Figs.. 12(a), 13(a), and 14(a), it can be seen that the flow velocity decreases as the width of the vegetation zone increases owing to a reduction in waves that propagate onto the vegetation crest, thereby forming a strong clockwise vorticity distribution behind the submerged vegetation. From Figs. 12(b), 13(b), and 14(b), it can be seen that a large turbulence distribution is formed at the crest and back of the submerged vegetation, and that the turbulence intensity behind the vegetation zone increases as the width of the zone increases. Therefore, the increasing wave height attenuation effect alongside the increase in the width of the submerged vegetation can be confirmed by the wave height distribution shown in Fig. 15.

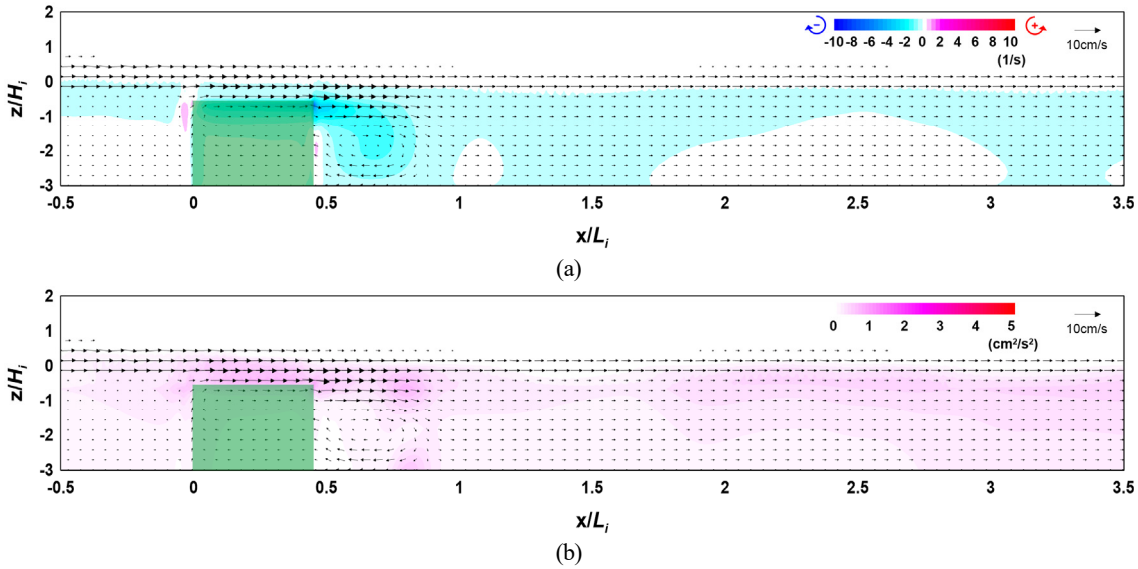

Fig. 12 Flow field, vorticity distribution, and turbulence distribution around the vegetation (Case CR-06, B/L_i = 0.447): (a) flow field and vorticity distribution; (b) flow field and turbulence distribution

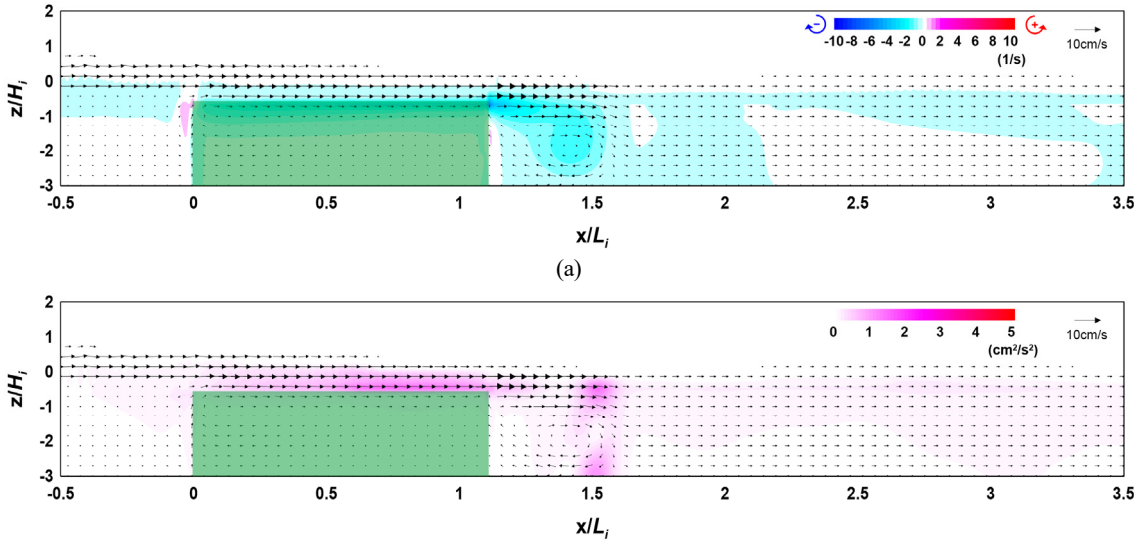

Fig. 13 Flow field, vorticity distribution, and turbulence distribution around the vegetation (Case CR-08, B/L_i = 1.107): (a) flow field and vorticity distribution; (b) flow field and turbulence distribution

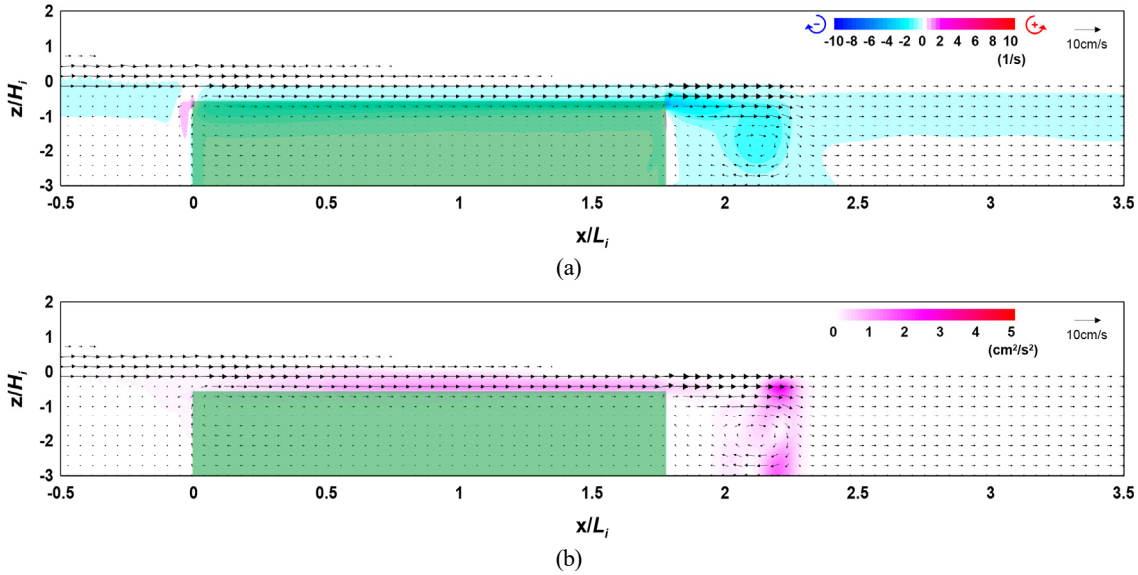

Fig. 14 Flow field, vorticity distribution, and turbulence distribution around the vegetation (Case CR-11, B/L_i = 1.773): (a) Flow field and vorticity distribution; (b) Flow field and turbulence distribution

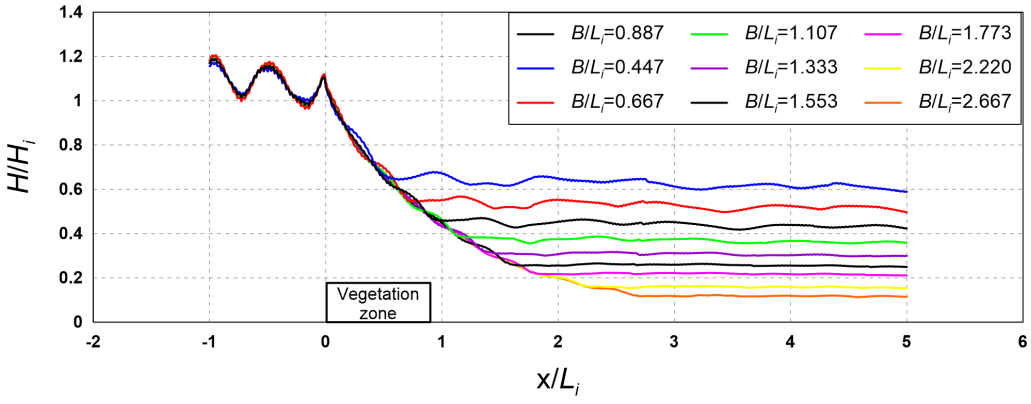

Fig. 15 Wave height distribution according to the change in the width of the vegetation zone (B/L_i)

The abovementioned results indicate that wave attenuation increases as the width of the submerged vegetation increases, and it is judged from the flow field, vorticity distribution, and turbulence distribution that submerged vegetation is more effective for wave attenuation as energy attenuation on the crest of the vegetation increases owing to the drag of the vegetation.

4.3 Flow Field, Vorticity Distribution, Turbulence Distribution, and Wave Height Distribution According to the Density

Figs. 16 and 17 show the flow field, vorticity distribution, and turbulence distribution according to the density of the vegetation zone. Fig. 18 shows the wave height distribution around the submerged vegetation according to the density. From Figs. 16(a) and 17(a), it can be seen that the flow velocity on the vegetation crest increases as the density of the vegetation zone increases, thereby forming a strong clockwise vorticity distribution behind the submerged vegetation. From Figs. 16(b) and 17(b), it can be seen that a large turbulence distribution is formed at the crest and back of the submerged vegetation, confirming that the turbulence intensity at the back increases as the density of the vegetation increases. Therefore, the increasing wave height attenuation effect alongside the increase in the density of the submerged vegetation can be confirmed by the wave height distribution shown in Fig. 18. Additionally, from Fig. 18, wave attenuation owing to the change in the wave on the vegetation crest can be confirmed together with the increase in reflectivity as the density of the submerged vegetation increases.

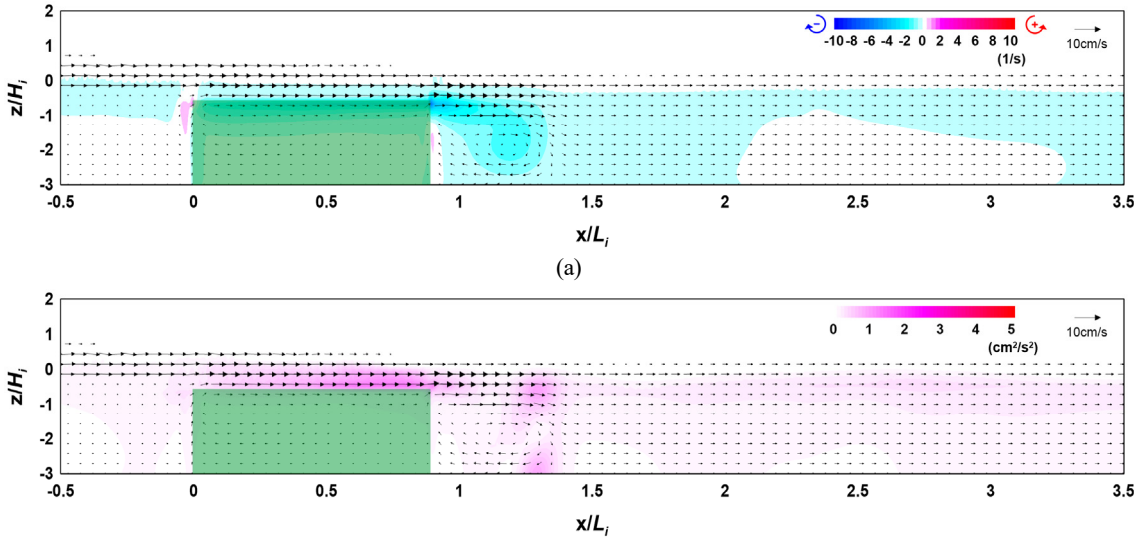

Fig. 16 Flow field, vorticity distribution, and turbulence distribution around the vegetation (Case CR-00, ρ_V = 0.123): (a) flow field and vorticity distribution; (b) flow field and turbulence distribution

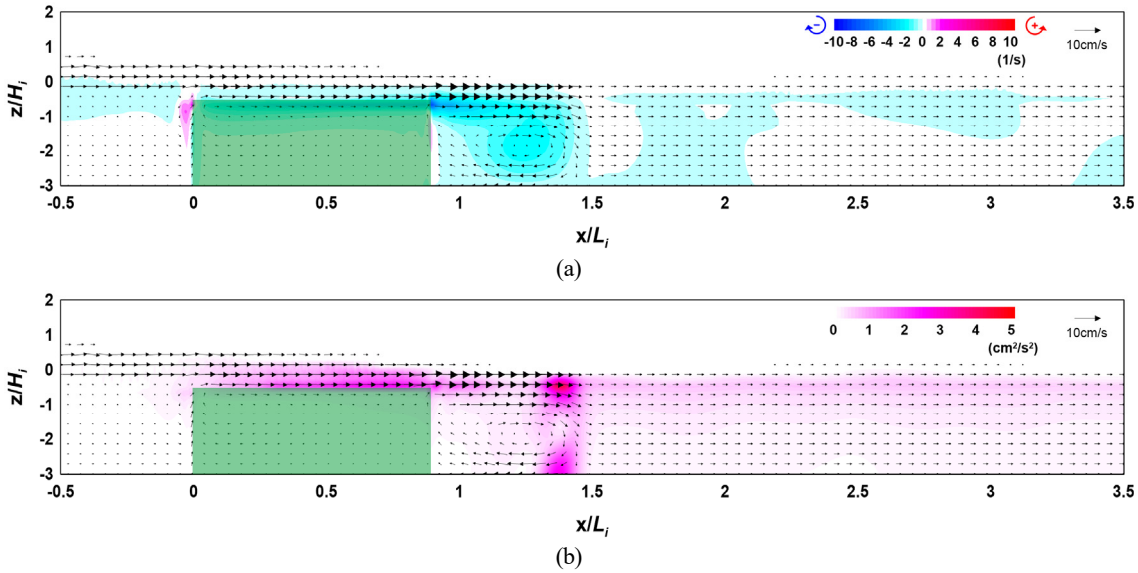

Fig. 17 Flow field, vorticity distribution, and turbulence distribution around the vegetation (Case CR-17, ρ_V = 0.213): (a) flow field and vorticity distribution; (b) flow field and turbulence distribution

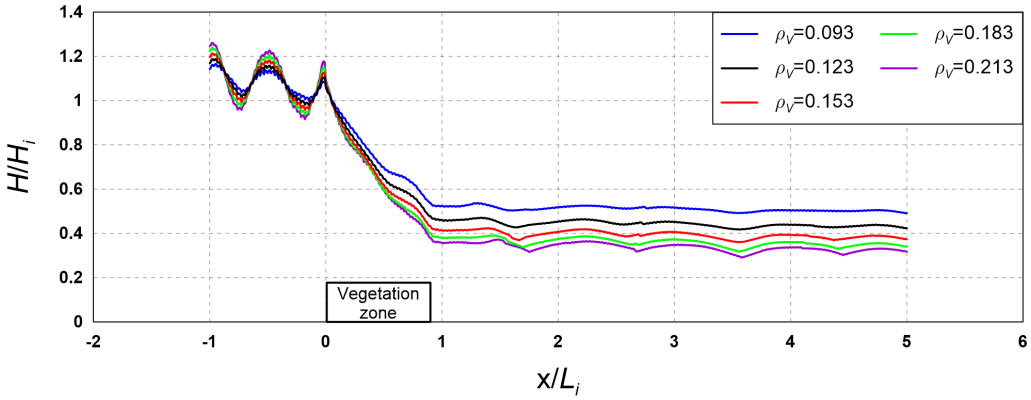

Fig. 18 Wave height distribution according to the changes in vegetation zone density (ρ_V)

The above results indicate that wave attenuation increases as the density of the submerged vegetation increases, and it is judged from the flow field, vorticity distribution, and turbulence distribution that submerged vegetation is more effective for wave attenuation as its density increases owing to the difference in energy attenuation at the crest and back of the vegetation.

4.4 Flow Field, Vorticity Distribution, Turbulence Distribution, and Wave Height Distribution According to the Arrangement Distance

Figs. 19–21 show the flow field, vorticity distribution, and turbulence distribution according to the multi-row arrangement distance of the vegetation zone. Fig. 22 shows the wave height distribution around the submerged vegetation according to the arrangement distance. From Figs. 19(a), 20(a), and 21(a), it can be seen that the flow velocity decreases as the arrangement distance increases owing to a reduction in waves that propagate onto the vegetation crest, thereby forming a strong clockwise vorticity distribution behind the submerged vegetation. From Figs. 19(b), 20(b), and 21(b), it can be seen that a large turbulence distribution is formed at the crest and back of the submerged vegetation, confirming that similar turbulence intensity occurs despite the increase in arrangement distance. Therefore, the similar wave height attenuation effect despite the increase in arrangement distance can be confirmed by the wave height distribution shown in Fig. 22.

The abovementioned results indicate that similar wave attenuation occurs regardless of the arrangement distance. From the flow field, vorticity distribution, and turbulence distribution, we assumed that similar energy attenuation occurs owing to the drag of the submerged vegetation.

This result is contrary to the wave attenuation effect by Bragg reflection that occurs when submerged breakwaters are arranged in multiple rows. This is because the submerged vegetation has relatively low reflectivity than submerged breakwaters owing to its low porosity. However, additional examinations are required for the wave energy reduction effect according to the multi-row arrangement and arrangement distance of the submerged rigid vegetation.

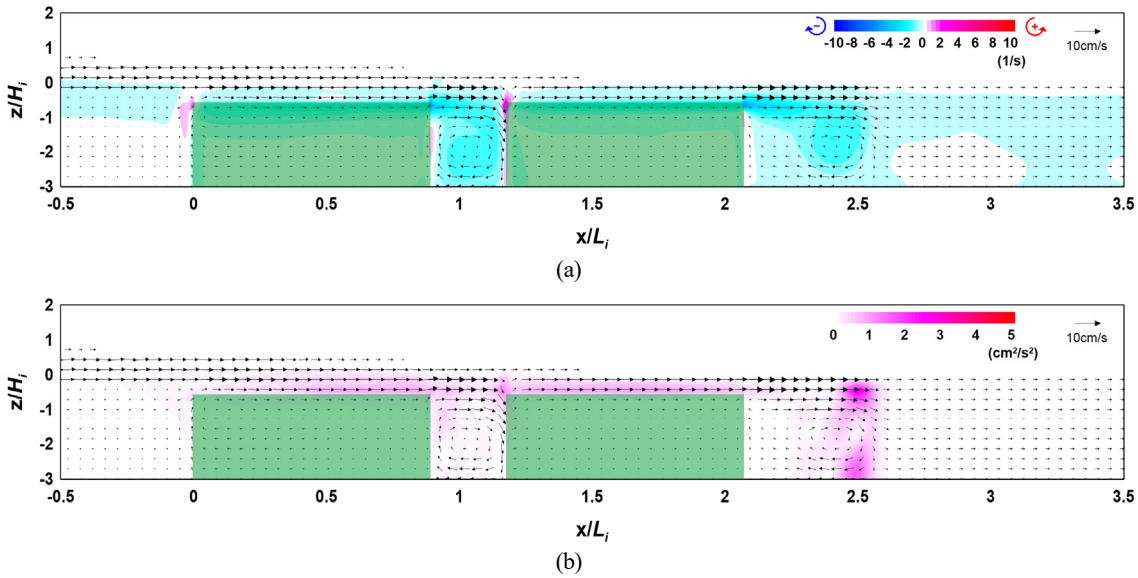

Fig. 19 Flow field, vorticity distribution, and turbulence distribution around the vegetation (Case CR-18, V_d/L_i = 0.293): (a) flow field and vorticity distribution; (b) flow field and turbulence distribution

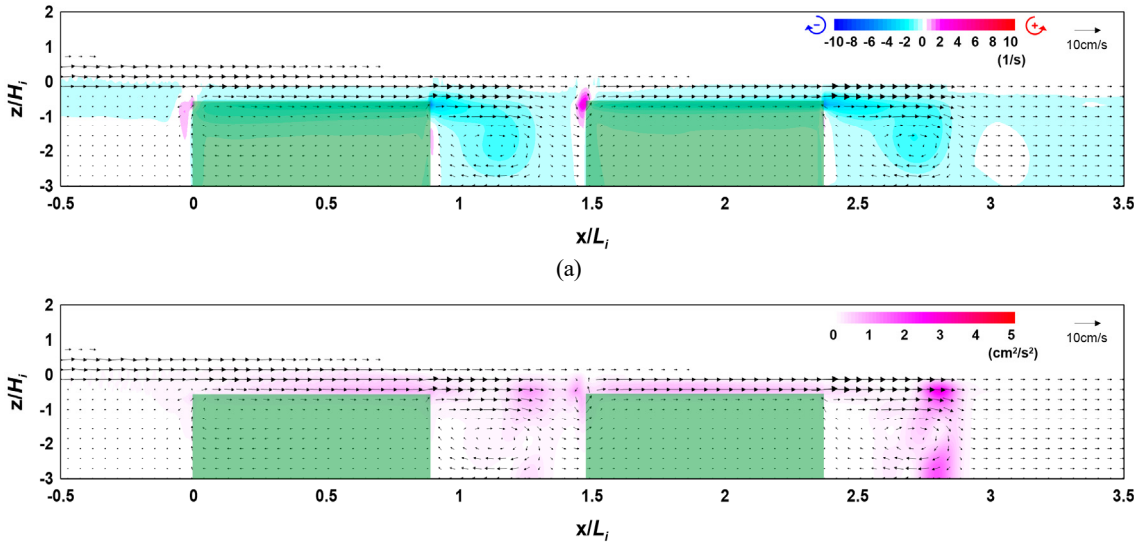

Fig. 20 Flow field, vorticity distribution, and turbulence distribution around the vegetation (Case CR-19, V_d/L_i = 0.593): (a) flow field and vorticity distribution; (b) flow field and turbulence distribution

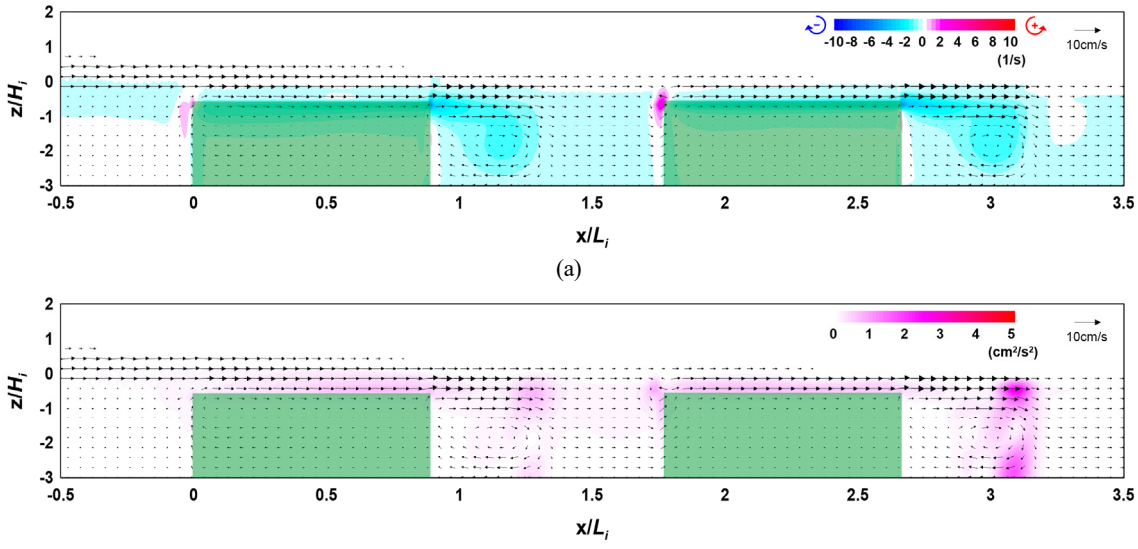

Fig. 21 Flow field, vorticity distribution, and turbulence distribution around the vegetation (Case CR-20, V_d/L_i = 0.887); flow field and vorticity distribution; (b) flow field and turbulence distribution

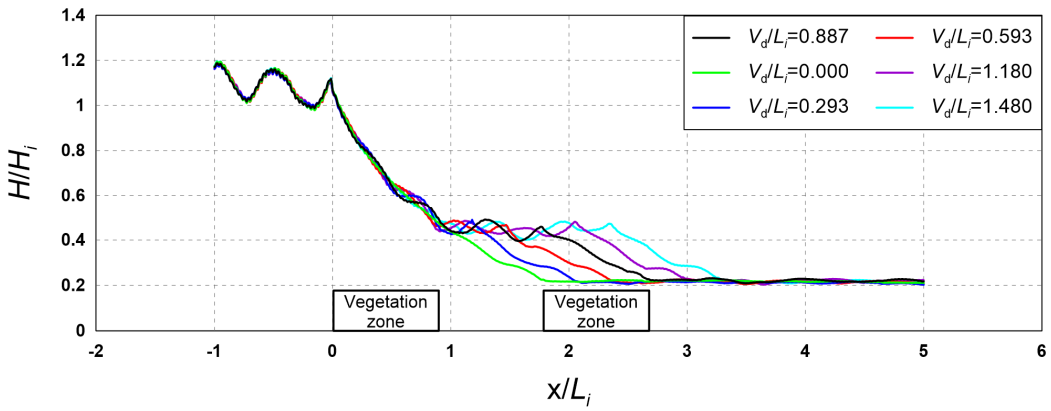

Fig. 22 Wave height distribution according to the arrangement distance of the vegetation zone (V_d/L_i)

5. Conclusions

A hydraulic model experiment and a numerical model experiment were performed to analyze the hydraulic characteristics according to the cross-section changes in the submerged rigid vegetation. Using the hydraulic model experiment, the reflection coefficient, transmission coefficient, and energy dissipation coefficient were analyzed according to the density, width, and multi-row arrangement distance of the vegetation zone. Using the numerical model experiment, the flow field, vorticity distribution, turbulence distribution, and wave height distribution were analyzed according to the crest depth, density, width, and multi-row arrangement distance of the vegetation zone. The following conclusions were drawn based on the results obtained.

(1) From the hydraulic model experiment, the reflection coefficient, transmission coefficient, and energy dissipation coefficient according to the cross-section changes in vegetation were calculated. Additionally, the flow field, vorticity distribution, turbulence distribution, and wave height distribution according to the cross-section changes in vegetation were analyzed using the numerical wave tank, which was validated by comparing the results obtained from the hydraulic model experiment.

(2) The results of the hydraulic model experiment showed that the reflection coefficient decreased as the density of the vegetation zone decreased. This is because the transmission area of waves increased in front of the vegetation zone. Additionally, we found that the transmission coefficient increased as the density and width of the vegetation zone increased. This is because more breaking waves were induced at the crest of the vegetation zone as the density and width of the vegetation zone increased.

(3) The results of the numerical model experiment showed that the distribution and intensity of vorticity and turbulence increased at the crest and back of the vegetation zone as the crest depth of the vegetation zone decreased and width and density increased, thereby increasing the wave height attenuation performance.

(4) When the total width of the vegetation zone was identical, the vorticity distribution, turbulence distribution, and wave height distribution according to the multi-row arrangement and arrangement distance were found to be similar. However, we believe that more examinations are required for wave energy attenuation characteristics according to the multi-row arrangement and arrangement distance of the submerged rigid vegetation.

Conflict of Interest

No potential conflict of interest relevant to this article was reported.

Funding

This research was a part of the project titled “Practical Technologies for Coastal Erosion Control and Countermeasure”, funded by the Ministry of Oceans and Fisheries, Korea (20180404).

References

Abdolahpour, M., Hambleton, M., & Ghisalberti, M. (2017). The wave-driven current in coastal canopies. *Journal of Geophysical Research: Oceans, 122*(5), 3660–3674. https://doi.org/10.1002/2016JC012446

Anderson, M. E., McKee Smith, J., & McKay, S. K. (2011). Wave dissipation by vegetation. ERDC/CHL CHETN-I-82.

Asano, T., Tsutsui, S., & Sakai. T. (1988). 海藻が繁茂する場の波高減衰の特性 [Wave damping characteristics due to seaweed]. *Proceedings of the Japanese Conference on Coastal Engineering, 35*, 138–142. https://doi.org/10.2208/proce1970.35.138

Beudin, A., Kalra, T. S., Ganju, N. K., & Warner, J. C. (2017). Development of a coupled wave-flow-vegetation interaction model. *Computers & Geosciences, 100*, 76–86. https://doi.org/10.1016/j.cageo.2016.12.010

Blackmar, P. J., Cox, D. T., & Wu, W. C. (2014). Laboratory observations and numerical simulations of wave height attenuation in heterogeneous vegetation. *Journal of Waterway, Port, Coastal, and Ocean Engineering, 140*(1), 56–65.

Cho, W. C. (2006). Optimum distance between multiple submerged breakwaters for wave screening performance enhancement. *Journal of Ocean Engineering and Technology, 20*(6), 82–87.

Cho, Y. S., Lee, J. I., & Kim, Y. T. (2002). Hydraulic experiments on reflection of regular waves due to rectangular submerged breakwaters. *Journal of Korea Water Resources Association, 35*(5), 563–573. https://doi.org/10.3741/JKWRA.2002.35.5.563

Christensen, E. D., & Deigaard, R. (2001). Large eddy simulation of breaking waves. *Coastal Engineering, 42*(1), 53–86. https://doi.org/10.1016/S0378-3839(00)00049-1

Goda, Y., & Suzuki, T. (1976). Estimation of incident and reflected waves in random wave experiments. *Coastal Engineering Proceedings, 1*(15), 47. https://doi.org/10.9753/icce.v15.47

Hadadpour, S., Paul, M., & Oumeraci, H. (2019). NNumerical investigation of wave attenuation by rigid vegetation based on a porous media approach. *Journal of Coastal Research, 92*(SI), 92–100. https://doi.org/10.2112/SI92-011.1

Hu, Z., Suzuki, T., Zitman, T., Uittewaal, W., & Stive, M. (2014). Laboratory Study on Wave Dissipation by Vegetation in Combined Current–wave flow. *Coastal Engineering, 88*, 131–142. https://doi.org/10.1016/j.coastaleng.2014.02.009

Hur, D. S., & Choi, D. S. (2008). Effect of the slope gradient of a permeable submerged breakwater on wave field around it. *Journal of Korean Society of Civil Engineers*, *28*(2B), 249–259.

Jeong, Y. M., & Hur, D. S. (2016). Numerical experiment of wave attenuation considering behavior of vegetation zone. *Journal of Korean Society of Coastal and Ocean Engineers, 28*(4), 232–239. https://doi.org/10.9765/KSCOE.2016.28.4.232

Kirby, J. T., & Anton, J. P. (1990). Bragg reflection of waves by artificial bars. *Coastal Engineering Proceedings, 1*(22).

Lee, W. D., Cox, D. T., & Hur, D. S. (2017a). Numerical model study

on the wave and current control by coastal vegetation. *Journal of Coastal Research, 79*(10079), 219–223. https://doi.org/10.2112/SI79-045.1

Lee, W. D., Park, J. R., Jeon, H. S., & Hur, D. S. (2017b). Effects of tsunami waveform on energy dissipation of aquatic vegetation. *Journal of Ocean Engineering and Technology, 31*(2), 121–129. https://doi.org/10.5574/KSOE.2017.31.2.121

Manca, E., Stratigaki, V., & Prinos, P. (2010). Large scale experiments on spectral wave propagation over Posidonia oceanica seagrass. *Proceedings of 6th International Symposium on Environmental Hydraulics*, 463–469.

Maza, M., Lara, J. L., Losada, I. J., Ondiviela, B., Trinogga, J., & Bouma, T. J. (2015). Large-scale 3-D experiments of wave and current interaction with real vegetation. Part 2: Experimental analysis. *Coastal Engineering, 106*, 73–86. https://doi.org/10.1016/j.coastaleng.2015.09.010

Mitsuyasu, H. (1969). On the growth of wind-generated waves (Ⅱ). *Research Institute for Applied Mechanics, Kyushu University, 17*(59), 235–248.

Okayasu, A., Suzuki, T., & Matsubayashi, Y. (2005). Laboratory experiment and three-dimensional large eddy simulation of wave overtopping on gentle slope seawalls. *Coastal Engineering Journal, 47*(2-3), 71–89. https://doi.org/10.1142/S0578563405001215

Peruzzo, P., De Serio, F., Defina, A., & Mossa, M. (2018). Wave height attenuation and flow resistance due to emergent or near-emergent vegetation. *Water, 10*(4), 402. https://doi.org/10.3390/w10040402

Raffel, M., Willert, C. E., & Kompenhans, J. (1998). *Particle image velocimetry: a practical guide* (Vol. 2). Berlin: Springer.

Raffel, M., Willert, C. E., Wereley, S. T., & Kompenhans, J., (2007). *Particle image velocimetry*. Berlin: Springer-Verlag. https://doi.org/10.1007/978-3-540-72308-0

Sakakiyama, T., & Kajima, R. (1992). Numerical simulation of nonlinear wave interacting with permeable breakwaters. *Coastal Engineering Proceedings, 1*(23), 1517–1530.

Schumann, U. (1987). Direct and large eddy simulation of turbulence. Summary of the state of art 1987. *Von Karman Institute for Fluid Dynamics.*

Smagorinsky, J. (1963). General circulation experiments with the primitive equations: I. The basic experiment. *Monthly Weather Review, 91*(3), 99–164. https://doi.org/10.1175/1520-0493(1963)091<0099:GCEWTP>2.3.CO;2

van Veelen, T. J., Fairchild, T. P., Reeve, D. E., & Karunarathna, H. (2020). Experimental study on vegetation flexibility as control parameter for wave damping and velocity structure. *Coastal Engineering, 157*, 103648. https://doi.org/10.1016/j.coastaleng.2020.103648

Wang, H., Yin, Z., Luan, Y., Wang, Y., & Liu, D. (2022). Hydrodynamic characteristics of idealized flexible vegetation under regular waves: Experimental investigations and analysis. *Journal of Coastal Research, 38*(3), 673–680. https://doi.org/10.2112/JCOASTRES-D-21-00089.1

Wu, W. C., & Cox, D. T. (2015). Effects of wave steepness and relative water depth on wave attenuation by emergent vegetation. *Estuarine, Coastal and Shelf Science, 164*, 443–450. https://doi.org/10.1016/j.ecss.2015.08.009

Author ORCIDs

Author name	ORCID
Lee, Jeongheum	0000-0003-1827-5478
Jeong, Yeon-Myeong	0000-0003-3349-1427
Kim, Jun-Seok	0000-0002-6522-3585
Hur, Dong-Soo	0000-0003-4627-7593

KSOE

Journal of Ocean Engineering and Technology 36(5), 340-352, October, 2022
https://doi.org/10.26748/KSOE.2022.019

pISSN 1225-0767
eISSN 2287-6715

Original Research Article

Underwater Navigation of AUVs Using Uncorrelated Measurement Error Model of USBL

Pan-Mook Lee[1], Jin-Yeong Park[1], Hyuk Baek[2], Sea-Moon Kim[1], Bong-Huan Jun[1], Ho-Sung Kim[3] and Phil-Yeob Lee[3]

[1]*Principal Researcher, Ocean System Engineering Research Division, KRISO, Daejeon, Korea*
[2]*Engineer, Ocean System Engineering Research Division, KRISO, Daejeon, Korea*
[3]*Senior Engineer, Ocean System Team, Hanwha System Corporation, Gumi-si, Gyeongbuk, Korea*

KEY WORDS: Underwater navigation, Outlier rejection, Ultra-short baseline acoustic positioning system, Mahalanobis distance, Uncorrelated measurement error, Autonomous underwater vehicle

ABSTRACT: *This article presents a modeling method for the uncorrelated measurement error of the ultra-short baseline (USBL) acoustic positioning system for aiding navigation of underwater vehicles. The Mahalanobis distance (MD) and principal component analysis are applied to decorrelate the errors of USBL measurements, which are correlated in the x- and y-directions and vary according to the relative direction and distance between a reference station and the underwater vehicles. The proposed method can decouple the radial-direction error and angular direction error from each USBL measurement, where the former and latter are independent and dependent, respectively, of the distance between the reference station and the vehicle. With the decorrelation of the USBL errors along the trajectory of the vehicles in every time step, the proposed method can reduce the threshold of the outlier decision level. To demonstrate the effectiveness of the proposed method, simulation studies were performed with motion data obtained from a field experiment involving an autonomous underwater vehicle and USBL signals generated numerically by matching the specifications of a specific USBL with the data of a global positioning system. The simulations indicated that the navigation system is more robust in rejecting outliers of the USBL measurements than conventional ones. In addition, it was shown that the erroneous estimation of the navigation system after a long USBL blackout can converge to the true states using the MD of the USBL measurements. The navigation systems using the uncorrelated error model of the USBL, therefore, can effectively eliminate USBL outliers without loss of uncontaminated signals.*

1. Introduction

The ultra-short baseline (USBL) acoustic positioning system measures the bearing angle and slant angle of the received acoustic signal and converts the propagation delay time of the sound wave into a distance. It is an underwater acoustic positioning device that measures the relative position of an underwater object via a triangulation method using two angles orthogonal to the distance (Milne, 1983). The USBL system has advantage of being convenient for operation owing to its ability to measure the position of an underwater object using a single transceiver. For this reason, it is widely used for the location tracking of remotely operated vehicles and autonomous underwater vehicles (AUVs). In addition, the USBL can measure the position of the underwater object within a certain error bound regardless of the elapsed time. It is also employed as an auxiliary sensor for aiding the navigation systems of underwater vehicles composed of inertial sensors (Vasilijevic et al., 2012; Lee et al., 2017).

To use the USBL position measurements for aiding a navigation system, an error modeling system of the USBL is required. The main sources of errors are the physical properties of the acoustic propagation medium, diffraction, and non-uniform underwater environments (temperature gradient, pressure gradient, etc.). So characteristics of the errors varies depending on factors such as multi-pass of acoustic propagation, variation of ambient noise caused by passing ships, unique features of the transceiver array (i.e. range-

Received 27 June 2022, revised 12 August 2022, accepted 13 August 2022
Corresponding author Pan-Mook Lee: +82-42-866-3810, pmlee@kriso.re.kr
This article is based on a thesis presented at the Korean Association of Ocean Science and Technology Societies (KAOSTS) Joint Symposium and is a detailed and expanded version of it (Lee et al., 2022).

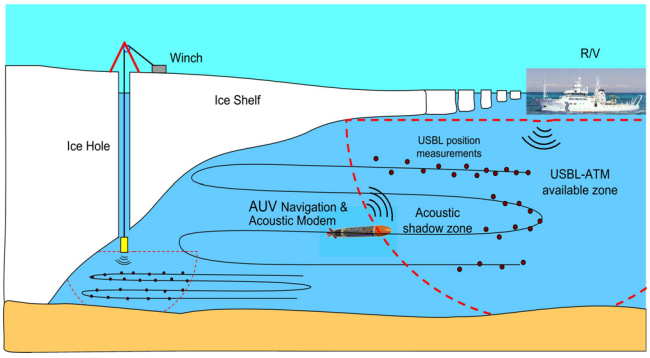

Fig. 1 Integrated navigation aided with a USBL and an acoustic telemetry modem for exploration of the Antarctic Ocean under an ice shelf

dependent error in the angular direction), and misalignment of the transceiver mounted on the vehicle frame. The USBL is particularly sensitive to noise because it measures the reception angle to calculate the phase difference of the signal received by the transceiver array (Luo et al., 2021). This makes the USBL prone to outliers. Since the USBL's position error increases in proportion to range, the position measurement in the horizontal plane shows nonlinear tendencies when the operating depth is smaller than the measurement range. The USBL, in case of which tracks the positions of underwater vehicles operated in shallow water, has an elliptical distribution of measurement errors according to the distances from the reference station to the AUVs. Furthermore the principal axis of the elliptical distribution changes according to the positions of the vehicles relative to the reference station. Therefore, when USBL positioning measurements are used for aiding an underwater navigation system of an underwater vehicle operating in shallow water, a measurement model including the nonlinear characteristics of the errors is required. In particular, it is essential to design a filter that can selectively reject outliers for a robust navigation system. To utilize the USBL signal for the navigation system even in abnormal situations, such as blackout or frequent outliers of USBL measurements, it is necessary to ensure the stability of the navigation system with outlier rejection and reduce the position errors after when the USBL signal reception is recovered from the blackout. For example, as shown in Fig. 1, USBL tracking of the locations of AUVs operating under an ice shelf requires not only the rejection of outliers but also decision on integrity of the USBL signals received after a long time of blackout (Park, 2021).

An AUV position measured by USBL is defined using the Earth coordinates. However, the acceleration, angular velocity, and speed used in the navigation of the AUV are defined using the body-fixed coordinates of the vehicle. The position measurement tolerance of the USBL can be modeled in the Earth coordinate system by separating the direction toward the vehicle and the direction orthogonal thereto. As the vehicle moves, the position and heading change constantly. So, the three-dimensional (3D) error component of the USBL defined in the body coordinate system of the vehicle changes according to the attitude and heading of the vehicle. To use the USBL position signal as an auxiliary signal for aiding a navigation of the vehicle, it is necessary to transform the global coordinate to the body frame of the USBL measurements. The error covariance of the USBL defined in the body coordinate system of the vehicle is correlated between the coordinate axes. When this correlation error covariance model is applied to the navigation system, the outlier decision level should be set to large values, ensuring that the normal USBL signals are not lost. If the navigation system is designed in such a way, outliers within the threshold, which have to be rejected, can be recognized as signals. Therefore, the outlier determination area should be minimized so that only the outliers are rejected while normal signals are secured. Uncorrelated error modeling is one of the potential methods for reducing the outlier decision area.

In the studies on outlier rejection, De Maesschalck et al. (2000) defined the Mahalanobis distance (MD) and determined its relationship with the Euclidean distance (ED) through principal component analysis (PCA). They explained and discussed the techniques based on the MD and outlier rejection applied in multivariate calibration, pattern recognition and process control. Chang (2014) proposed a robust Kalman filter to reject the outliers from the measurement signal. By assuming that the difference between the measured signals containing noise and the estimated state was a Gaussian distribution, he set outlier judgment indices and statistically treated them as null hypotheses to perform tests on actual observations. In the case of outliers, a scale factor was introduced to readjust the covariance of measurement noise, and a solution was obtained using Newton's repetitive method or an analytical method. However, this approach may not be practical if the number of repetitions increases. Hassan et al. (2021) proposed a method for rejecting outliers via repeated smoothing process with an image signal and a low-cost inertial sensor in underwater. By installing reference markers on an underwater structure and updating the innovation and covariance when the acquired image information is valid, they showed that outliers can be removed and navigation accuracy can be improved through experiments. Zhu et al. (2021) proposed an improved Kalman filter algorithm based on MD algorithm to deal with outliers. For a strap-down inertial navigation system (SDINS) aided with a DVL, the adaptive and robust estimation of the error covariance was developed to suppress the effect of the non-Gaussian noise. To design the robust filter adapting to the environment, they used an MD algorithm for the DVL signal containing the non-Gaussian noise. A simulation was performed using the in-flight alignment test data of the DVL-aided SDINS. They showed that the covariance matrix could be adaptively estimated in real time and the outliers could be effectively suppressed.

This paper proposes a method of modeling the measurement error of USBL as an uncorrelated error in the horizontal plane for the design of a robust underwater vehicle navigation system to outlier, which uses MD and principal component analysis of the USBL error model. Using this method, the error characteristics of the USBL positioning data can be decomposed and set to the principal axis of normal distribution in

the MD. We analyzed the feature of position measurements of the USBL and modeled the inherent error characteristics of the USBL measurement system accordingly. The difference between the position estimated by the navigation system of the vehicle and the measured position was updated with a Kalman filter having the modulated error covariance of measurements on the basis of the MD. To evaluate performance of the outlier rejection with the error model, a simulation on the underwater navigation of an AUV was conducted with a data set of surface maneuvering test of the vehicle. This paper investigated the robustness of the outliers rejection among the USBL measurements as well as the effects of the varying magnitude and direction of the measurement error covariance on the performance of the navigation system . Through the simulation of the navigation aided by USBL measurements, it was confirmed that the proposed method is more robust to reject outliers than a conventional method. This paper also examined that the erroneous estimation of the navigation system after a long USBL blackout can converge to the true states using the MD of the USBL measurements.

2. Underwater Navigation Aided with USBL

2.1 Position Measurements of USBL in the Horizontal Plane

USBL is performed by measuring the bearing angle $\psi_{bearing}$ and the slant angle θ_{slant} of the two directions that are orthogonal to each other as well as the time delay of the transmitted-received signal δT, as shown in Fig. 2. If the sound velocity c is known, the relative three-dimensional position in underwater can be calculated with one range $R(=c\,\delta T/2)$ and two angles $\psi_{bearing}$ and θ_{slant}. When the water depth is greater than the horizontal distance, the horizontal position measurement error can be assumed to have independent normal distributions in the x- and y-directions. In this condition, the USBL

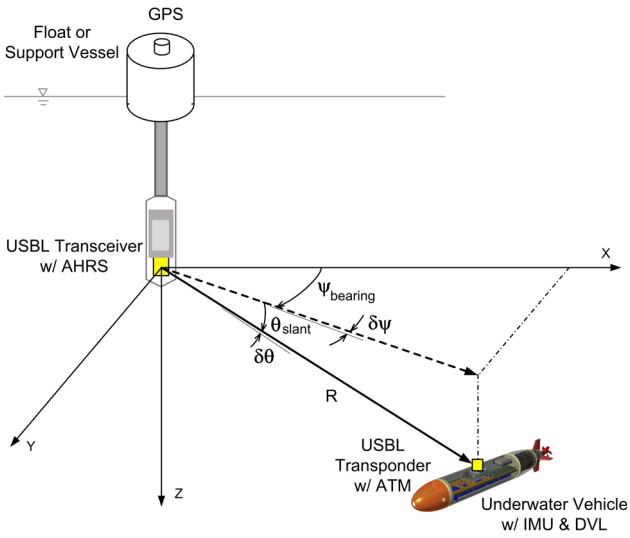

Fig. 2 Angular measurement errors of the USBL acoustic positioning system

system has been successfully applied to aiding a navigation system as an auxiliary sensor in a previous study (Lee et al., 2017). If an AUV is performing a long-range exploration in an ice sheet or operating in a shallow water, the error in the radial direction will be constant regardless of the range as well. However, the error in the angular direction that is perpendicular to the radial direction will increase with range. Therefore, an error modeling approach of the USBL able to handle this feature should be developed for aiding underwater navigation in shallow water.

In this article, the MD is introduced for the error modeling of measurement equations of USBL. Considering the characteristics of commercially available USBL 18/34 (EvoLogics, 2017), a virtual USBL measurement data set was generated whereby the characteristics of each location were analyzed. A simulation was performed for the cases where the rms error of range was 1 m and the rms error of angle was 1°, in which it was assumed that the range error and angular error of the USBL had a normal Gaussian distribution. In such cases where an underwater vehicle operating at a depth of 10 m was stationary at a horizontal distance of 50, 100, 300, or 500 m from a reference station with 0°, 45°, and 90° bearing angles centered on the USBL transceiver on the station, a series of data set was simulated to track the stationary vehicle at each location with the USBL. These data were generated with random noise following a normal distribution, assuming a 10-min measurement at 2 samples per second. The number of each dataset is 300. Fig. 3 shows the simulated positions of the USBL measurement for 12 locations. As the relative range increased, the error in the direction perpendicular to the radial direction increased linearly, and the principal axis of the elliptical error distribution changed according to the relative bearing angle. The left column of Fig. 4 presents an enlarged view of the position measurement data at

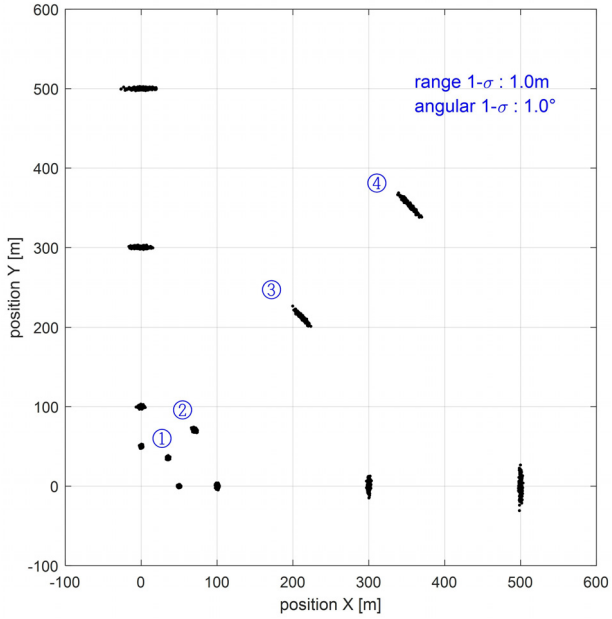

Fig. 3 Simulated USBL measurements with root-mean-square (rms) errors of the heading and range ($\delta\psi$ = 1°, δr = 1 m) at a depth of d = 10 m

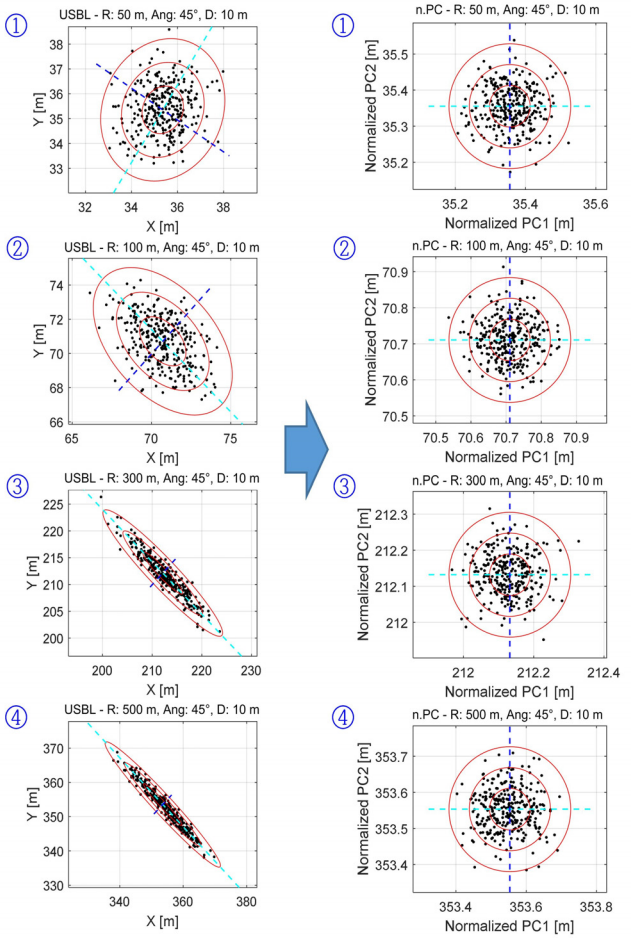

Fig. 4 (Left) measurement errors at positions ① to ④ in Euclidean space, (right) normalized principal components (PCs) of the measurements in the Mahalanobis distance

each position for points ①–④ with a 45° bearing angle. Here, the angular direction error of the simulated positions of the USBL exhibits a distorted oval-shaped distribution and increases in proportion to the range of the vehicle. In the figure, the concentric ellipses represent the contours equivalent to $(\sigma_1, 2\sigma_1, 3\sigma_1)$ of the standard deviation σ_1 of the first principal component (PC1) for each position dataset. Because the error distribution of the USBL measurement has nonlinear characteristics, underwater vehicles operating in shallow water require an error modeling to consider the correlation between the *x*- and *y*-axis directions.

2.2 MD and PCA of the USBL Measurements

The MD and PCA were reviewed prior to modeling the USBL position data. Assuming that the USBL localization error has a normal Gaussian distribution with mean $\boldsymbol{\mu}$ and covariance $\boldsymbol{\Sigma}$, the probability density function of the k-dimensional multivariate vector $\boldsymbol{X} = (X_1,\ldots,X_k)^T$ is expressed as follows:

$$f_{\boldsymbol{X}}(x_1,\ldots,x_k) = \frac{\exp\{-(\boldsymbol{x}-\boldsymbol{\mu})^T\boldsymbol{\Sigma}^{-1}(\boldsymbol{x}-\boldsymbol{\mu})/2\}}{\sqrt{(2\pi)^k|\boldsymbol{\Sigma}|}} \quad (1)$$

where $\boldsymbol{\Sigma}$ is the covariance matrix $\boldsymbol{\Sigma} = \frac{1}{N}(\boldsymbol{X}-\boldsymbol{\mu})^T(\boldsymbol{X}-\boldsymbol{\mu})$, and the square root of the matrix of the exponential function $\sqrt{(\boldsymbol{x}-\boldsymbol{\mu})^T\boldsymbol{\Sigma}^{-1}(\boldsymbol{x}-\boldsymbol{\mu})}$ represents the MD. Each element of the multivariate vector MD_i can be calculated as $\sqrt{(\boldsymbol{x}_i-\boldsymbol{\mu})\boldsymbol{\Sigma}^{-1}(\boldsymbol{x}_i-\boldsymbol{\mu})^T}$. Because the USBL position projected to the horizontal plane is two-dimensional (2-D), the covariance matrix is given as follows:

$$\boldsymbol{\Sigma} = \begin{bmatrix} \sigma_1^2 & \rho_{12}\sigma_1\sigma_2 \\ \rho_{12}\sigma_1\sigma_2 & \sigma_2^2 \end{bmatrix}, \quad (2)$$

and the MD in the 2-D horizontal plane is expressed as follows (De Maesschalck et al., 2000):

$$\mathrm{MD}_i = \sqrt{\left(\frac{x_{i1}-\mu_1}{\sigma_1}\right)^2 + \left(\frac{x_{i2}-\mu_2}{\sigma_2} - \rho_{12}\frac{x_{i1}-\mu_1}{\sigma_1}\right)^2 \frac{1}{1-\rho_{12}}} \quad (3)$$

Here, σ_1 and σ_2 represent the standard deviations of the principal components, and ρ_{12} represents the correlation coefficient between x_1 and x_2. If the standard deviations in the *x*- and *y*-axis directions are equal, the MD is equal to the ED ($\mathrm{MD}_i = \mathrm{ED}_i$).

For the PCA, consider a data matrix of $\boldsymbol{X}(n\times p)$ that includes n measurements ($\boldsymbol{x}_i$) composed of p variables. $\boldsymbol{X}_c$ is determined by removing the mean $\overline{\boldsymbol{x}}_j$ from each column vector $\boldsymbol{x}_j(n\times 1)$ in the data matrix $\boldsymbol{X}(n\times p)$. In this sense, if singular value decomposition is performed, $\boldsymbol{X}_c$ can be expressed as

$$\boldsymbol{X}_c = \boldsymbol{U}(n\times a)\,\boldsymbol{\Lambda}(a\times a)\,\boldsymbol{V}(p\times a)^T \quad (4)$$

where $\boldsymbol{\Lambda}$ is a diagonal matrix of singular values λ_i for $i=1,\ldots,a$ which is interpreted as the total variance for each principal component (PC) ordered as $\lambda_1 > \lambda_2 > \ldots > \lambda_a$. $\boldsymbol{U}$ is a column vector indicating the normalized value for each PC axis, and $\boldsymbol{V}$ is a unit matrix indicating the direction of the PC axis.

When applied to the position measurement data of the USBL, the position data on the horizontal plane are 2-D; thus, $p=2$, $a=2$, and the USBL dataset, i.e., (x, y), can be handled using the PCA. The average of the position dataset is calculated and eliminated, and the PCA can be performed on the matrix X_c as follows, by using the singular value decomposition of the MATLAB function *svd()*.

$$[U,\ S,\ V] = svd(X_c,\ 'econ'); \quad (5)$$

Here, S represents the diagonal matrix of the singular values $\boldsymbol{\Lambda}$. The right column of Fig. 4 indicates that the normalized MD data of the USBL position error of points ①–④ have a 2-D symmetric normal distribution. As shown in Table 1, as the range increases, the first singular value of the PC (PC1) increases proportionally (0.99, 1.75,

Table 1 Standard deviation for the principal axis of the relative position of the USBL

Location (Depth = 10 m, Direction = 45°)	Sigma matrix $\sqrt{S}$ (Standard deviation)	Principal-axis matrix V
R = 50 m	$\begin{bmatrix} 0.993 & 0 \\ 0 & 0.857 \end{bmatrix}$	$\begin{bmatrix} 0.539 & 0.842 \\ 0.842 & -0.539 \end{bmatrix}$
R = 100 m	$\begin{bmatrix} 1.750 & 0 \\ 0 & 1.068 \end{bmatrix}$	$\begin{bmatrix} 0.721 & -0.693 \\ -0.693 & -0.721 \end{bmatrix}$
R = 300 m	$\begin{bmatrix} 5.550 & 0 \\ 0 & 0.913 \end{bmatrix}$	$\begin{bmatrix} 0.715 & 0.699 \\ 0.699 & 0.715 \end{bmatrix}$
R = 500 m	$\begin{bmatrix} 8.545 & 0 \\ 0 & 0.981 \end{bmatrix}$	$\begin{bmatrix} -0.705 & 0.709 \\ 0.709 & 0.705 \end{bmatrix}$

5.55, and 8.55). However, the singular value of the second PC (PC2) does not change significantly. In Fig. 4, concentric circles represent the equidistance of the Mahalanobis distance MD, 2MD, and 3MD corresponding to σ_1, σ_2, and σ_3, respectively.

2.3 USBL-aided Navigation System of AUVs in Shallow Water

The objective of this study is to design a navigation system robust to outliers using the USBL position information for the operation of AUVs in shallow waters. Since the error characteristics of the USBL change according to the relative range and direction between the transceiver of the USBL and the AUVs, it is necessary to make an uncorrelated error model of the USBL to provide auxiliary measurement information in the navigation system. The navigation system of the vehicles equipped with inertial sensors can be modeled in various forms depending on the grade of the sensors. In this study, a dead-reckoning navigation method was applied to estimate the position. The simple equation of motion was established using only the speed, bearing angle, and position information of the AUV (Lee et al., 2017). If the AUV operates at a constant speed and the accelerations of the vehicle can be assumed decoupled normal noises in each direction, the equation of motion can be expressed as follows:

$$\boldsymbol{x}_{k+1} = \boldsymbol{F}_k \boldsymbol{x}_k + \boldsymbol{w}_k \tag{6}$$

$$\boldsymbol{w}_k \sim N(0, \boldsymbol{Q}_k) \tag{7}$$

where the state vector $\boldsymbol{x}_k (= \{X_k, Y_k, Z_k, \psi_k, u_k, v_k, w_k, r_k\}^T)$ is composed of 3-D position, heading angle, 3-D velocity, and yaw angular velocity of the vehicle. The system disturbance vector $\boldsymbol{w}_k$ is mean zero and the covariance matrix is $\boldsymbol{Q}_k$. If the 3-D position, heading, and 3-D velocity are observable, a measurement model can be expressed as

$$\boldsymbol{y}_k = \boldsymbol{H}_k \boldsymbol{x}_k + \boldsymbol{v}_k . \tag{8}$$

Here, $\boldsymbol{y}_k$ is the measured states, the measurement matrix $\boldsymbol{H}_k = [I_{7\times7}\, 0_{7\times1}]$. We assumed that the noise vector is the normal distribution $\boldsymbol{v}_k \sim N(0, \boldsymbol{R}_k)$ where the mean is zero and the covariance matrix $\boldsymbol{R}_k$ is

$$\boldsymbol{R}_k = \frac{1}{N-1} \mathrm{E}\left[(\boldsymbol{x}_k - \boldsymbol{\mu})^T (\boldsymbol{x}_k - \boldsymbol{\mu}) \right]. \tag{9}$$

If we assume that the horizontal position X_k and Y_k is not correlated with other state variables, we can separately handle the covariance matrix $\boldsymbol{R}_{xy_k}$ of the x and y position derived from the error of the USBL measurements. Then the covariance matrix can be expressed as follows in the horizontal plane:

$$\boldsymbol{R}_{xy_k} = \begin{bmatrix} \sigma_x^2 & \rho_{xy}\sigma_x\sigma_y \\ \rho_{xy}\sigma_x\sigma_y & \sigma_y^2 \end{bmatrix}, \tag{10}$$

where σ_x^2 and σ_y^2 represent the error variances of x and y, respectively, and $\rho_{xy}\sigma_x\sigma_y$ represents the error covariance correlated with the two variables. Because the USBL measurements of the x and y position in the shallow water are correlated with each other, it is necessary to decorrelate the error covariance by using its eigenvector before implementing a Kalman filter.

An arbitrary vector $\boldsymbol{x}$ can be converted into an arbitrary coordinate $\tilde{\boldsymbol{x}}$ using the unitary matrix Φ $(\Phi^H \Phi = I)$. If $\tilde{\boldsymbol{x}}$ is defined on the principal axis of the ellipse representing the error covariance of the USBL position measurement, it can be expressed as $\boldsymbol{x} = \boldsymbol{\phi}_1 \tilde{x}_1 + \boldsymbol{\phi}_2 \tilde{x}_2$ in the horizontal 2-D plane. Fig. 5 illustrates an example of matching the eigenvector to the main axis of the error covariance of the USBL measurements. In the figure, $\boldsymbol{\phi}_1$ and $\boldsymbol{\phi}_2$ are the eigenvectors of the error covariance matrix matched to the principal-axis of the error distribution.

Because the error covariance of the USBL measurement $\boldsymbol{R}_{xy_k}$ is a Hermitian matrix, the eigenvalues can be decomposed into a diagonal matrix of $\boldsymbol{R}_{xy_k} = \boldsymbol{\Phi}\, \Lambda\, \boldsymbol{\Phi}^H$ (Scharlau, 1985), where $\Lambda = diag(\sigma_1^2, \cdots, \sigma_N^2)$ and σ_i are eigenvalues. All eigenvalues of the covariance

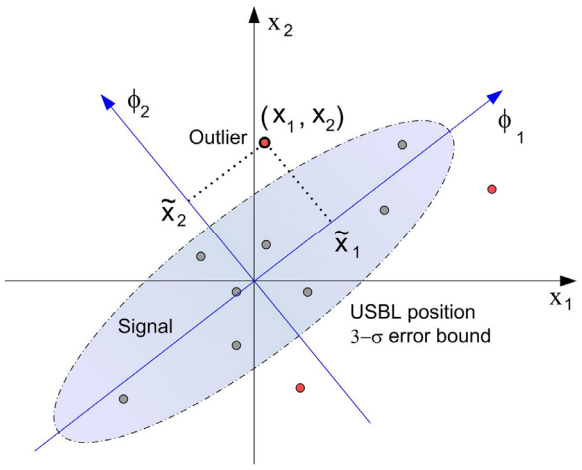

Fig. 5 Rotation of the axis using a unitary matrix

matrix are non-negative, i.e., $\sigma_i \geqq 0$, and $\boldsymbol{R}_{xy_k}\boldsymbol{\phi}_i = \sigma_i^2\boldsymbol{\phi}_i$. Since $\tilde{\boldsymbol{x}} = \Phi^H\boldsymbol{x}$, if the coordinate axis is set in the principal axis of the error distribution and then the error covariance is calculated, it can be decomposed into a diagonal matrix with the eigenvalues as follows:

$$\boldsymbol{R}_{\tilde{x}} = \tilde{\boldsymbol{x}}\tilde{\boldsymbol{x}}^T = \Phi^H\boldsymbol{x}\boldsymbol{x}^T\Phi = \Phi^H\boldsymbol{R}_{xy_k}\Phi = \Phi^H(\boldsymbol{\Phi}\,\Lambda\boldsymbol{\Phi}^H)\Phi = \Lambda \tag{11}$$

Therefore, the error covariance, which is correlated depending on the relative position and angle of the vehicle with respect to the USBL reference station, is decorrelated by transforming its axis to the principal component axis. And then the decorrelated error covariance can be used for implementing the USBL-aided navigation. If the error of the USBL measurement is located outside a certain bound, e.g., 3-σ illustrated in Fig. 5, we can decide that the USBL measurement is an outlier.

The integrated navigation system aided with the USBL was developed using the Kalman filter (Gelb, 1974; Simon, 2006). Fig. 6 shows a configuration diagram of the navigation system implemented in this study. The simulations of the navigation system were performed by updating the system error covariance with the innovation which is the difference of the estimated position and the USBL measurement with outlier. Assuming that the effect of time delay of the position data transmitted through an acoustic telemetry modem was compensated by the dead-reckoning navigation in a short interval, the time delay was not considered in the simulations.

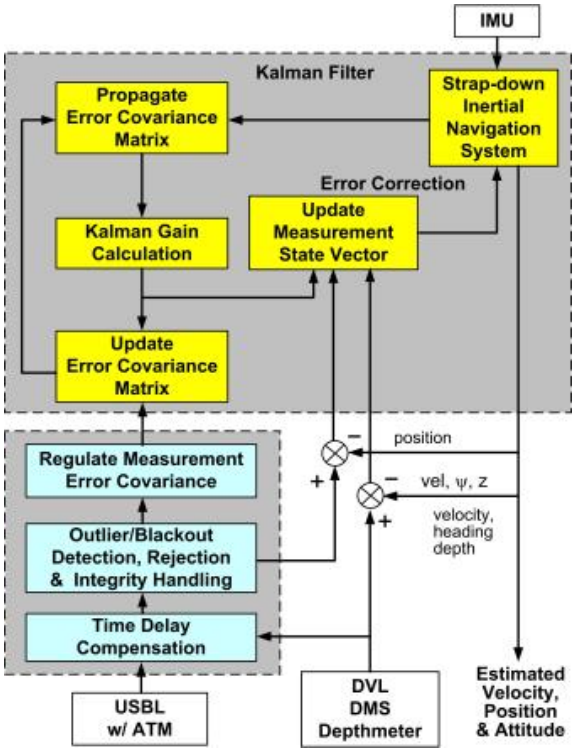

Fig. 6 USBL-aided integrated navigation system based on the inertial measurement unit and DVL with the uncorrelated USBL error model and outlier rejection

3. Underwater Navigation with the Uncorrelated Error Model of USBL

3.1 Motion Data of an AUV and Simulation of the USBL Measurements

A navigation simulation involving the USBL outlier rejection algorithm was performed using a dataset of the 1-hours surface

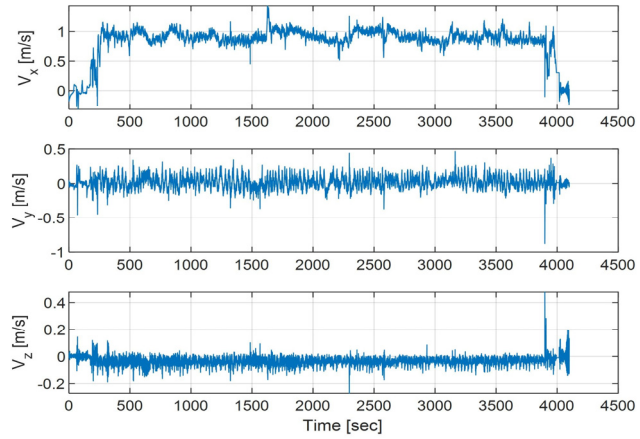

(a)

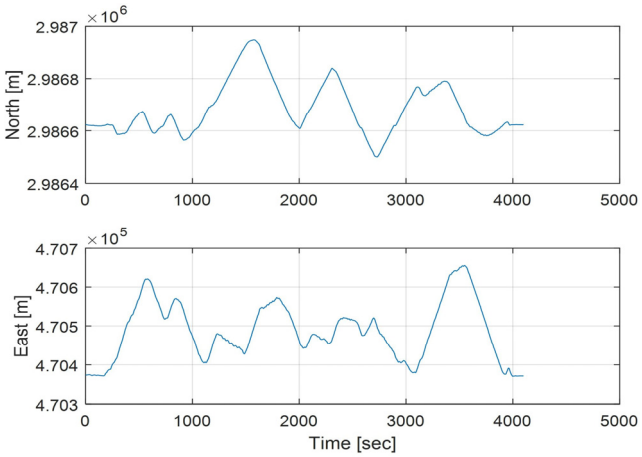

(b)

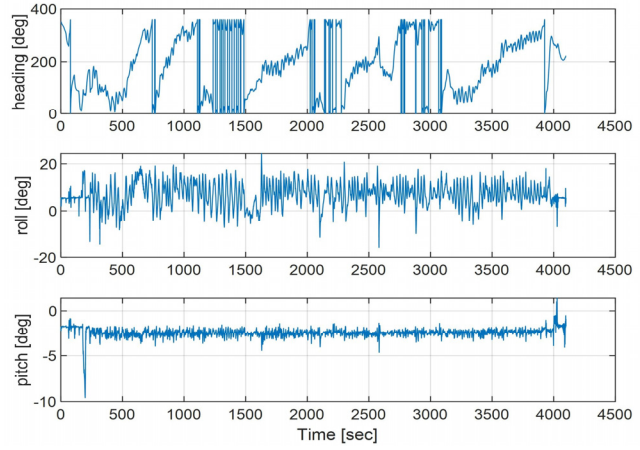

(c)

Fig. 7 Experimental data used in the simulation for the integrated navigation: (a) Velocity of the vehicle in the x, y, and z direction; (b) Y and X positions; (c) Attitude of the vehicle

Table 2 Specifications of the AHRS of the EvoLogics USBL

Roll / Pitch	0.2° / 0.4° (Static) 0.5° / 2.0° (Dynamic)
Yaw	1.0°

navigation of an AUV owned by Hanwha Systems Co., Ltd. The experiment was conducted at surface by reciprocating an arbitrary short-range path within Jangmok Bay at Jeoje Island. The sensors equipped on the AUV were a global positioning system (GPS), an inertial measurement unit (IMU FI200P), a Doppler velocity log (DVL RDI), an attitude heading reference system (AHRS) (TCM-XB), and a depth meter. To realize a situation in which a large navigation error occurred during blackout, a dead-reckoning navigation system integrated with the horizontal velocities and heading angle was introduced. The uncorrelated error model of USBL was applied to the navigation system. Fig. 7 presents the experimental data of the AUV used in the simulation. Fig. 7(a) shows the forward, lateral and vertical velocities measured by the DVL, u, v, w; Fig. 7(b) shows the AUV's latitude and longitude measured by the GPS, y and x, and Fig. 7(c) shows the heading, roll and pitch angles of the AUV by the AHRS. All the sensor information was stored at 100 sps (samples per second) rate, and the sampling rate of the DVL was 10 sps.

The experiment was performed on the sea surface to acquire the absolute position with the GPS, so the USBL measurement was not conducted. Instead, the USBL positioning data was simulated by adding the errors, generated with the stochastic features of the USBL sensor and a certain bound of outlier, to the absolute position. We used the specifications of the USBL EvoLogics 18/34 in the simulation and produced the USBL positioning data from a reference station to the current position of the vehicle at every 2 seconds. Additionally, we supposed the outlier ratio of the USBL would be set as 20%, so the outlier was generated at 10-seconds interval. The bearing-angle error of the USBL was set as 1.0° rms to consider the heading sensor specifications of the USBL built-in AHRS, as shown in Table 2. The range error of the USBL was set as 1.0 m rms to consider the motion compensation error of the moving vehicle and the variation of the acoustic propagation media. The outliers were generated by adding uniformly distributed random variables in [0, 30] m displacement and in [0, 360]° angle, which is independent of the current position of the vehicle.

Fig. 8 shows the USBL positioning data generated according to the AUV trajectory as Fig. 7(b) in case of no outlier, where the initial position of the vehicle was set at (0, 0) and the reference station of the USBL transceiver was located at (−100, 300). The error increased in the direction perpendicular to the radial direction as the distance from the reference station to the USBL increased. The error of the simulated USBL measurements increased in the orthogonal direction of the radial axis of the range from the reference station to the vehicle as the range increased. In addition to changing the magnitude, the principal axis of the error changed according to the location of the reference station. Fig. 9 shows the process of generating the simulated error of

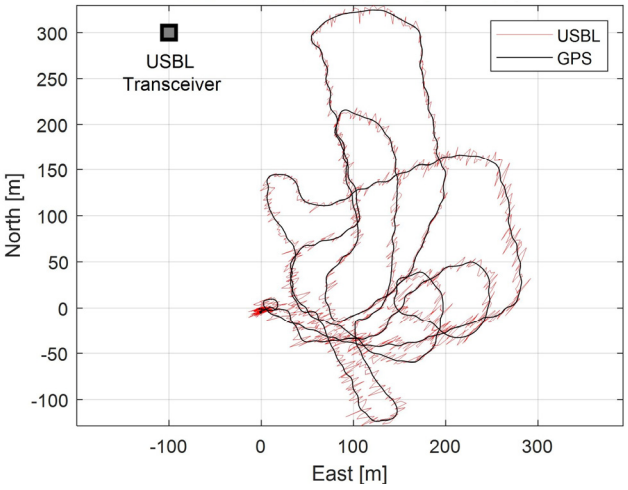

Fig. 8 USBL measurements generated by adding normal angular and range errors to the GPS positions

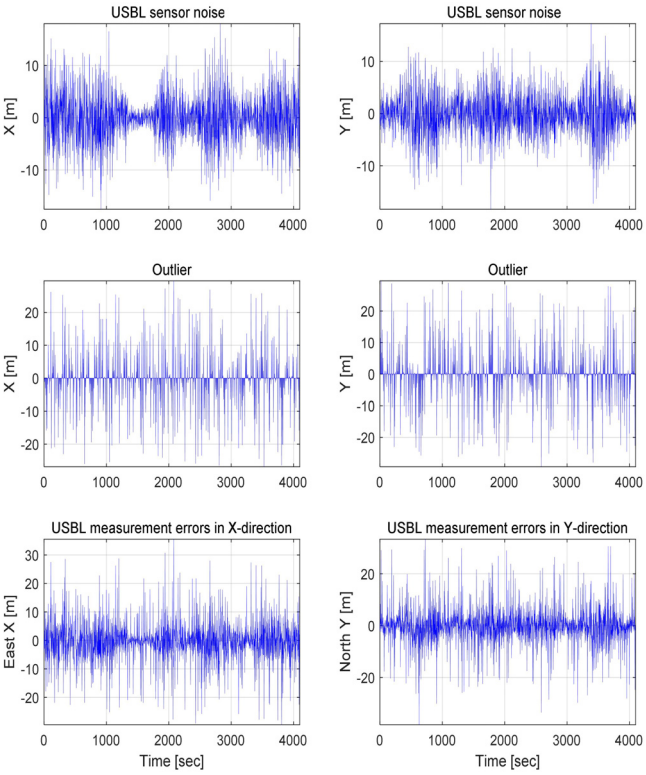

Fig. 9 Simulated USBL measurements with outliers: (top) intrinsic errors of the USBL—0.5 sps with Gaussian noise in the range direction and the orthogonal direction thereto; (middle) outliers—0.1 sps with uniform noise in the distance range of [0 30] m and the angular range [0, 360]°; (bottom) simulated errors. USBL measurements were generated by adding GPS measurements to these errors.

the USBL measurements: The upper parts are the simulated position error of the USBL measurements in the x- and y-directions; The middle parts are outliers generated as explained previously; The lower parts show the simulated error of the USBL measurements including the two components of the errors.

3.2 Simulation of USBL-aided Underwater Navigation with the Uncorrelated Error Model

A simulation was performed for the USBL-aided navigation system with the uncorrelated error model of USBL measurement. The range and angular rms error of the USBL used in the simulation was characterized by $\sigma_r = 1.0$ m and $\sigma_\psi = 1.0°$, respectively. The procedure of the simulation was as follows: (1) Define the rms error σ_r in the radial direction and the rms error σ_ψ in the orthogonal direction to the radial direction; (2) Calculate the first principal axis PC1 and the second principal axis PC2 through PCA at the estimated position of the vehicle; (3) Decorrelated the error covariance matrix by obtaining the σ_1 and σ_2 corresponding to the principal components of PC1 and PC2 with the rotation matrix at the time instant when the USBL measurement is received; (4) Apply the decorrelated covariance matrix to the Kalman filter of the navigation system.

Another simulation of the navigation system having no outlier of the USBL was also conducted for comparison with a conventional method. In the navigation simulation, the outlier judge level (OJL) was determined by a certain level, e.g. 5- σ , in the principal axes. When the difference between the USBL measurement and the estimated position of the navigation system exceeds the OJL, the navigation system decides the USBL measurement as outlier and discards the signal. In the proposed navigation system, the OJL was determined by the five times of the MD, 5-σ_{MD}, for the difference between the USBL measurement and the estimated position. Whenever the USBL measurement was newly acquired, the MD σ_{MD} was calculated with the rms errors of the radial direction and its orthogonal direction, σ_r and σ_ψ, respectively, at the estimated position of the vehicle. When the MD deviated from the OJL 5-σ_{MD}, the USBL measurement was discarded in the simulation.

Figs. 10 and 11 show the simulation results of the USBL-aided navigation system having the uncorrelated error model of USBL for the cases of no outlier and the outliers, respectively. The outliers occurred at 10-seconds interval as described previously. Figs. 10(a) and 11(a) depict the trajectories of the USBL measurement and the estimated position of the vehicle in the xy-plane. The USBL measurements were indicated by the blue dots and the estimated position was marked in the red solid lines. Figs. 10(c) and 11(c) are enlarged plots in the time of [3,050 3,300] s for Figs 10(a) and 11(a), respectively. The estimated positions of the two simulations exhibited a slight difference, which was attributed to the effect of the unrejected outliers within the OJL. Comparing the two simulation results, therefore, we can find the outliers larger than the OJL were almost completely rejected and the proposed navigation system stably produced the estimated position of the vehicle even when the USBL measurement contaminated by outliers. Figs. 10(b) and 11(b) show the estimation errors of the navigation system in the x- and y-positions. The rms error of the estimated position was 3.50 m when only the intrinsic error of the USBL sensor was considered, and 3.87 m when the outliers were included additionally. The estimation error of the navigation system with the outliers increased by approximately 10%

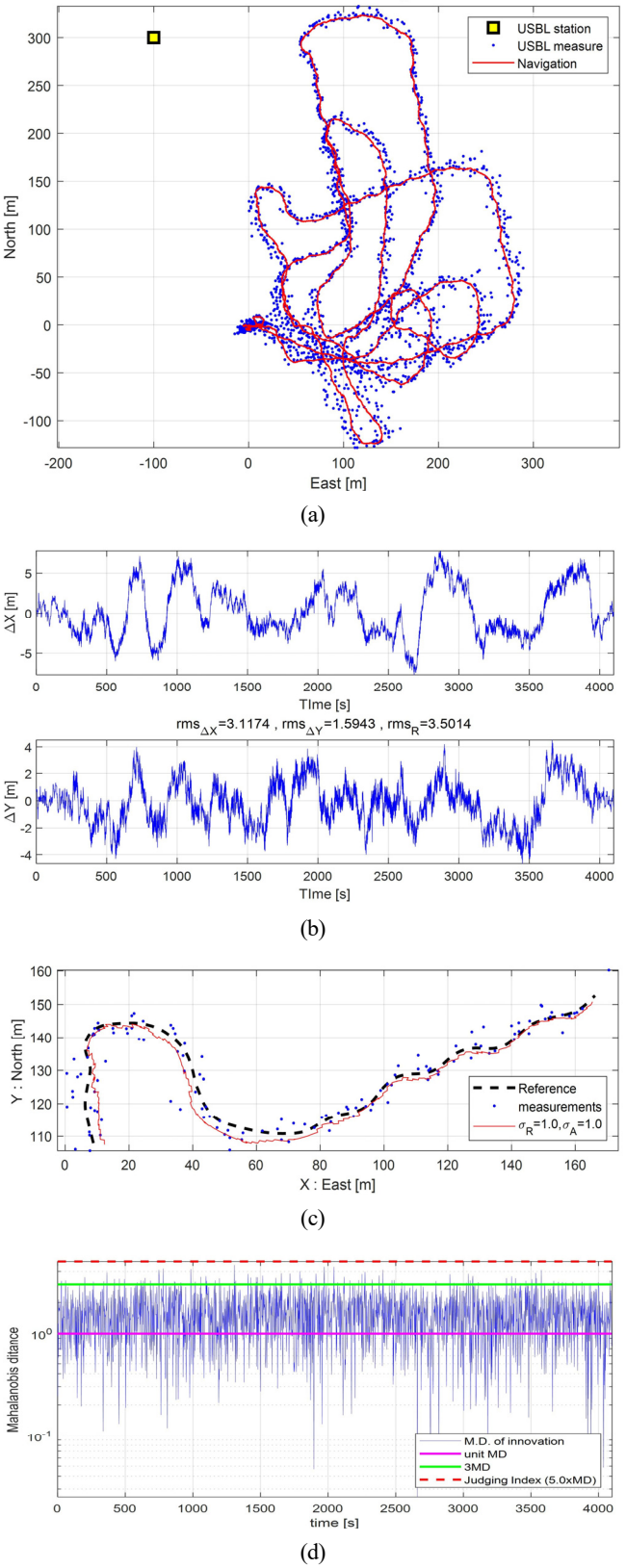

Fig. 10 Simulation results of the navigation system using the uncorrelated error covariance model without outlier: (a) Trajectories of USBL measurements and estimated positions; (b) Navigation errors in the x- and y-positions; (c) The xy-plane trajectories: zoomed in for [3050, 3300] s; (d) Mahalanobis distance between the USBL measurements and the estimated positions

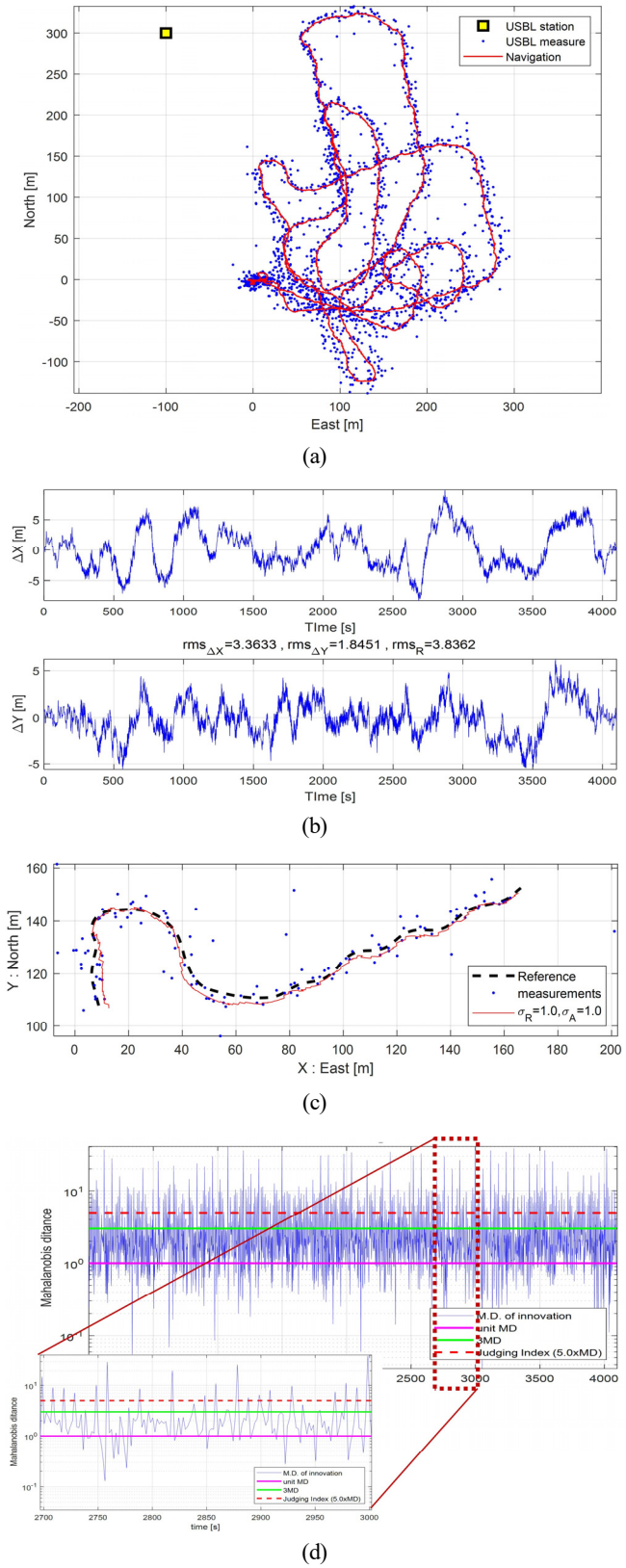

Fig. 11 Simulation results of the navigation system using the uncorrelated error covariance model with outliers: (a) Trajectories of USBL measurements and estimated positions; (b) Navigation errors in the *x*- and *y*-positions; (c) The *xy*-plane trajectories: zoomed in for [3050, 3300] s; (d) Mahalanobis distance between the USBL measurements and the estimated positions

compared to that of the navigation system with no outlier. This increment was caused by the outliers less than the OJL, which was updated in the navigation system. However, the two estimation errors show a very similar pattern.

Figs. 10(d) and 11(d) show the MD for the errors between the USBL measurements and the estimated position of the navigation system. The vertical axis of these figures is on a logarithmic scale. The MD was calculated in three steps. After acquiring the error at each USBL measurement, the principal axis was obtained from the range and the relative azimuth angle between the estimated position and the USBL reference station. And then the MD was calculated by decomposing the error. In Figs. 10(d) and 11(d), the outlier judge level 5-σ_{MD} is indicated by the red dotted line. In the case of no outlier, the MD in Fig. 10(d) did not exceed the OJL over the whole time. In the case with the outliers, the MD frequently exceeded the OJL due to the outliers, as shown in Fig. 11(d). Although the differences between the estimated position and the USBL measurements were mostly within 4-σ_{MD}, the OJL was set as 5-σ_{MD} considering margin of the estimation error of the navigation system in these simulations. The navigation system stably detected and rejected the outliers larger than the criterion, as shown in the enlarged subplot in Fig. 11(d).

3.3 Performance of Outlier Rejection

In order to examine the outlier removal characteristics of the USBL-aided navigation system, the estimated positions of the navigation system with the uncorrelated error model was compared to those of the navigation system with a conventional error model. Fig. 12 (a) and (b) show the results of the estimated position of the two navigation systems in the *xy*-plane for the time [2350 2600] s, respectively. In these figures, the black dashed lines indicate the GPS trajectories of the AUV, that is, the true positions, the blue points represent the measured positions with the USBL, and the colored solid lines indicates the trajectories of the estimated positions for the case of four different OJLs. In Fig. 12(a), the estimated positions of the proposed method for the four levels of OJL between 3.5-σ_{MD} and 5-σ_{MD} were exactly the same, so the four colored solid lines were all overlapped on one trajectory. That is, the USBL-aided integrated navigation system with the USBL decorrelation model identified and removed the outliers in the same way even when the OJL was changed between 3.5-σ_{MD} and 5-σ_{MD} in the time period.

In Fig 12(b), the estimated positions of the navigation system with conventional USBL error model were depicted with the colored solid lines, of which the OJL was 11, 16, 21, and 24m, respectively. It was shown that the estimated positions with the conventional error model were more affected by the outliers, which were not rejected when the OJL was specified larger. The smaller the OJL, the better the outliers were rejected. In such a conventional navigation system, it is required to make the OJL small in order to remove the outliers. However, if the OJL is not set larger than the intrinsic error bound of the USBL, the valid data of the USBL measurements will also be cut off.

The outlier reject characteristics were also reviewed, according to

the OJL selection in the navigation system with the conventional error model of USBL. Because the total simulation time was 4,094 s, the number of the USBL measurements used in the simulation was 2,047. Among these signals, the number of the outliers included N_{OL} was 410. The number of the outliers' magnitude exceeding the OJL would be less than 410. Because the magnitude of the random outliers used in the simulation was uniformly distributed within the range of $[0\ L_{\max}(=30)]m$, the expected number of outliers can be expressed as $N_{\text{expected}} = N_{OL} \times (1 - OJL/L_{\max})$ in case of when there was no navigation error. The simulations were performed by adjusting the OJL for the navigation system with the conventional error model of USBL. Fig. 13 shows the estimated position errors with the conventional error model according to the OJL, as well as the number cut off the normal USBL signals needed for the navigation system.

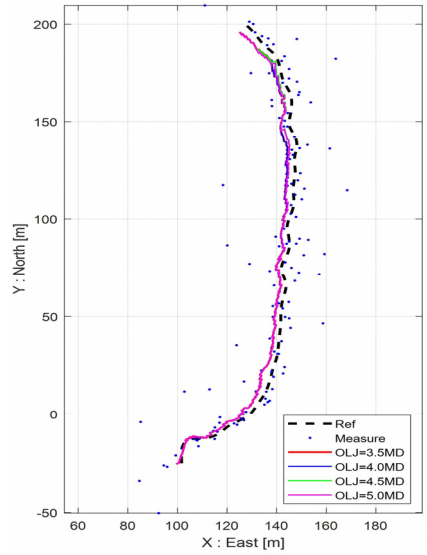

(a)

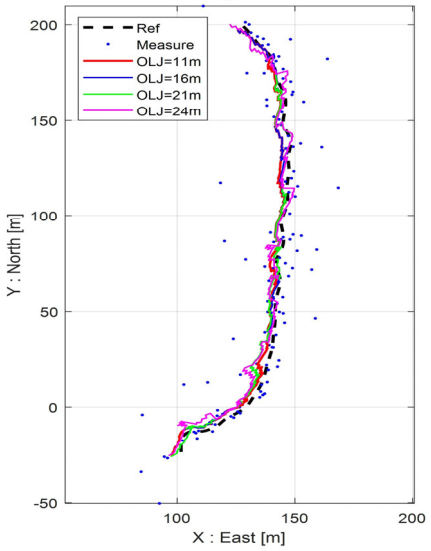

(b)

Fig. 12 Estimated positions of the navigation system for the uncorrelated USBL model and the conventional model: (a) Proposed navigation; (b) Conventional navigation

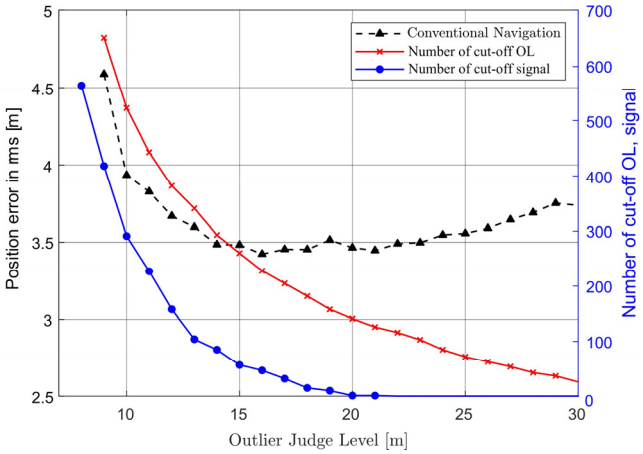

Fig. 13 Estimation errors with a conventional USBL error model and the numbers of cut-off the OL data (including signals) and the signals only according to the OJL

The estimated position error showed a tendency to decrease as the OJL increased in the range of $OJL \leq 13$ m, had minimum value in the range of 14 m $\leq OJL \leq$ 21 m, and gradually increased at $OJL >$ 21 m. The OJL should be set larger than 21 m to design the navigation system so that the normal USBL signals were not cut off. Otherwise, some of the normal signals larger than the OJL would be discarded. When the OJL was 22 m, 116 signals were judged as outliers and discarded without losing normal signal. In this case, the expected number of outliers will be $N_{\text{expected}} = 109$. Because the estimated position of the navigation system included errors, it is reasonable that the number of the blocked outliers differed from the expected value by approximately 6%. When the OJL was 16 m, the position estimation error was minimized, as shown in Fig. 13 and Table 3, while the number of the total blocked signal was 228. Among them, 47 normal USBL signals were blocked. The number of the blocked outliers in the simulation was 181, which differed approximately 5% from the expected number of 191. When the OJL was adjusted from 16 to 22 m, the blockage of the 47 normal signals was prevented. However, the 65 outliers were additionally considered as normal signals.

Therefore, in the navigation system using the conventional error model of USBL, the loss of the normal USBL signals is inevitable for ensuring outlier rejection. When a large OJL is specified to avoid losing the normal signals of USBL, outliers within the OJL are

Table 3 Numbers of cut-off outliers and normal signals with respect to the OJL for conventional navigation

Outlier Judge level OJL (m)	# of cut-off data	# of cut-off normal signals	# of cut-off outliers
12	382	158	224
13	341	104	237
16	228	47	181
17	205	32	173
22	116	0	116
29	37	0	37

identified as signals and adversely affects the navigation system. Conversely, when a small OJL is specified, some normal signals are lost, which also adversely affects the navigation system.

In contrast, the navigation system with the uncorrelated error model of USBL can designate the OJL according to the Mahalanobis distance, so it is possible to design a navigation system robust to outliers while preventing the loss of normal USBL signals. Fig. 14, similar as Fig. 13, shows the positioning errors of the proposed navigation system designed with $OJL = 3.5\text{-}\sigma_{MD}$ and $\sigma_R = 2.0$ m, the number of the signals detected as outliers and cut-off (including the USBL signals), and the number of the cut-off normal USBL signals. In the figure, the horizontal axis represents the change of the OJL, of which the angular rms error of the USBL σ_ψ is varying within the range $[0.5\ \ 1.5]°$. In the simulations, the rms error σ_ψ was also related with the covariance of the noise vector in the navigation system. From the point of view of outlier rejection, a value larger σ_ψ than 1.2 is required because the normal USBL signals were lost when it was designed with $\sigma_\psi \leq 1.2°$.

In Fig. 14 and Table 4, as σ_ψ was set smaller, the number of the cut-off USBL signals increased. When σ_ψ is set larger than 1.2, no signal was lost. In the range of $\sigma_\psi \geq 0.8°$, as the value of σ_ψ increases, the number of the rejected outliers decreased, but the change was very small. In $\sigma_\psi < 0.8°$, the number of the rejected outliers was independent of the level of σ_ψ. When $\sigma_\psi = 1.2°$, one normal signal was lost, and the 282 outliers were rejected. In this case, an equivalent OJL in the Euclidean space would be 9.3 m. From the simulations, the proposed method has shown better performance of outlier rejection than the conventional method. In these simulations, on the other hand, the measurement error model of the navigation system was related with the level of σ_ψ of the OJL $3.5\text{-}\sigma_{MD}$. When σ_ψ was larger than 0.8°, the estimated position errors increased as σ_ψ increases in the measurement error model of the system. So, it is required to designate a fixed value for σ_ψ in the error covariance of the navigation system.

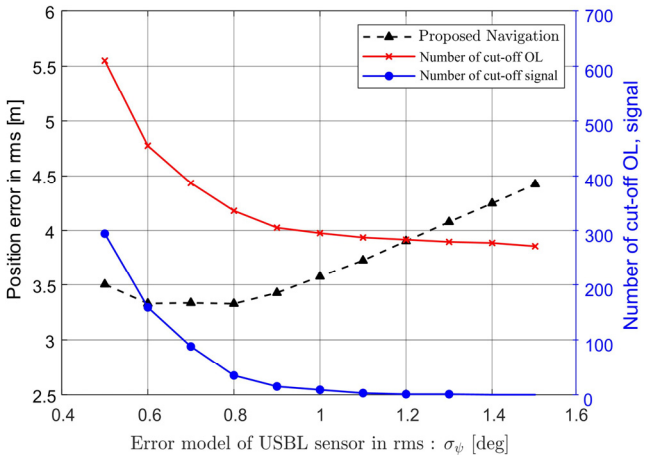

Fig. 14 Estimation errors with the proposed USBL error model and the numbers of cut-off the OL data (including signals) and the signals only according to $\sigma_\psi = [0.5\ 1.5]°$ (fixed $OJL = 3.5\text{-}\sigma_{MD}$ and $\sigma_R = 2.0$ m)

Table 4 Numbers of cut-off outliers and normal signals with respect to the OJL for the proposed navigation system

Outlier Judge level σ_ψ (deg)	# of cut-off data	# of cut-off normal signals	# of cut-off outliers
0.6	455	159	296
0.7	387	88	299
0.8	336	35	301
1.0	295	9	286
1.2	283	1	282
1.5	271	0	271

Therefore, the navigation system with the uncorrelated model of USBL is more robust to outliers than the navigation system with a conventional error model of it.

3.4 Blackout Response Characteristics

When the position measurement is not valid for a long time, the error of the navigation system increases in proportion to the blackout time. As the blackout time increases, the measured position of the USBL after the blackout might be significantly different from the estimated position of the navigation system. The outlier rejection method proposed in this paper can be applied when the navigation error is no larger than the order of the USBL position measurement error. Although it is beyond the scope of this article, the method of determining the integrity of the received USBL signal after a blackout requires the development of an algorithm that integrates the error characteristics of the navigation system and the intrinsic features of the USBL. In this study, after a blackout, the operation status of the navigation system was examined by applying a simple method of setting the outlier decision level to twice the existing OJL.

A simulation was performed on the position estimation of the navigation system with the error model of USBL. We supposed that when an AUV surveying under an ice-shelf received a new USBL measurement during a homing activity after performing its mission in a remote sea area where the USBL signal did not reach. It was assumed that a blackout occurred in [1000, 2400] s of the total simulation time of 4,094 s in the previous simulation. The rms errors of the radial and angular direction was $\sigma_r = 1.0$ m, $\sigma_\psi = 1.0°$, respectively, and the outlier decision criterion was designed as $4\text{-}\sigma_{MD}$ in normal operation. In the simulation, the new reception of the USBL after the blackout occurred was considered a valid signal when the position deviation of $\Delta x = \tilde{x} - \hat{x}$, i.e., the difference between the measured position and the estimated position, was within $8\text{-}\sigma_{MD}$.

Fig. 15 shows the simulation results of the navigation system with the uncorrelated error model of USBL for the event in which a USBL blackout occurred. In Fig. 15(a), which presents the horizontal-plane trajectory, the estimated position denoted by the red solid line, the USBL measurements with outliers are shown as blue dots, and the USBLs that have not been received in the time zone of blackout are depicted in light gray. During the USBL blackout, the navigation system operated only with speed, attitude, and depth information. So,

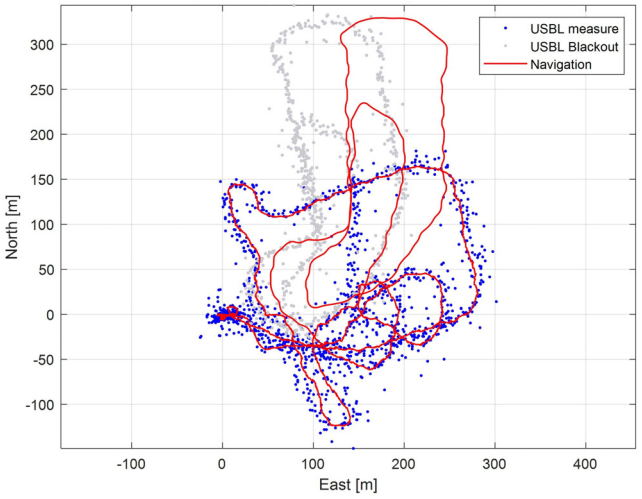

(a)

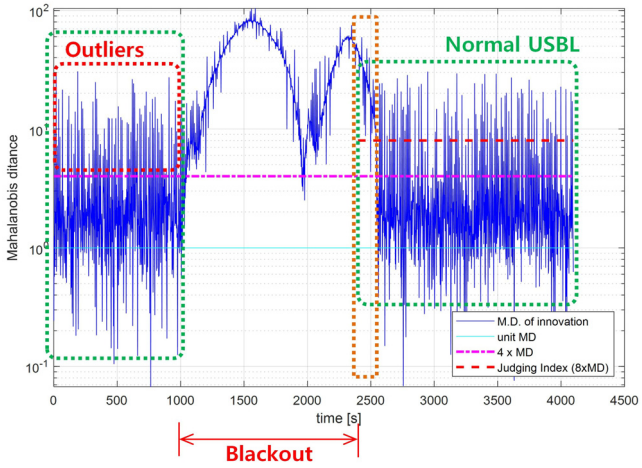

(b)

Fig. 15 Simulation results of the USBL-aided navigation system including outliers and blackout occurred in [1000 2400] s: USBL signals with blackout and estimated trajectories; (b) Mahalanobis distance

the AUV estimated the position that deviated from the true trajectory after 1,000 s of the blackout occurrence. The estimation error of position was up to about 81 m.

When the USBL positioning signal was received again after 2,400 s, it was judged as a valid signal when and if the difference between the measured USBL position and the estimated position of the navigation system was within 8-σ_{MD}. So, even if a normal USBL signal is received, the measurement cannot be used immediately as the innovation of the navigation system under a large deviation Δx.

As shown in Fig. 15(b), the MD between the measured position of USBL and the estimated position at 2,400 s was 47.1-σ_{MD}, exceeding the threshold level of 8-σ_{MD}. So, the AUV judged this signal as an outlier and did not use it as an innovation signal for the navigation system. Even when the normal USBL position measurement data were subsequently received, the navigation system continued to discard the USBL position measurement, because the deviation Δx exceeded the OJL. At 2,540 s, when the position error was within the range of 8-σ_{MD}, the navigation system used the USBL position measurement signal to update the error covariance, and the estimation error of the navigation system rapidly decreased and converged to the true position within 10 seconds. A further study on the integrity judgment reflecting the USBL positioning data received after a blackout and the navigation error is required.

4. Conclusions

This paper proposes a USBL-aided underwater navigation system with the uncorrelated error model of USBL, which can be applied to survey under Antarctic ice-shelf or missions in shallow water. The Mahalanobis distance (MD) and principal components (PC) of the USBL measurements in the horizontal plane were analyzed, of which the magnitude of the error and the direction of the principal axis of the error distribution varies according to relative position and distance between the reference station, typically USBL transceiver, and an AUV. Simulations of the navigation system were performed by synthesizing the measured data and the numerically generated data. A measured position dataset of the USBL were generated by adding the intrinsic noise of a USBL and the random outliers in magnitude and direction to the relative position between the GPS position and a reference station of the USBL. The proposed method can effectively reject the outliers without loss of the USBL signals by decorrelating the error covariance of the radial direction and its orthogonal direction of the USBL in the horizontal plane, and judging whether the USBL measurement is outlier based on the Mahalanobis distance. The simulation results indicated that the navigation system with the uncorrelated error model of USBL can reject outliers more robustly than the navigation system with a conventional error model of USBL. It was also illustrated that the estimation error of the navigation system may be reduced by applying the USBL measurement received after a blackout. The outliers of USBL would be apt to change in frequency and/or magnitude, depending on the sea conditions such as changes in water temperature and salinity. Therefore, it is necessary to adjust the outlier decision level accordingly to match the environmental conditions of the operating area of the AUV through field experiments at sea in the future. Further study is additionally required to analyze the integrity of the new measurement of the USBL after a long blackout and the convergence of the estimation error of the navigation system to the true position.

Conflict of Interest

No potential conflict of interest relevant to this article was reported.

Funding

This study was conducted with the support of the “Development of core technologies of underwater robot ICT for polar under-ice-shelf

exploration and remote monitoring (4/5)" and the Korea Coast Guard, as a key technology project of the Korea Research Institute of Ships and Ocean Engineering. These findings are a part of the ongoing research results of the "Development of AUV fleet and its operation system for maritime search (2/5)."

References

Chang, G. (2014). Robust Kalman filtering based on Mahalanobis distance as outlier judging criterion. *Journal of Geodesy*, *88*, 391−401. https://doi.org/10.1007/s00190-013-0690-8

De Maesschalck, R., Jouan-Rimbaud, D., & Massart, D. (2000). The Mahalanobis distance. *Chemometrics and Intelligent Laboratory Systems, 50*(1), 1−18. https://doi.org/10.1016/S0169-7439(99)00047-7

EvoLogics GmbH. (2017). *EvoLogics underwater acoustic positioning system −User guide* (ver. 1.0B).

Gelb, A. (Ed.). (1974). *Applied optimal estimation*. MIT Press.

Hassan, S., Byun, H., & Kim, J. (2021). Iterative smoothing and outlier detection for underwater navigation. *arXiv preprint arXiv:2109.14220*. https://doi.org/10.48550/arXiv.2109.14220

Lee, P. M., Park, J. Y,, Baek, H., Kim, S. M., Kim, H. S., & Lee, P. Y. (2022). A study on modeling of uncorrelated measurement errors of USBL for aiding underwater navigation of AUVs. *Proceedings of the 2022 Joint Academic Conference of the Korean Association of Ocean Science and Technology Societies*, *Jeju, Korea,* F2302.

Lee, P. M., Shim, H., Baek, H., Kim, B., Park, J., Jun, B., & Yoo, S. (2017). A navigation system of a deep-sea ROV fusing USBL, DVL and heading measurements. *Journal of Ocean Engineering and Technology, 31*(4), 315−323. https://doi.org/10.26748/KSOE.2017.08.31.4.315

Luo, Q., Yan, X., Ju, C. Chen, Y., & Luo, Z. (2021). An ultra-short baseline underwater positioning system with Kalman filtering. *Sensors, 21*(1), 143. https://doi.org/10.3390/s21010143

Milne, P. H. (1983). *Underwater acoustic positioning systems.* Gulf Publishing Company.

Park, J. Y. (2021). *극지 빙하 탐사와 원격 모니터링을 위한 수중로봇 ICT 원천기술 개발* [Development of core technologies of underwater robot ICT for polar under-ice-shelf exploration and remote monitoring] (Technical Report BSPES4010-12310-2). Korea Research Institute of Ships and Ocean Engineering.

Scharlau, W. (1985). *Quadratic and Hermitian forms. Berlin*, Springer-Verlag. https://doi.org/10.1007/978-3-642-69971-9

Simon, D. (2006). *Optimal state estimation − Kalman, H_∞, and nonlinear approaches.* John Wiley & Sons.

Vasilijevic, A., Borovic, B., & Vukic, Z. (2012). Underwater vehicle localization with complementary filter: Performance analysis in the shallow water environment. *Journal of Intelligent Robotic Systems, 68*, 373−386. https://doi.org/10.1007/s10846-012-9766-6

Zhu, B., Li, D., Li, Z., He H., & Li, X. (2021). Robust adaptive Kalman filter for strapdown inertial navigation system dynamic alignment. *IET Radar, Sonar & Navigation, 15*(12), 1583−1593. https://doi.org/10.1049/rsn2.12148

Author ORCIDs

Author name	ORCID
Lee, Pan-Mook	0000-0002-0500-6167
Park, Jin-Yeong	0000-0002-8255-6402
Baek, Hyuk	0000-0002-3371-4160
Kim, Sea-Moon	0000-0002-0488-9770
Jun, Bong-Huan	0000-0002-4629-4433
Kim, Ho-Sung	0000-0002-5706-3163
Lee, Phil-Yeob	0000-0001-9065-1154

Instructions for Authors

General information

To submit a manuscript to the Journal of Ocean Engineering and Technology (JOET), it is advised to first carefully read the aims and the scope section of this journal, as it provides information on the editorial policy and the category of papers it accepts. Unlike many regular journals, JOET usually has no lag in acceptance of a manuscript and its publication. Authors that find a match with the aims and the scope of JOET are encouraged to submit as we publish works from all over the world. JOET adheres completely to guidelines and best practices published by professional organizations, including Principles of Transparency and Best Practice in Scholarly Publishing (joint statement by COPE, DOAJ, WAME, and OASPA (http://doaj.org/bestpractice) if otherwise not described below. As such, JOET would like to keep the principles and policies of those professional organizations during editing and the publication process.

Research and publication ethics

Details on publication ethics are found in http://joet.org/authors/ethics.php. For the policies on research and publication ethics not stated in the Instructions, Guidelines on Good Publication (http://publicationethics.org/) can be applied.

Requirement for membership

One of the authors who submits a paper or papers should be member of the Korean Society of Ocean Engineers (KSOE), except a case that editorial board provides special admission of submission.

Publication type

Article types include scholarly monographs (original research articles), technical articles (technical reports and data), and review articles. The paper should have not been submitted to other academic journal. When part or whole of a manuscript was already published to conference papers, research reports, and dissertations, then the corresponding author should note it clearly in the manuscript.

Copyright

After published to JOET, the copyright of manuscripts should belong to KSOE. A transfer of copyright (publishing agreement) form can be found in submission website (http://www.joet.org).

Manuscript submission

Manuscript should be submitted through the on-line submission website (http://www.joet.org). The date that manuscript was received through on-line website is the official date of receipt. Other correspondences can be sent by an email to the Editor in Chief or secretariat. The manuscript must be accompanied by a signed statement that it has been neither published nor currently submitted for publication elsewhere. The manuscript should be written in English or Korean. Ensure that online submission are in a standard word processing format. Corresponding author must write the manuscript using the JOET template provided in Hangul or MS Word format. Ensure that graphics are high-resolution. Be sure all necessary files have been uploaded/ attached.

Authors' checklist

Please refer to “Authors' Checklist” for details.

Article structure

Manuscript must be edited in the following order: (1) Title, (2) Authors' names and affiliations, (3) Keywords, (4) Abstract, (5) Nomenclature (optional), (6) Introduction, (7) Main body (analyses, tests, results, and discussions), (8) Conclusions, (9) Conflict of interest, (10) Funding (optional), (11) Acknowledgements (optional), (12) References, (13) Appendices (optional), (14) Author’s ORCIDs.

Abstract

A concise and factual abstract is required. The abstract should state briefly the background, purpose and methods of the research, the principal results and conclusions. An abstract should be written in 150-200 words. References are not cited in abstract whenever possible. Also, non-standard or uncommon abbreviations should be avoided, but if essential they must be defined at their first mention in the abstract itself.

Keywords

Immediately after the abstract, provide a maximum of 5 or 6 keywords.

Unit

Use the international system units(SI). If other units are mentioned, please give their equivalent in SI.

Equations

All mathematical equations should be c1early printed/typed using well accepted explanation. Superscripts and subscripts should be typed clearly above or below the base line. Equation numbers should be given in Arabic numerals enclosed in parentheses on the right-hand margin.

Tables

Tables should be numbered consecutively with Arabic numerals. Each table should be fully titled. All tables should be referred to in the texts.

Figures

Figures should be numbered consecutively with Arabic numerals. Each figure should be fully titled. All figures should be referred to in the texts. All the illustrations should be of high quality meeting with the publishing requirement with legible symbols and legends.

Conflict of interest

It should be disclosed here according to the statement in the Research and publication ethics regardless of existence of conflict of interest. If the authors have nothing to disclose, please state: “No potential

conflict of interest relevant to this article was reported."

Funding

Funding to the research should be provided here. Providing a FundRef ID is recommended including the name of the funding agency, country and if available, the number of the grant provided by the funding agency. If the funding agency does not have a FundRef ID, please ask that agency to contact the FundRef registry (e-mail: fundref.registry@crossref.org). Additional detailed policy of FundRef description is available from http://www.crossref.org/fundref/. Example of a funding description is as follows:

The study is supported by the Inha University research fund (FundRef ID: 10.13039/501100002632), and the Korea Health Personnel Licensing Examination Institute research fund (FundRef ID: 10.13039/501100003647).

Acknowledgments

Any persons that contributed to the study or the manuscript, but not meeting the requirements of an authorship could be placed here. For mentioning any persons or any organizations in this section, there should be a written permission from them.

References in text

References in texts follow the APA style. Authors can also see how references appear in manuscript text through the 'Template'.

Reference list

Reference list follows the APA style. Authors can see how references should be given in reference section through the 'Template'.

Appendices

The appendix is an optional section that can contain details and data supplemental to the main text. If there is more than an appendix, they should be identified as A, B, C, etc. Formulae and equations in appendices should be given separate numbering: Eq. (A1), Eq. (A2), etc.; in a subsequent appendix, Eq. (B1) and so on. Similarly for tables and figures: Table A1; Fig. A1, etc.

ORCID (Open Researcher and Contributor ID)

All authors are recommended to provide an ORCID. To obtain an ORCID, authors should register in the ORCID web site: http://orcid.org. Registration is free to every researcher in the world. Example of ORCID description is as follows:

Joonmo Choung: https://orcid.org/0000-0003-1407-9031

Peer review and publication process

The peer review process can be broadly summarized into three groups: author process, review process, and publishing process for accepted submissions. General scheme is presented in Figure 1.

Check-in process for review

If the manuscript does not fit the aims and scope of the Journal or does not adhere to the Instructions to Authors, it may be rejected immediately after receipt and without a review. Before reviewing, all submitted manuscripts are inspected by Similarity Check powered by iThenticate (https://www.crossref.org/services/similarity-check/), a plagiarism-screening tool. If a too high degree of similarity score is found, the Editorial Board will do a more profound content screening.

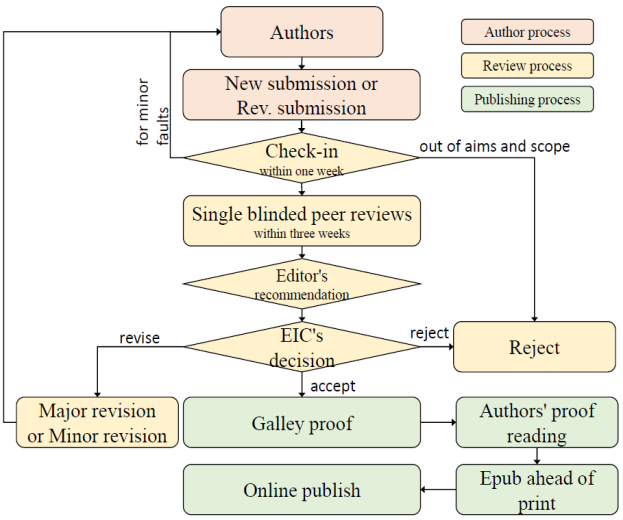

Figure 1 Flow chart of the peer review and publication process of JOET

The criterion for similarity rate for further screening is usually 15%; however, rather than the similarity rate, the Editorial Board focuses on cases where specific sentences or phrases are similar. The settings for Similarity Check screening are as follows: It excludes quotes, bibliography, small matches of 6 words, small sources of 1%, and the Methods section.

Number of reviewers

Reviewers will be selected from the list of reviewers. Manuscripts are then peer reviewed by at least 2 experts in the corresponding field, usually by 2.

Peer review process and the author response to the reviewer comments

JOET adopts single blind review, which means that the authors do not know the identity of the reviews. All papers, including those invited by the Editor, are subject to peer review.

The review period is 4 weeks. Usually the first decision is made within a week after completion of the review. The Editorial Board's decision after the review will be one of followings: Accept, Minor revision, Major revision, or Rejection. The Editorial Board may request the authors to revise the manuscript according to the reviewers' comments. If there are any requests for revision of the manuscript by the reviewers, the authors should do their best to revise the manuscript. If the reviewer's opinion is not acceptable or is believed to misinterpret the data, the author should reasonably indicate that. After revising the manuscript, the author should upload the revised files with a separate response sheet to each item of the reviewer's commentary. The author's revisions should be completed within 3 months after the request. If it is not received by the due date, the Editorial Board will notify the author. To extend the revision period beyond 3 months, the author should negotiate that with the Editorial Board. The manuscript review process can be provided for up two rounds. If the authors wish further review, the Editorial Board may consider it. The Editorial Board will make a final decision on the approval of the submitted manuscript for publication and can request any further corrections, revisions, and deletions of the article text if necessary. Statistical editing is also performed if the data requires professional statistical review by a statistician.

Processing after acceptance

If the manuscript is finally accepted, the galley proof will be sent to the corresponding author after professional manuscript editing and English proofreading. Proofreading should be performed for any misspellings or errors by the authors. Proofreading manuscript for publication is provided to the corresponding author, and the corresponding author must review the proofreading manuscript. Corresponding authors are responsible for the content of the proofreading manuscript and any errors. After final proofreading, the manuscript may appear at the journal homepage as an article in press with a unique DOI number for rapid communication. All published articles will be replaced by the replacement XML file and a final PDF.

Feedback after publication

If the authors or readers find any errors, or contents that should be revised, it can be requested from the Editorial Board. The Editorial Board may consider erratum, corrigendum or a retraction. If there are any revisions to the article, there will be a CrossMark description to announce the final draft. If there is a reader's opinion on the published article with the form of Letter to the editor, it will be forwarded to the authors. The authors can reply to the reader's letter. Letter to the editor and the author's reply may be also published.

How the journal handle complaints and appeals

The policy of JOET is primarily aimed at protecting the authors, reviewers, editors, and the publisher of the journal. If not described below, the process of handling complaints and appeals follows the guidelines of the Committee of Publication Ethics available from: https://publicationethics.org/appeals

- *Who complains or makes an appeal?*

Submitters, authors, reviewers, and readers may register complaints and appeals in a variety of cases as follows: falsification, fabrication, plagiarism, duplicate publication, authorship dispute, conflict of interest, ethical treatment of animals, informed consent, bias or unfair/inappropriate competitive acts, copyright, stolen data, defamation, and legal problem. If any individuals or institutions want to inform the cases, they can send a letter via the contact page on our website: https://www.joet.org/about/contact.php. For the complaints or appeals, concrete data with answers to all factual questions (who, when, where, what, how, why) should be provided.

- *Who is responsible to resolve and handle complaints and appeals?*

The Editorial Board or Editorial Office is responsible for them. A legal consultant or ethics editor may be able to help with the decision making.

- *What may be the consequence of remedy?*

It depends on the type or degree of misconduct. The consequence of resolution will follow the guidelines of the Committee of Publication Ethics (COPE).

Article processing charge

Payment due

Article processing charge (APC) covers the range of publishing services JOET provides. This includes provision of online tools for editors and authors, article production and hosting, and customer services. Upon editorial acceptance of an article for the regular review service and upon submission of an article for the fast review service, the corresponding author will be notified that payment is due.

APC

The APC up to 6 pages is ₩200,000 (or ＄200) and ₩550,000 (or ＄550) for the for the regular and fast review services, respectively. An extra APC of $50 per page is charged for papers longer than 6 pages, No taxes are included in this charge. For the fast review service, an advance fee of ₩250,000 ($250) should be paid on submission.

Payment methods

Credit card payment can be made online using a secure payment form as soon as the manuscript has been editorially accepted. We will we send a receipt by email once payment has been processed. Please note that payment by credit card carries a surcharge of 10% of the total APC.

Invoice payment is due within 7 days of the manuscript receiving editorial acceptance. Receipts are available on request.

JOET Template 2022.08.27

Journal of Ocean Engineering and Technology 00(0), 000-000, December, 2100
https://doi.org/10.26748/KSOE.2100.000
pISSN 1225-0767
eISSN 2287-6715

Original Research Article, Technical Article, Review Article, etc

Title of Article

Firstname Lastname[1], Firstname Lastname[2] and Firstname Lastname[3]

[1]*Professor, Department of OO, OO School, OO University, Busan, Korea*
[2]*Graduate Student, Department of OO, OO University, Seoul, Korea*
[3]*Senior Researcher, Department of OO, OO Engineering. Corp., Seoul, Korea*

KEY WORDS: Lumped mass line model, Explicit method, Steel lazy wave riser (Provide a maximum of 5 or 6 keywords.)

ABSTRACT:

Abstract Construction Guidelines
1) Describe the research background and aims in 1-2 sentences
2) Describe the research/analysis method (method section) in 2-3 sentences.
3) Describe the research/analysis results (results) in 2-3 sentences.
4) Describe the research conclusion in 1-2 sentences.
Abstract Editing Guidelines
1) Review English grammar.
2) Describe in 150-200 words.
3) When using an abbreviation or acronym, write the acronym after full words.
4) Abbreviations (acronyms) used only once should be written in full words only, and no acronyms.
5) References are not included in the abstract.

Nomenclature (Optional)

ITOC	Increment of total operating cost ($/yr)
LHV	Lower heating value (kJ/kg)
Pw	Power (kW)
T	Temperature (K)
V	Volume (m^3)
ρ	Density (kg/m^3)

1. Introduction

The introduction should briefly place the study in a broad context and highlight why it is important. It should define the purpose of the work and its significance. The current state of the research field should be reviewed carefully and key publications cited. Please highlight controversial and diverging hypotheses when necessary. Finally, briefly mention the main aim of the work and highlight the principal conclusions. As far as possible, please keep the introduction comprehensible to scientists outside your particular field of research.

Received 00 February 2100, revised 00 October 2100, accepted 00 October 2100
Corresponding author Firstname Lastname: +82-51-759-0656, e-mail@e-mail.com
It is a recommended paper from the proceedings of 2019 spring symposium of the Korea Marine Robot Technology (KMRTS).

2. General Information for Authors

2.1 Research and Publication Ethics

Authorship should be limited to those who have made a significant contribution to the conception, design, execution, or interpretation of the reported study. All those who have made significant contributions should be listed as co-authors. Where there are others who have participated in certain substantive aspects of the research project, they should be acknowledged or listed as contributors.

The corresponding author should ensure that all appropriate co-authors and no inappropriate co-authors are included on the paper, and that all co-authors have seen and approved the final version of the paper and have agreed to its submission for publication.

Details on publication ethics are found in the journal's website (http://joet.org/authors/ethics.php). For the policies on research and publication ethics not stated in the Instructions, Guidelines on Good Publication (http://publicationethics.org/) can be applied.

2.2 Requirement for Membership

One of the authors who submits a paper or papers should be member of The Korea Society of Ocean Engineers (KSOE), except a case that editorial board provides special admission of submission.

2.3 Publication Type

Article types include scholarly monographs (original research articles), technical articles (technical reports and data), and review articles. The paper should have not been submitted to another academic journal. When part or whole of a manuscript was already published to conference papers, research reports, and dissertations, then the corresponding author should note it clearly in the manuscript.

Example: It is noted that this paper is revised edition based on proceedings of KAOST 2100 in Jeju.

2.4 Copyright

After published to JOET, the copyright of manuscripts should belong to KSOE. A transfer of copyright (publishing agreement) form can be found in submission website (http://www.joet.org).

2.5 Manuscript Submission

Manuscript should be submitted through the on-line submission website (http://www.joet.org). The date that manuscript was received through on-line website is the official date of receipt. Other correspondences can be sent by an email to the Editor in Chief or secretariat. The manuscript must be accompanied by a signed statement that it has been neither published nor currently submitted for publication elsewhere. The manuscript should be written in English or Korean. Ensure that online submission is in a standard word processing format. Corresponding author must write the manuscript using the JOET template provided in Hangul or MS Word format. Ensure that graphics are high-resolution. Be sure all necessary files have been uploaded/ attached.

2.5.1 Authoer’s checklist

Authoer’s checklist and Transfer of copyright can be found in submission homepage (http:/www.joet.org).

3. Manuscript

Manuscript must be edited in the following order: (1) Title, (2) Authors' names and affiliations, (3) Keywords, (4) Abstract, (5) Nomenclature (optional), (6) Introduction, (7) Main body (analyses, tests, results, and discussions), (8) Conclusions, (9) Conflict of interest, (10) Funding (optional), (11) Acknowledgements (optional), (12) References, (13) Appendices (optional), (14) Author’s ORCIDs.

3.1 Unit

Use the international system units (SI). If other units are mentioned, please give their equivalent in SI.

3.2 Equations

All mathematical equations should be clearly printed/typed using well accepted explanation. Superscripts and subscripts should be typed clearly above or below the base line. Equation numbers should be given in Arabic numerals enclosed in parentheses on the right-hand margin. The parameters used in equation must be defined. They should be cited in the text as, for example, Eq. (1), or Eqs. (1)–(3).

$$G_{GEV}(x;\mu,\sigma,\xi)=\begin{cases}\exp[-(1+\xi(x-\mu)/\sigma)^{-1/\xi}] & \xi\neq 0\\ \exp[-\exp(-(x-\mu)/\sigma)] & \xi=0\end{cases} \quad (1)$$

in which μ, σ, and ξ represent the location ("Shift" in figures), scale, and shape parameters, respectively.

3.3 Tables

Tables should be numbered consecutively with Arabic numerals. Each table should be typed on a separate sheet of paper and be fully titled. All tables should be referred to in the texts.

Table 1 Tables should be placed in the main text near to the first time they are cited

Item	Buoyancy riser
Segment length[1)] (m)	370
Outer diameter (m)	1.137
Inner diameter (m)	0.406
Dry weight (kg/m)	697
Bending rigidity ($N\cdot m^2$)	1.66E8
Axial stiffness (N)	7.098E9
Inner flow density ($kg\cdot m^3$)	881
Seabed stiffness ($N/m/m^2$)	6,000

[1)]Tables may have a footer.

3.4 Figures

Figures should be numbered consecutively with Arabic numerals. Each figure should be fully titled. All the illustrations should be of high quality meeting with the publishing requirement with legible symbols and legends. All figures should be referred to in the texts. They should be referred to in the text as, for example, Fig. 1, or Figs. 1−3.

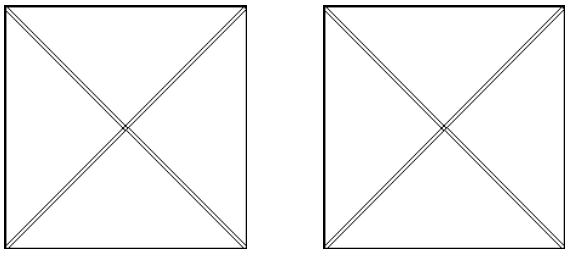

(a) (b)

Fig. 1 Schemes follow the same formatting. If there are multiple panels, they should be listed as: (a) Description of what is contained in the first panel; (b) Description of what is contained in the second panel. Figures should be placed in the main text near to the first time they are cited

3.5 How to Describe the References in Main Texts

- JOET recommends to edit authors' references using MS-Word reference or ZOTERO plug-in
- How to add a new citation and source to a document using MS-Word is found in MS Office web page: https://support.microsoft.com/en-us/office/add-citations-in-a-word-document-ab9322bb-a8d3-47f4-80c8-63c06779f127
- How to add a new citation and source to a document using ZOTERO is found in zotero web page: https://www.zotero.org/

4. Results

This section may be divided by subheadings. It should provide a concise and precise description of the experimental results, their interpretation as well as the experimental conclusions that can be drawn. Tables and figures are recommended to present the results more rapidly and easily. Do not duplicate the content of a table or a figure with in the Results section. Briefly describe the core results related to the conclusion in the text when data are provided in tables or in figures. Supplementary results can be placed in the Appendix.

5. Discussion

Authors should discuss the results and how they can be interpreted in perspective of previous studies and of the working hypotheses. The findings and their implications should be discussed in the broadest context possible. Future research directions may also be highlighted

6. Conclusions

This section can be added to the manuscript.

Conflict of Interest

It should be disclosed here according to the statement in the Research and publication ethics regardless of existence of conflict of interest. If the authors have nothing to disclose, please state: “No potential conflict of interest relevant to this article was reported.”, “The authors declare no potential conflict of interest.”, “The authors declare that they have no conflict of interests.”

Funding (Optional)

Please add: “This research was funded by Name of Funder, grant number XXX” and “The OOO was funded by XXX”. Check carefully that the details given are accurate and use the standard spelling of funding agency names at https://search.crossref.org/funding

Acknowledgments (Optional)

In this section you can acknowledge any support given which is not covered by the author contribution or funding sections. This may include administrative and technical support, or donations in kind (e.g., materials used for experiments). For mentioning any persons or any organizations in this section, there should be a written permission from them.

References

JOET follows the American Psychological Association (APA) style.

- Some samples are found in following web pages: https://apastyle.apa.org/style-grammar-guidelines/references/examples or https://www.ntnu.edu/viko/apa-examples
- JOET recommends editing authors’ references using MS-Word reference or ZOTERO plug-in
- How to add a new citation and source to a document using MS-Word is found in MS Office web page: https://support.microsoft.com/en-us/office/add-citations-in-a-word-document-ab9322bb-a8d3-47f4-80c8-63c06779f127
- How to add a new citation and source to a document using ZOTERO is found in ZOTERO web page: https://www.zotero.org/

Appendix (Optional)

The appendix is an optional section that can contain details and data supplemental to the main text. For example, explanations of experimental details that would disrupt the flow of the main text, but nonetheless remain crucial to understanding and reproducing the research shown; figures of replicates for experiments of which representative data is shown in the main text can be added here if brief, or as Supplementary data. Mathematical proofs of results not central to the paper can be added as an appendix.

All appendix sections must be cited in the main text. In the appendixes, Figures, Tables, etc. should be labeled starting with ‘A’, e.g., Fig. A1, Fig. A2, etc.

Examples:

https://doi.org/10.26748/KSOE.2019.022

https://doi.org/10.26748/KSOE.2018.4.32.2.095

Author ORCIDs

All authors are recommended to provide an ORCID. To obtain an ORCID, authors should register in the ORCID web site: http://orcid.org. Registration is free to every researcher in the world. Example of ORCID description is as follows:

Author name	**ORCID**
So, Hee	0000-0000-000-00X
Park, Hye-Il	0000-0000-000-00X
Yoo, All	0000-0000-000-00X
Jung, Jewerly	0000-0000-000-00X

Authors' Checklist

The following list will be useful during the final checking of a manuscript prior to sending it to the journal for review. Please submit this checklist to the KSOE when you submit your article.

< Checklist for manuscript preparation >

☐ I checked my manuscript has been 'spell-checked' and 'grammar-checked'.

☐ One author has been designated as the corresponding author with contact details such as
- E-mail address
- Phone numbers

☐ I checked abstract 1) stated briefly the purpose of the research, the principal results and major conclusions, 2) was written in 150−200 words, and 3) did not contain references (but if essential, then cite the author(s) and year(s)).

☐ I provided 5 or 6 keywords.

☐ I checked color figures were clearly marked as being intended for color reproduction on the Web and in print, or to be reproduced in color on the Web and in black-and-white in print.

☐ I checked all table and figure numbered consecutively in accordance with their appearance in the text.

☐ I checked abbreviations were defined at their first mention there and used with consistency throughout the article.

☐ I checked all references mentioned in the Reference list were cited in the text, and vice versa according to the APA style.

☐ I checked I used the international system units (SI) or SI-equivalent engineering units.

< Authorship checklist >

JOET considers individuals who meet all of the following criteria to be authors:

☐ Made a significant intellectual contribution to the theoretical development, system or experimental design, prototype development, and/or the analysis and interpretation of data associated with the work contained in the article.

☐ Contributed to drafting the article or reviewing and/or revising it for intellectual content.

☐ Approved the final version of the article as accepted for publication, including references.

< Checklist for publication ethics >

☐ I checked the work described has not been published previously (except in the form of an abstract or as a part of a published lecture or academic thesis).

☐ I checked when the work described has been published previously in other proceedings without copyright, it has clearly noted in the text.

☐ I checked permission has been obtained for use of copyrighted material from other sources including the Web.

☐ I have processed Plasgiarism Prevention Check through reliable web sites such as www.kci.go.kr, http://www.ithenticate.com/, or https://www.copykiller.org/ for my submission.

☐ I agree that final decision for my final manuscript can be changed according to results of Plasgiarism Prevention Check by JOET administrator.

☐ I checked one author at least is member of the Korean Society of Ocean Engineers.

☐ I agreed all policies related to 'Research and Publication Ethics'

☐ I agreed to transfer copyright to the publisher as part of a journal publishing agreement and this article will not be published elsewhere including electronically in the same form, in English or in any other language, without the written consent of the copyright-holder.

☐ I made a payment for reviewing of the manuscript, and I will make a payment for publication on acceptance of the article.

☐ I have read and agree to the terms of Authors' Checklist.

Title of article	:	
Date of submission	: DD/MM/YYYY	
Corresponding author	:	signature
Email address	:	

※ E-mail this with your signature to ksoehj@ksoe.or.kr

Publishing Agreement

ARTICLE DETAILS

Title of article :

Corresponding author :

E-mail address :

DOI : https://doi.org/10.26748/KSOE.2XXX.XXX

YOUR STATUS

I am one author signing on behalf of all co-authors of the manuscript.

ASSIGNMENT OF COPYRIGHT

I hereby assign to the Korean Society of Ocean Engineers, the copyright in the manuscript identified above and any tables, illustrations or other material submitted for publication as part of the manuscript (the "Article"). This assignment of rights means that I have granted to Korean Society of Ocean Engineers the exclusive right to publish and reproduce the Article, or any part of the Article, in print, electronic and all other media (whether now known or later developed), in any form, in all languages, throughout the world, for the full term of copyright, and the right to license others to do the same, effective when the Article is accepted for publication. This includes the right to enforce the rights granted hereunder against third parties.

SCHOLARLY COMMUNICATION RIGHTS

I understand that no rights in patents, trademarks or other intellectual property rights are transferred to the Journal owner. As the author of the Article, I understand that I shall have: (i) the same rights to reuse the Article as those allowed to third party users of the Article under the CC-BY-NC License, as well as (ii) the right to use the Article in a subsequent compilation of my works or to extend the Article to book length form, to include the Article in a thesis or dissertation, or otherwise to use or re-use portions or excerpts in other works, for both commercial and non-commercial purposes. Except for such uses, I understand that the assignment of copyright to the Journal owner gives the Journal owner the exclusive right to make or sub-license commercial use.

USER RIGHTS

The publisher will apply the Creative Commons Attribution-Noncommercial Works 4.0 International License (CC-BY-NC) to the Article where it publishes the Article in the journal on its online platforms on an Open Access basis.

The CC-BY-NC license allows users to copy and distribute the Article, provided this is not done for commercial purposes and further does not permit distribution of the Article if it is changed or edited in any way, and provided the user gives appropriate credit (with a link to the formal publication through the relevant DOI), provides a link to the license, and that the licensor is not represented as endorsing the use made of the work. The full details of the license are available at http://creativecommons.org/licenses/by-nc/4.0/legalcode.

REVERSION OF RIGHTS

Articles may sometimes be accepted for publication but later rejected in the publication process, even in some cases after public posting in "Articles in Press" form, in which case all rights will revert to the author.

☑ I have read and agree to the terms of the Journal Publishing Agreement.

Corresponding author:

name signature

※ E-mail this with your signature to ksoehj@ksoe.or.kr (Papers will not be published unless this form is signed and returned)

Research and Publication Ethics

Journal of Ocean Engineering and Technology (JOET) adheres to the guidelines published by professional organizations, including Committee on Publication Ethics (COPE; https://publicationethics.org/)

1. Authorship

JOET considers individuals who meet all of the following criteria to be authors:

1) Made a significant intellectual contribution to the theoretical development, system or experimental design, prototype development, and/or the analysis and interpretation of data associated with the work contained in the article.
2) Contributed to drafting the article or reviewing and/or revising it for intellectual content.
3) Approved the final version of the article as accepted for publication, including references.

Contributors who do not meet all of the above criteria may be included in the Acknowledgment section of the article. Omitting an author who contributed to your article or including a person who did not fulfill all of the above requirements is considered a breach of publishing ethics.

Correction of authorship after publication: JOET does not correct authorship after publication unless a mistake has been made by the editorial staff.

2. Originality and Duplicate Publication

All submitted manuscripts should be original and should not be in consideration by other scientific journals for publication. Any part of the accepted manuscript should not be duplicated in any other scientific journal without permission of the Editorial Board, although the figures and tables can be used freely if the original source is verified according to the Creative Commons Attribution License (CC BY-NC). It is mandatory for all authors to resolve any copyright issues when citing a figure or table from other journal that is not open access.

3. Conflict-of-Interest Statement

Conflict of interest exists when an author or the author's institution, reviewer, or editor has financial or personal relationships that inappropriately influence or bias his or her actions. Such relationships are also known as dual commitments, competing interests, or competing loyalties. These relationships vary from being negligible to having a great potential for influencing judgment. Not all relationships represent true conflict of interest. On the other hand, the potential for conflict of interest can exist regardless of whether an individual believes that the relationship affects his or her scientific judgment. Financial relationships such as employment, consultancies, stock ownership, honoraria, and paid expert testimony are the most easily identifiable conflicts of interest and the most likely to undermine the credibility of the journal, the authors, or of the science itself. Conflicts can occur for other reasons as well, such as personal relationships, academic competition, and intellectual passion. If there are any conflicts of interest, authors should disclose them in the manuscript. The conflicts of interest may occur during the research process as well; however, it is important to provide disclosure. If there is a disclosure, editors, reviewers, and reader can approach the manuscript after understanding the situation and the background of the completed research.

4. Management Procedures for the Research and Publication Misconduct

When JOET faces suspected cases of research and publication misconduct such as a redundant (duplicate) publication, plagiarism, fabricated data, changes in authorship, undisclosed conflicts of interest, an ethical problem discovered with the submitted manuscript, a reviewer who has appropriated an author's idea or data, complaints against editors, and other issues, the resolving process will follow the flowchart provided by the Committee on Publication Ethics (http://publicationethics.org/resources/flowcharts). The Editorial Board of JOET will discuss the suspected cases and reach a decision. JOET will not hesitate to publish errata, corrigenda, clarifications, retractions, and apologies when needed.

5. Editorial Responsibilities

The Editorial Board will continuously work to monitor and safeguard publication ethics: guidelines for retracting articles; maintenance of the integrity of the academic record; preclusion of business needs from compromising intellectual and ethical standards; publishing corrections, clarifications, retractions, and apologies when needed; and excluding plagiarism and fraudulent data. The editors maintain the following responsibilities: responsibility and authority to reject and accept articles; avoiding any conflict of interest with respect to articles they reject or accept; promoting publication of corrections or retractions when errors are found; and preservation of the anonymity of reviewers.

6. Hazards and human or animal subjects

If the work involves chemicals, procedures or equipment that have any unusual hazards inherent in their use, the author must clearly identify these in the manuscript. If the work involves the use of animal or human subjects, the author should ensure that the manuscript contains a statement that all procedures were performed in compliance with relevant laws and institutional guidelines and that the appropriate institutional committee(s) has approved them. Authors should include a statement in the manuscript that informed consent was obtained for experimentation with human subjects. The privacy rights of human subjects must always be observed.

Ensure correct use of the terms sex (when reporting biological factors) and gender (identity, psychosocial or cultural factors), and, unless inappropriate, report the sex and/or gender of study participants, the sex of animals or cells, and describe the methods used to determine sex and gender. If the study was done involving an exclusive population, for example in only one sex, authors should justify why, except in obvious cases. Authors should define how they determined race or ethnicity and justify their relevance.

7. Secondary publication

It is possible to republish manuscripts if the manuscripts satisfy the conditions of secondary publication. These are:

- The authors have received approval from the Editorial Board of both journals (the editor concerned with the secondary publication must have access to the primary version).
- The priority for the primary publication is respected by a publication interval negotiated by editors of both journals and the authors.
- The paper for secondary publication is intended for a different group of readers
- The secondary version faithfully reflects the data and interpretations of the primary version.
- The secondary version informs readers, peers, and documenting agencies that the paper has been published in whole or in part elsewhere, for example, with a note that might read, "This article is based on a study first reported in the [journal title, with full reference]"
- The title of the secondary publication should indicate that it is a secondary publication (complete or abridged republication or translation) of a primary publication.

8. Complaints and Appeals

The process of handling complaints and appeals follows the guidelines of the COPE available from: https://publicationethics. org/appeals

9. Post-publication discussions and corrections

The post-publication discussion is available through letter to editor. If any readers have a concern on any articles published, they can submit letter to editor on the articles. If there found any errors or mistakes in the article, it can be corrected through errata, corrigenda, or retraction.

The Korean Society of Ocean Engineers